Understanding Magmatic Timescales and Magma Dynamics in Proterozoic Anorthosites: a Geochronological and Remote Sensing Investigation of the Kunene Complex (Angola)

Alan Martin Brower (567615) – 2017

Supervisor: Dr. Grant Bybee

Co-Supervisor: Dr. Jeremie Lehmann

UNIVERSITY OF THE WITWATERSRAND, JOHANNESBURG

A Dissertation submitted to the Faculty of Science, University of the Witwatersrand, in fulfillment of the requirements for the degree of Master of Science.

I declare that this dissertation is my own, unaided work. It is being submitted for the Degree of Master of Science at the University of the Witwatersrand, Johannesburg. It has not been submitted before for any degree or examination at any other University.

Alan Martin Brower

2nd day of the month of June 2017 in Johannesburg (Final Submission)

Abstract

The Kunene Anorthosite Complex (KAC), located in southwest Angola, is one of the largest Proterozoic anorthosite intrusions on Earth, with an areal extent of at least 18 000 km^2. The KAC is composed of anorthosite, leucotroctolite, leuconorite, leucogabbro and granitoids. Many aspects of Proterozoic anorthosite petrogenesis are still unknown with debates including the parental magma source, temporal restriction of anorthosite, and anorthositic magma emplacement mechanisms. Very little research has been conducted on the Angolan portion of the KAC, and published maps lack detail and are often inconsistent. Previous studies considered the Kunene Complex to be have formed as a layered intrusion and, more recently, as a series of coalesced plutons. As one of the largest and least studied Proterozoic anorthosites in the world, the KAC provides a unique opportunity to test recent ideas surrounding Proterozoic anorthosite petrogenesis related to the KAC. Its linear geometry, make-up of multiple plutons and large age range also create a great desire for study. This study allows for the development of new models for the emplacement dynamics, timescales, and tectonic setting of the KAC. This study makes use of the interpretation of remote sensing datasets (Landsat 8 and SRTM 3 – Shuttle Radar Topography Mission) as well as U-Pb TIMS (Thermal Ionisation Mass Spectrometer) geochronology to analyse the composition, structure and age variations of the KAC. In order to extract maximum compositional data from this magmatic complex, various image processing techniques have been performed, including false colour composites, a minimum noise fraction, a principle component analysis, and band ratioing for the Landsat 8 data. To best identify structural data, hill-shading and an automatic lineament extraction was used for the SRTM and Principle Component 1 images. The results of the Landsat Image processing enable identification of different spectral signals and allow for the differentiation of the KAC from country rocks, in addition to separating the anorthositic rocks of the KAC itself. From the SRTM imaging, lineament data were extracted and various structural features identified throughout the KAC. In combination with ground truthing, these lineaments are classified into either magmatic foliations, subsolidus planar structures or fault structures. Using these techniques, this study reiterates the batholitic appearance of the KAC and identifies two main magmatic entities of distinct crystallization age, composition and Landsat spectral response, making up the

KAC. In combination with ground truthing, a new interpretative lithological map for the KAC and adjacent country rocks has been produced.

Understanding the relative timing of the anorthosite emplacement is crucial for understanding how these enigmatic magmas form and how they rise through the crust. The ages and relative emplacement sequence of the individual batches forming the KAC are unknown. New high precision U-Pb ID-TIMS ages on zircon and baddeleyite for many of the newly defined spectral domains across the anorthositic complex are presented. These new geochronological results reveal subtle variations in crystallisation age within the KAC on the order of 10 Ma. There is no gradual age progression between potential distinct magmatic batches but distinct groupings of ages. Mean age clusters of 1379.8 ± 2.0 Ma (n=5) occurring to the north of the NE – SW striking Red Granite intrusions, whereas in the south there is an older age grouping of 1390.4 ± 2.3 (n=3). Two additional ages of 1400.5 ± 1.3 Ma and 1438.4 ± 1.1 Ma have been obtained in the centre and southeast of the complex, respectively. These results indicate that the Kunene anorthosites were emplaced over 60 Ma. The 40 Ma difference between emplacement of the first anorthositic body and the remaining anorthositic emplacement suggests two possibilities for the long-lived magmatic system: 1) Magma differentiation occurred slowly over an extended period of time with anorthositic mushes reaching their final emplacement depth at a faster rate. 2) Differentiation occurred at a faster rate but the mushes ascended slowly to their final emplacement depths. A link has been found between spectral domain composition and age. In general, leuconoritic domains are older than the leucotroctolitic domains. This may imply that the first pulses of magma received a greater degree of crustal contamination, forcing the initial broadly basaltic magma to produce orthopyroxene as the main mafic phase. The later pulses received less contamination as they ascended through the already partially melted and refractory crust, producing olivine as the mafic phase and deforming the older domains. This study reiterates the multiphase petrogenesis of Proterozoic anorthosites and sheds light on the assembly of crystal-rich magmas as they ascend through the crust. Utilizing the remote sensing data and the geochronological results, a new model for the petrogenesis of the KAC been developed and it is suggested that the most valid setting for the KAC is a continental arc.

Acknowledgements

This dissertation could not have been completed without the help, advice and support I received from so many. Firstly this project would not have been possible without the funding from the NRF Thuthuka grant which provided funds to cover two field expeditions and a trip to the University of Oslo (UiO), Norway, to perform the geochronological analyses. In addition to this funding, I would like to thank the REI Fund of the Geological Society of South Africa for funds to help cover the cost of my field work and lastly to the University of the Witwatersrand for travel funding to the American Geophysical Union Fall (2016) meeting to present this research. To Pablo González Cuadra and Alfred Kroner, I thank you both for providing maps and reports of the Kunene Anorthosite Complex that were otherwise extremely difficult to obtain. To Tsehaie Woldai, thank you for all your advice and teachings on remote sensing, it was great to work with you. To Martin Le Roux, thank you for your valuable assistance in the field and for safely guiding the team through Angola. To Katie Hill and Caitlin Stewart, a great thanks is required for your support and help over the last few years. To staff at UiO, thank you for making me feel welcome in Norway and helping me through my analytical work. Extra thanks to Fernando Corfu for your guidance and inspiration in the world of geochronology, your advice and kindness will be forever appreciated. To the School of Geosciences at Wits University, thank you for the training and learning experience over the years that brought me to this point. To my family, especially my parents, I really appreciate the support and reconcilement during the tough times and all the help throughout my entire education. To Lara Cloete, I could not have completed my Master's degree without you. Your support whether it be emotionally through all the hard bits or someone to celebrate with in the good time is beyond thanks. Most importantly I cannot thank you enough for the countless hours of editing I put you through to help improve my work. To my co-supervisor Jeremie Lehmann, I thank you for the advice, assistance, and help throughout my entire research program. Your way of thinking has definitely taught me new ways to approach problems and their respective solutions. I thank you for the training in the field and hours of commenting, editing, and advice you offered through the years. Lastly to Grant Bybee, this research would be nowhere without you. From 2nd year when you inspired me to become a geologist to the end of my Master's degree, your advice and leadership are to be commended. I thank you for providing the opportunities over the last 2 years where I have learnt so many skills and have improved as a person. It has been a privilege to be your student and I am extremely grateful for your mentorship. I cannot express how much I appreciate your guidance through all the challenges I have faced. You have made this degree exciting and fun to do and it has become one of the greatest life learning experiences I have had. To anyone who has helped in even the smallest way, I thank you.

Contents

List of figures

List of tables

1 Introduction

Bowen (1917) recognized that anorthosites present a particularly unusual problem, in that a rock with a very simple mineral assemblage is associated with many difficult petrogenetic questions. These questions include identification of a parental magma for anorthosites in general, plagioclase concentration mechanisms, emplacement mechanisms, tectonic setting(s), and the temporal restriction of Proterozoic anorthosites (See Sections 1.1 – 1.3 for more specifics; Bowen, 1917; Ashwal, 1993; Ashwal, 2004). These topics have challenged, and continue to challenge, the minds of petrologists. Anorthosites are rocks with a near monomineralogical composition of at least 90% plagioclase (Streckeisen, 1976) and can cover a significant areal extent of up to 20 000 km^2 (Morse, 1982; Ashwal, 1993). Proterozoic anorthosite, the focus of this study, is one of six types of anorthosites (Ashwal, 1993; Ashwal, 2010): Archean (calcic) anorthosite, Proterozoic anorthosite, anorthosite in layered intrusions, anorthosite in oceanic settings, anorthosite inclusions in other igneous rocks, and extraterrestrial anorthosite. Each of these anorthosite types are unique and have distinctive characteristics (Ashwal, 1993). Examples of such characteristics include the temporal restriction of Proterozoic anorthosite, and the occurrence of Proterozoic anorthosite as massifs (large batholiths of anorthosite and related plagioclase rich rocks; Ashwal, 2010). The temporal restriction of Proterozoic anorthosite between ~2.69 – 0.55 Ga (Morse, 1982; Ashwal, 2010) and their highly debated origins (see Section 1.1) create a great desire for study. Proterozoic anorthosites are the most voluminous type of anorthosite on Earth and although they are found from 2.69 – 0.55 Ga, most occur between ~1.8 – 0.8 Ga (Morse, 1982; Ashwal, 1993; Ashwal, 2010). The dominant rock types include: anorthosite, leuconorite, leucogabbro and leucotroctolite, with minor amounts of mafic rock and rare or absent ultramafic rocks (Ashwal, 1993). Typically plagioclase in Proterozoic anorthosites has an intermediate anorthite content of $An_{50 \pm 10}$ with the coarsest grains reaching up to one meter in length. Common among these Proterozoic anorthosites are the occurrence of high alumina orthopyroxene megacrysts of up to 1 meter in length (HAOMs; 2 – 9 wt. % Al_2O_3; Ashwal, 1993).

The Kunene Anorthosite Complex (KAC) in southern Angola and northern Namibia is one of the Earth's largest Proterozoic anorthosite bodies with a mapped surface area of ~18 000 km^2 (Ashwal and Twist, 1993; Mayer et al., 2004). It has been suggested that this anorthositic body is made up of ~10 – 12 coalesced plutons (Ashwal and Twist, 1994). Owing to civil conflict and poor outcrop accessibility in Angola, minimal research has been completed on the KAC, aside from the Zebra Lobe (Figure 1.1) which is the most southern part of the KAC in Namibia (Ashwal and Twist, 1994; Drüppel et al., 2001; Drüppel et al., 2007; Gleißner, 2010a; Gleißner et al., 2010b; Gleißner et al., 2010, Maier et al., 2013).

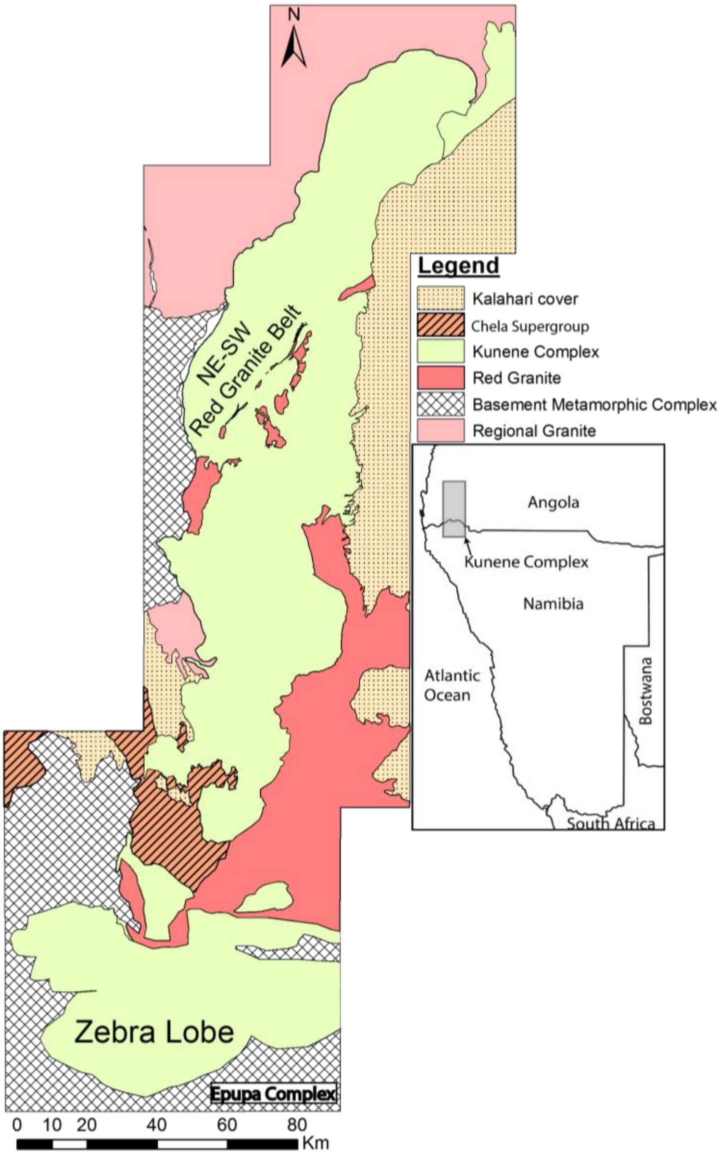

Figure 1.1 – Simplified geological map and outline of the Kunene Anorthosite Complex and its surrounding rocks.

As one of the largest and least studied Proterozoic anorthosites in the world, the KAC provides a unique opportunity to test recent ideas surrounding Proterozoic anorthosite petrogenesis related to the KAC. (See Section 1.5). Its linear geometry, make-up of multiple plutons and large age range also create a great desire for study. This study allows for the development of new models for the emplacement dynamics, timescales, and tectonic setting of the KAC.

1.1 Parental Magma Source for Proterozoic Anorthosites

The major issue still being debated over the last century is the source of parental magmas of Proterozoic anorthosites. Originally consensus on a mantle source with a high silica contamination component was established for the parental magma (Barker, 1975; Ashwal and Wooden, 1983). More recently, however, a second opinion argues for lower continental crust as the magmatic source (Figure 1.2; Morse, 1982; Taylor et al., 1984; Duchesne et al., 1999; Schiellerup et al., 2000; Longhi et al., 2005).

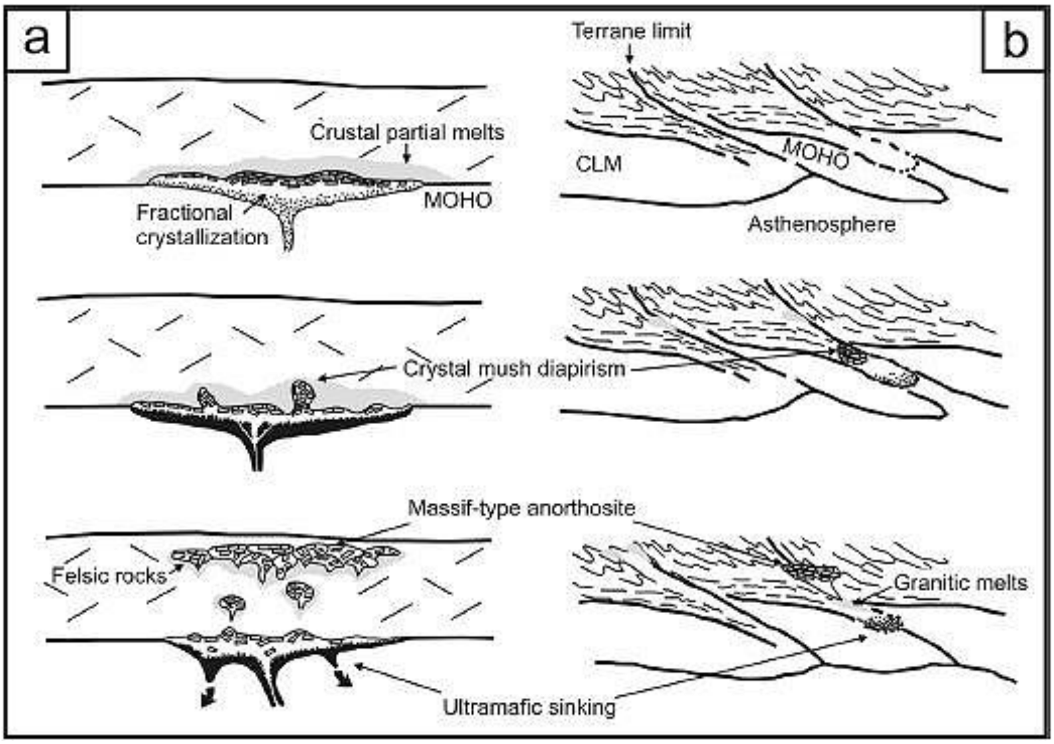

Figure 1.2 - Two models for origin of Proterozoic anorthosites (after Gleiβner, 2010a). (a) Mantle Origin (after Ashwal, 1993) (b) A lower crust origin (after Duchesne et al., 1999).

Based on field observations, petrology, geochemistry, and modelling of Proterozoic anorthosites, an Al-enriched tholeiitic magma is suggested as the likely starting composition in the mantle-derived source models (Morse, 1982; Charlier et al. 2010; Heinonen et al., 2010; Bybee et al., 2014). The role of crustal contamination is a vital process in the mantle source origin and developing magmatic signatures (such as: $\delta^{18}O$ of ~ 7‰, initial Sr ratios > 0.704 and negative εNd values) indicating influences of crustal contamination of an initial mantle magma (Ashwal, 1993; Peck et al., 2010). Associated anatexis of a crustal component also allows for formation of jotunites, monzodiorites, ferrodiorites and granitoids (Morse, 1982; Emsile et al., 1994; Mitchell et al., 1995; Frost et al., 2010; Peck et al., 2010; Bybee et al., 2014). Overall, the model for a mantle source involves partial melting of the mantle to form a tholeiitic magma, this magma ponds at the base of the crust and over time causes anatexis of the crust which is assimilated with the magma (Emsile et al., 1994; Frost, 2010; Heinonen, 2010; Bybee et al., 2014). This magma ascends from the Moho and emplaced as a crustally contaminated magma derived from the mantle (Emsile et al., 1994; Frost et al., 2010; Heinonen, 2010; Bybee et al., 2014).

Recent field and experimental studies have challenged the mantle source hypothesis and favour a mafic lower crustal source as the more preferable source for anorthositic magmas (Taylor et al., 1984; Duchesne et al., 1999; Schiellerup et al., 2000; Longhi et al., 2005). Part of this debate is created by the crustal isotopic signatures which could either originate from a contaminated mantle source (as explained above), or a derivative directly from a lower crustal source. Evidence such as unreasonably high Al compositions, low An content and low Mg# (Taylor et al., 1984), as well as Re/Os isotopic evidence of crustal components within the anorthosite from the Rogaland region, Norway (Schiellerup et al., 2000), are suggested to be incompatible with a mantle parental source. Rather, the observed mineral assemblages and isotopic signatures are more compatible with partial melting of a mafic lower crust (Taylor et al., 1984). In the case of the Gothian Orogeny in Norway, Schiellerup et al. (2000) suggested that γ_{Os} values of +419 would require 610 Ma to evolve from γ_{Os} 0 (the starting chondritic value) to +419. They suggested that a 1400 – 1550 Ma-old lower crustal component could be a likely source for the 930 Ma anorthosites in the Rogaland region and that there is no isotopic evidence to justify a mantle-derived source. This specific crustal source was challenged by Sauer et al. (2013) and produced ε_{Hf} values for the Rogaland anorthosite of +3.8 ± 3 (2σ) which better fits a crust of ~1260 Ma or 1050 – 1020 Ma as more plausible crustal sources. They therefore suggest the 1050 – 1020 Ma aged lower crust as a more preferable source owing to the large volume of rocks in the south western region of Norway at that age. An experimental study involving phase stability of anorthosites at 11 kbar indicates that the parental compositions will fractionate away from the observed mineral assemblages and are not compatible with a mantle source (Longhi, 2005). Longhi (2005) uses this study to reaffirm that only partial melting of mafic lower crust can produce the observed mineral assemblage. A model suggested by Duchesne et al. (1999) shows that anorthosites are associated with crustal weakness zones that extend to Moho depths and that lower crustal "tongues" are underthrust into the mantle, which results in their partial melting (Fig. 1.2b).

Both mantle and lower crust are plausible sources for anorthosite suites. Either the crustal component is an indicator of assimilation of the crust by a mantle-derived magma, or it is a direct component of melting the lower crust (Ashwal, 2004; Bybee, 2013). Although a combination of the two as a mixed source is another possibility. A complete consensus on the question of the source of anorthosites is fundamental as it directly influences the possible types of tectonic environment (Ashwal, 2004).

1.2 Accumulation of Plagioclase and Emplacement Mechanisms

The way in which large volumes of plagioclase are crystallised, and the subsequent emplacement mechanisms, add to the anorthosite problem. The process of plagioclase accumulation can be achieved in essentially two ways: Floatation and accumulation of plagioclase crystals (Morse, 1982; Ashwal, 1993) or crystallisation of plagioclase from a hyper-feldspathic magma (Wiebe, 1990). The mechanical processes of plagioclase accumulation involve ponding of the parental magma at lower crustal levels, plagioclase crystallisation, and subsequent floatation due to the positive buoyancy of plagioclase relative to its host basaltic magma. An experimental study by Kushiro (1980) shows that at pressures lower than 6 kbar plagioclase sinks but at a pressures higher than 6 kbar plagioclase will float relative to its host magma. This allows large volumes of plagioclase to float and accumulate, as well as allowing the minor mafic component to sink and recycle back into the mantle (Ashwal, 1993). A hyper-feldspathic magma in which large volumes of plagioclase can directly crystallize may be formed in different ways. They encompass the existence of an anorthositic liquid (Buddington, 1939), delayed nucleation of plagioclase (Morse, 1982), and formation of a ponded magma where remelting and resorption of preexisting plagioclase enriches the magma and forms a supersaturated hyper-feldspathic magma (Wiebe, 1990). The existence of an anorthositic liquid is implausible owing to unrealistically high temperatures required (~1400 °C), whereas delayed nucleation and super-saturation of plagioclase are more plausible, although further research is required (Ashwal, 1993).

The emplacement mechanism of anorthositic mushes is thought to be similar to that of granitoids with a diapiric rise (a body of magma of a near solid-state crystal mush) which is emplaced into the crust (Ramsey, 1989; Cruden, 1990). This emplacement mechanism and its applicability for anorthosites has been proposed by using finite element modeling (Martignole and Schrijver, 1970; Barnichon et al., 1999). In addition to diapiric ascent, the magma could employ conduit ascent mechanisms where a less viscous magma (as compared to a near solid state diapir) is emplaced into the mid-crust through crustal weaknesses (Royse and Park, 2000).

Geobarometric studies (Emslie, 1975), experimental work (Longhi, 1993), and geochemical modelling (Charlier et al., 2010) are indications that comagmatic High Alumina Orthopyroxene Megacrysts (HAOMs) form at Moho depths of around 35 km. These HAOMs are evidence that diapiric ascent is far too slow to be plausible as the settling velocity of the HAOMs are far too great and the diapir would need to ascend close to eight orders of magnitude faster to be able to support the HAOMs (Royse and Park, 2000). This process assumes plagioclase magma crystallinity is less than 50%. However, a study by Bybee and Ashwal (2015) shows that the anorthosite magma system can reach crystallinity greater than 50%. The increased viscosity of the magma would allow HAOMs to be transported with the diapiric mush even with a slow ascent velocity. Evidence for this is not yet clear and more research is required. HAOMs offer evidence for the onset polybaric crystallisation starting at depths of about 35 km (Emslie, 1975; Charlier et al., 2010; Bybee et al., 2014 and and showing by Valley and O'Neil (1982), $\delta^{18}O$ values of Proterozoic anorthosites from the Adirondack Mountains that indicate a shallow emplacement of the anorthosites at less than 10 km.

1.3 Tectonic Settings

A variety of tectonic settings have been proposed for Proterozoic anorthosites. These settings range from divergent plate margins to continental collision zones and subduction zones, as well as intra-plate settings associated with mantle hotspots (for a full review of tectonic settings, see Ashwal, 1993). Divergent margins were initially a popular tectonic environment for Proterozoic anorthosites. Rift settings allowed for an effective system of magma transportation from the mantle to the base of the crust. The magma could then fractionate and subsequently form anorthositic mushes that were emplaced within the crust (Berg, 1977; Morse, 1982; Ashwal, 2010). Other models include non-uniformitarianism ideas such as supercontinent-derived mantle superswells. The superswells are caused by a stationary supercontinent and subsequent thermal blanketing has been proposed as an additional setting to account for the restricted temporality of Proterozoic anorthosites (Hoffman, 1989). This setting, however, is not appropriate for Proterozoic anorthosites as not all younger supercontinents (e.g. Pangea) are characterised by the presence of these anorthosites (Bédard, 2010). Consensus over the last few years, however, has shifted to convergent settings as a more appropriate tectonic environment (Ashwal 2004, McLelland 2010, Bybee et al., 2014). A collisional setting could account for the linear array seen in these anorthositic bodies in map view, as well as a delivery system of magma to the base of the crust (Ashwal, 2004). While there is significant evidence favouring a converging orogenic setting (Ashwal 2004, McLelland 2010, Bybee et al., 2014), no agreement on the tectonic setting has yet been reached. A more detailed discussion of an appropriate tectonic setting will be discussed in Chapter 4.

1.4 Geological Settings of the Kunene Anorthosite Complex

The KAC is one of the largest and least studied Proterozoic anorthosite complexes in the world (Ashwal, 1993) and is located in southwest Angola with extensions into north western Namibia (Figure 1.1). The KAC intruded along the southwestern margin of the Congo Craton (Silva, 1990; Ashwal and Twist 1994), and has a surface areal extent of 18 000 km^2, extending ~350 km in length and 30 – 50 km in width (Ashwal and Twist, 1994; Mayer et al., 2004). The KAC is emplaced into several different rock types including regional granites in the north (De Carvalho and Alves, 1990), Archean-Paleoproterozoic basements rocks, and Mesoproterozoic rocks of the Epupa Metamorphic Complex (Brandt et al., 2007; Drüppel, 2007) in the west and southern regions respectively. The regional granites are Archean basement rocks and characterised by a large area of homogenous biotite granites (De Carvalho and Alves, 1990). The Archean-Paleoproterozoic basement rocks exhibit a large range of rock-types including gneisses, amphibolites, migmatites, as well as granodioritic and dioritic rocks (De Carvalho and Alves, 1990). The Epupa Complex is a metamorphic complex composed of the Orue Unit and the Empembe Unit which were metamorphosed at around 1330 ± 10 Ma to upper amphibolite and ultrahigh-temperature granulite facies respectively (Brandt et al., 2007; Brandt and Klemd, 2008). The Orue Unit is dominated by migmatitic granitic orthogneisses and a volcano-sedimentary sequence of interlayered mafic and felsic volcanics with migmatitic metagreywackes and minor metapelites (Brandt 2003; Brandt and Klemd, 2008). The Empembe Unit is composed of massive- to weakly-banded, mafic, two-pyroxene granulites interlayered with felsic orthogneisses and orthopyroxene bearing orthogneisses (Brand 2003; Brandt and Klemd, 2008; Gleiβner, 2010). There are extensive Kalahari sands covering part of the eastern margin of the KAC.

The KAC is made up of several anorthositic rock types. These include anorthosite *sensu stricto* (i.e. containing at least 90% of plagioclase), leucotroctolite, leuconorite, and leucogabbro (De Carvalho and Alves, 1990). There are also several granitic bodies associated with the KAC. These granites, referred to as “Red Granites”, occur as a NE – SW orientated belt inside the KAC and large granite bodies that surround part of the KAC (Figure 1.1; Ashwal and Twist, 1994; Morais, 1998; Mayer et al., 2004). The Chela Supergroup overlies the KAC unconformably in the southern part of the KAC (De Carvalho and Alves, 1990). The Chela Supergroup is composed of the Chela Group (a volcano-sedimentary sequence of conglomerate quartzite, sandstone, and felsic volcanics; De Carvalho and Alves, 1990; McCourt et al., 2010), dolomitic limestone of the Leba-Tchamalindi Formation, and a subhorizon of dolerite sills (De Carvalho and Alves, 1990). Dykes of ~1110 Ma commonly cross-cut and surround portions of the KAC (De Carvalho and Alves, 1990; Mayer et al, 2004; Ernst et al., 2013). The economically valuable commodities found within the KAC are occurrences of massive Fe – Ti ore bodies (Villanova et al., 2010; Charlier et al., 2015), and the use of anorthositic blocks as dimension stone.

Initially the studies of the KAC involved reconnaissance mapping at a variety of scales, from more detailed maps of the Namibian portion to regional-scale maps over the entire KAC (Simpson and Otto, 1960; Köstlin, 1974; Silva, 1972). These mapping studies were inhibited however, owing to the civil conflict, the semi-arid desert conditions of the area, and paucity of outcrop. In later years, data collected by the Serviços de Geologia è Minas were used to perform additional mapping at 1:250 000 to 1:100 000 scales, petrography, and geochemical studies of the KAC (De Carvalho & Alves, 1990; Silva, 1992; Menge, 1998). Silva (1990) reported systematic E – W and N – S variations in mineral chemistry and mineral assemblages throughout the KAC. These trends were interpreted to indicate magmatic layering, such as in the Bushveld Complex in South Africa or the Great Dyke in Zimbabwe (Silva, 1992; Menge, 1998). Ashwal and Twist (1994), however, disagreed and found evidence (coarse plagioclase grains, presence of block structures, and a lack of constant compositional trends in the anorthosites, as well as information extracted by satellite imagery) to suggest that the KAC is rather a composite batholith made up of coalesced plutons. More recent thermobarometry and geochemical studies reveal that the Namibian side of the KAC was emplaced at 7 – 9 kbar and likely originated from a mantle magma source owing to its $\delta^{18}O$ values of 5.88 ± 0.19 ‰, with Sr and Nd isotope data ($^{87}Sr/^{86}S$: 0.7039–0.70413 and εNd: 1.1 – 2.0) indicating that the magma underwent crustal contamination (Drüppel, 2001; Drüppel, 2007). Gleißner et al. (2011) showed that in Namibia there are two types of anorthosite: a white (leuconoritic) and a dark anorthosite (leucotroctolitic). They suggested that the white anorthosite is an evolved melt from a mantle source that has undergone fractional crystallisation and significant crustal assimilation, and that the dark anorthosite indicates a later emplacement of a mantle-derived parental melt that only experienced minor crustal assimilation.

1.5 Scope of this Study

This study aims to test new hypotheses related to the understanding and formation of the KAC and offer new interpretations of the emplacement dynamics, magmatic timescales, and tectonic setting.

The overarching working hypotheses of this studies are:

1) Enhanced satellite imagery will reveal spectral information about the KAC in relation to its composition and structure and allow for the creation of a new geological map of the KAC.

2) The KAC has similarly long-lived magmatic emplacement processes as other Proterozoic anorthosites around the world.

This dissertation assesses the applicability of using remote sensing techniques (more specifically, Landsat 8 and SRTM data) for creating new, detailed geological maps of magmatic bodies, in this case, the KAC. In Chapter 2, it is shown how the use of image processing techniques such as false colour composites, band rationing, principle component analysis, and a minimum noise fraction can enhance the Landsat 8 data and allow for interpretation of different spectral domains. For the SRTM and principle component 1 data, an automatic lineament extraction was used to map the regional scale lineaments through the KAC. In Chapter 3 newly obtained U-Pb ID-TIMS data were used to test whether there is any genetic link between the composition and age of the spectral domains within the KAC, what timescale the KAC is formed over, and develop a model for the emplacement of the KAC. Finally Chapter 4 shows the integration of the results from the remote sensing mapping and geochronology studies to suggest a new conceptual model for the petrogenesis and tectonic settings of formation of the KAC and Proterozoic anorthosites in general.

2 Mapping the Kunene Anorthosite Complex: A Remote Sensing Approach

2.1 Introduction

The Kunene Anorthosite Complex is one of the largest and least studied Proterozoic anorthosite complexes in the world with minimal mapping compiled mostly by Serviços de Geologia e Minas de Angola, De Carvalho and Alves (1990), and Menge (1998). Although these maps show a good general depiction of the surrounding geology of the KAC, they show little detail within the KAC itself. Where the geological maps have slightly more detail of the KAC itself (Figure 2.1), issues such as inconsistent transition of geological features across map sheets and changes in map legends (depending on the map publishers) are common.

Remote sensing has become a popular technique for fast and informative mapping over large areas and holds promise for better imaging and mapping of magmatic complexity in the extensive KAC. Alone, remote sensing is an important first order interpretive tool, but when combined with ground validation it becomes a much more valuable technique. The aim of this contribution is to perform a remote sensing analysis of the KAC, in combination with ground truthing, to understand fundamental compositional variations and the magmatic architecture of one of the world's largest Proterozoic anorthosite complexes, and to characterize the extent of the KAC.

2.2 Material and Methods

Landsat 8 OLI (Operational Land Imager) and SRTM 3 (Shuttle Radar Topography Mission) data of the Angolan portion of the KAC have been obtained from the US Geological Survey Earth Resources Observation and Science Centre (http://earthexplorer.usgs.gov) on the 10th of September 2015 (Figure 2.2a). 3 Landsat 8 tiles (rectangles covering an area of 185*180 km each) and 8 SRTM tiles (1 degree latitude by 1 degree longitude each) were chosen to cover the entire KAC. Landsat 8 data were chosen because of the better spectral resolution per band and higher number of bands than previous Landsat datasets. Additionally, fewer Landsat tiles are required to cover the KAC, and therefore less processing is required compared with other available products (such as Aster data). Image processing was performed using the computer programs: ENVI, ArcGIS, ILWIS, Global Mapper, PCI Geomatica, and Rockworks.

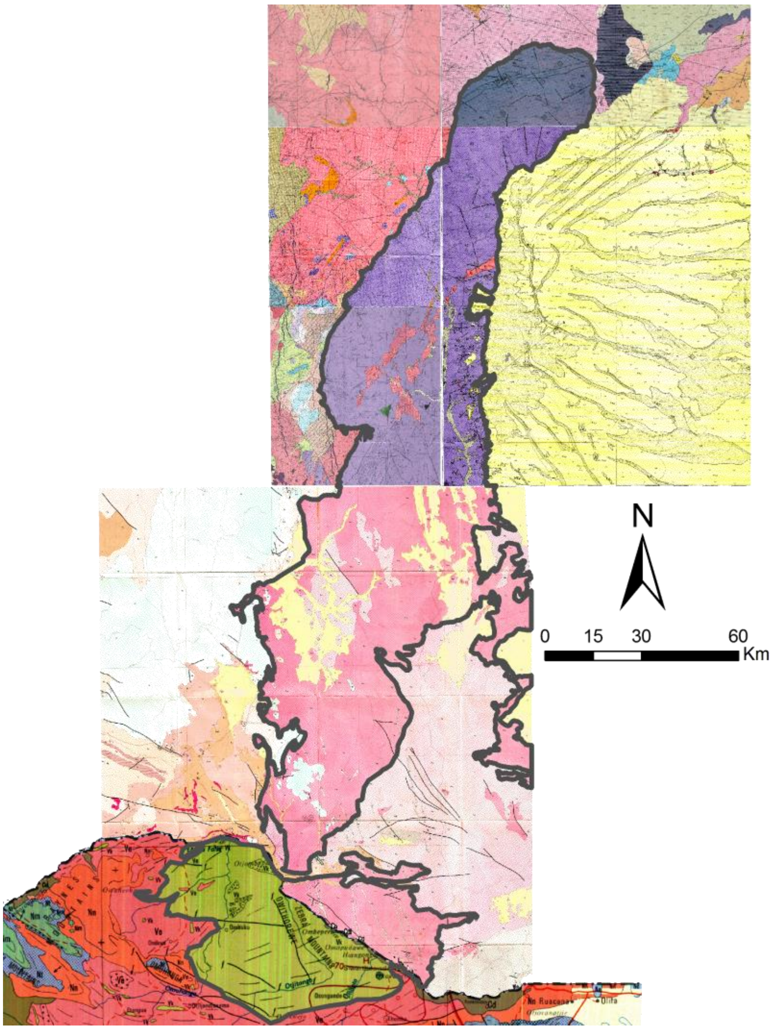

Figure 2.1 - Mosaic of geological maps of the Kunene Anorthosite Complex (compiled from Serviços De Geologia E Minas De Angola maps: SUL D-33 T-II & SUL D-33 T-IV, SUL D-33 U, SUL D-33 O and SUL E B-C-H-I; Miller and Schalk, 1980). The grey outline shows the published extent of the KAC.

The multiple image enhancement methods used in this study, and the rationale for using them, are outlined in Figure 2.2 and described below. They encompass False Colour Composite (FCC), Minimum Noise Fraction (MNF), Principle Component Analysis (PCA), and band ratioing for the Landsat 8 data as well as hill-shading and automatic lineament extraction for the SRTM data. These processing methods were used to achieve the best image detail and contrast, to enhance the geological units and structures of the area.

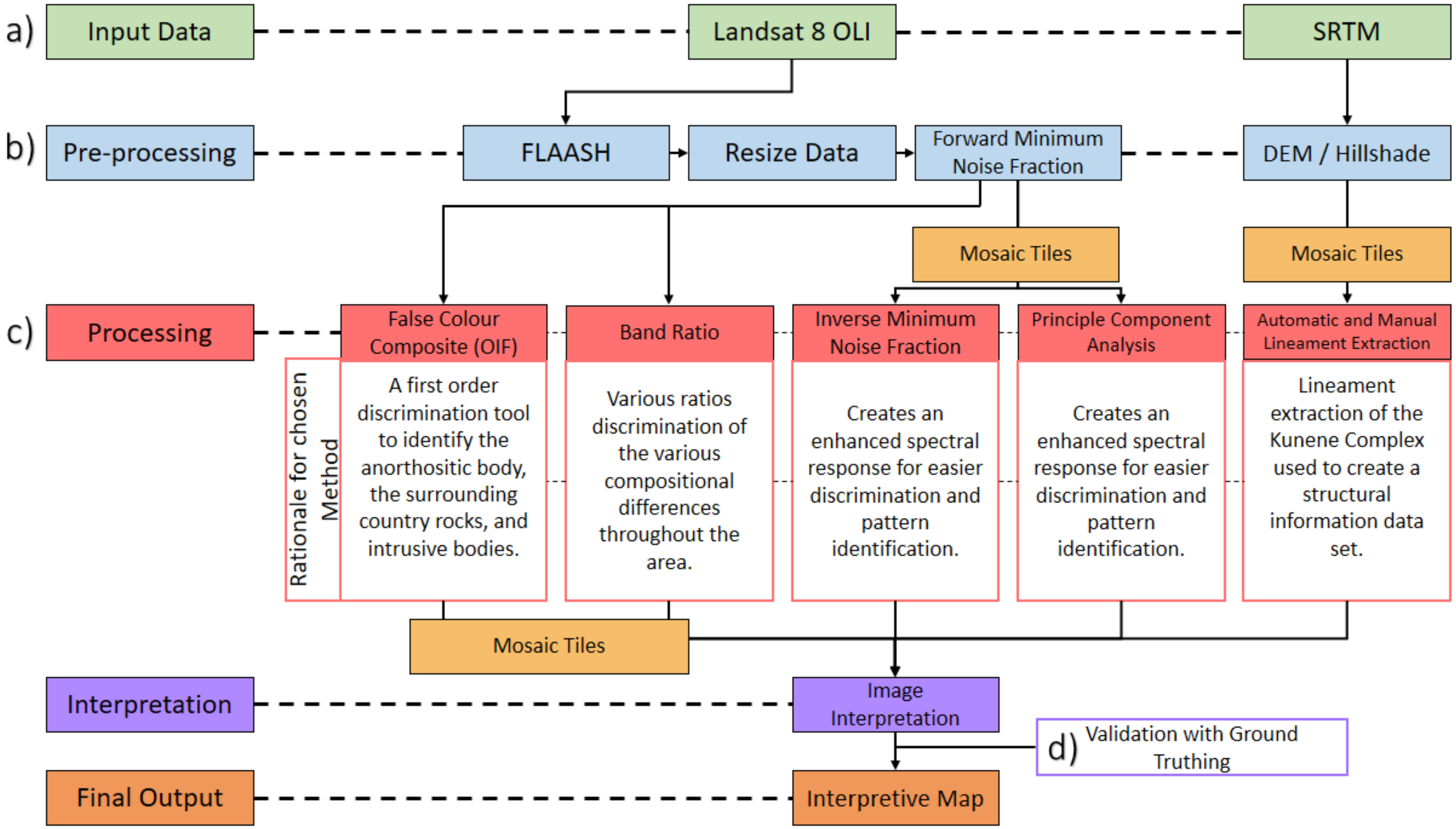

Figure 2.2 - Workflow diagram showing the methods employed and processing chain involved in image processing. See text for details.

2.2.1 Pre-processing Methods

2.2.1.1 Landsat

The pre-processing of the image was done by a three step method chain (Figure 2.2b): 1) A FLAASH (Fast Line-of-sight Atmospheric Analysis of Spectral Hypercubes) atmospheric correction was used to produce a more accurate estimation of the true surface reflectance (Felde et al., 2003; Perkins et al., 2005; Owojori & Xie 2005). This was done by removing the effects of the atmosphere (namely water vapour and aerosols) that alter the true surface reflectance (Matthew et al., 2002). 2) Clipping of the data to remove spectral signals outside the area of interest, allowing for a greater stretching of image pixel values of target areas. 3) The use of an inverse MNF from estimated statistics in a forward MNF process. This is used to identify and remove bands with the most noise and enable noise reduction in the final surface reflectance image (Green et al., 1988; Kruse 1996; Waldhoff et al., 2004; Harris et al., 2006).

2.2.1.2 SRTM

Eight SRTM version 3 DEM (Digital Elevation Model) image tiles were obtained to cover the entire study area. The DEM data are at 1-arc second spatial resolution (~30 meter resolution) and were hillshaded and seamlessly mosaicked in Global Mapper to highlight the surface lineament data.

2.2.2 Image Processing Methods

The resultant image of the pre-processing was used as the base image for further processing and enhancement (Figure 2.2c). All Landsat processed tiles were mosaicked using ENVI software. The FCC and band ratio data were mosaicked after individual tile processing and the outcome of the image processing was not affected by the mosaicking process. The PCA and MNF images were mosaicked before the image processing in order to keep a consistent and seamless spectral response output, as the PCA and MNF processes will change depending on the total data within each image. Multiple colour composites were made as a first order discrimination tool to identify the different rock-types in the area. A true colour composite of bands 4, 3 and 2 in Red Green Blue (RGB), and multiple FFCs such as Bands 6, 4 and 1 in RGB were chosen to best represent the signal responses. The FCC bands used were based on an Optical Index Fraction (OIF) calculation, which calculates the optimal combination of three bands out of all 7 individual

Landsat OLI bands, and shows the highest amount of information in bands with the least amount of redundant data.

The PCA and MNF methods were chosen as techniques in which the image data can be transformed for easier discrimination and pattern identification (Jolliffe, 2002; Gupta et al., 2013). The PCA transformation is able to compress data by eliminating redundancy between bands of the image in a way that combines similarities without loss of information from the image data. This is achieved by transforming the dataset into a new set of components (principle components – PCs), which are uncorrelated and orthogonal variables to each other (Jolliffe, 2002). The PCs are ordered so that the first PC contains the most data variability and the second to last PCs contain progressively less data and variability. The MNF is a similar transformation to the PCA, except the data components are ordered in decreasing signal to noise ratio (Green et al., 1998). The MNF transformation is comprised of two PCA transformations. The first is based on estimated noise statistics of the data in order to reduce the noise in the image and the second is a regular PCA transformation of the noise-reduced data (Green et al., 1998; Harris et al, 2006). The resultant images of both PCA and MNF allow for more simple discrimination of the image and later classification processes.

Band ratios 4/2, 6/5, and 6/7 of the Landsat dataset were used to enhance areas of ferric, ferrous, and OH-minerals respectively (Drury 2001; Gad & Kusky 2006; Mshiu 2011; Ali & Pour 2014; Pour & Hashim 2015). The ratios were combined into a RGB image to enable discrimination of the various compositional differences.

2.2.3 Automatic Lineament Extraction

Automatic lineament extraction is performed on both elevation data from the SRTM image and optical data of the PC1 band from the processed Landsat image. The LINE function of PCI Geomatica 2016 was used to extract linear features from the imagery and convert them into vector lines. The LINE algorithm consists of 3 steps: 1) an edge detection process to convert the images into an edge strength image, 2) thresholding of the edge strength image to assign an ON/OFF value to each pixel in the image, and 3) a curve detection to extract and link all possible curved features (PCI Geomatica Manual, 2016). Both extracted lineaments of the SRTM and PC1 images were processed and overlain on top of each other to combine matching, and to fill in missing, lineaments. Lastly, manual editing of the data was done to remove any lineaments that were interpreted as geologically unrelated (i.e. roads, railways, and farming-related patterns). In addition to identification of lineament data, hydrology tools (basin fill → flow direction → flow accumulation → stream order) were utilised in ArcGIS to extract the river networks from the DEM image over the study area.

2.2.4 Ground Truthing

Two field expeditions (2015 and 2016) to the Angolan portion of the KAC allowed for sample collection and structural measurements throughout the KAC. This ground truthing process (Figure 2.2d) allows for the validation and additional interpretation of the satellite images. The geological interpretation of Landsat 8 imagery was supported by field observations on 193 reference points and was complemented by assessing a group of thin sections (see Section 2.3.1.1) that are representative of all rock types occurring in the study area. All 135 thin sections and geochemical data (Appendix B) collected by the project team were briefly assessed and detailed analysis of a representative selection of the samples was used to confirm spectral responses of the satellite signals. This representative selection is described in Section 2.3.1.1.

2.3 Results

2.3.1 Rock-types and their Spectral Signatures

Field geology as well as an overview of collected thin sections allows for identification of the different rock types that make up the KAC and the surrounding country rocks. These rocks show distinct, individual spectral responses. The rock-types, their descriptions (section 2.3.1.1.), and their spectral responses are shown in Table 2.1. The processed images and ground truthing database of each rock type are shown in Figures 2.3a – e. The multispectral images indicate regions of homogenous signal responses and were correlated with field samples, which have been separated into individual domains based on differing spectral signatures and their relating ground validation. The processed images allow for identification of several domains (7 in Angola and 2 in Namibia; Figure 2.3c).

Table 2.1 - Characteristic spectral response signals of individual rock-types for the processed images, where the band ratio and MNF 234 images show the most useful data.

Rock Type	Rock Description and Common Characteristics	FCC 641 (Figure 2.3a)	Band Ratios (Figure 2.3b)	PCA 234 (Figure 2.3c)	MNF 234 (Figure 2.3d)
Anorthosite	Commonly coarse-grained (cm-scale) rock with dark grey euhedral plagioclase crystals. Minor interstitial mafic phases are present and include mainly olivine, orthopyroxene, clinopyroxene, and magnetite (or a combination thereof). Plagioclase is commonly sericitized.	Medium brown to brown-purple at outcrop locations. Purple-blue to white at weathered surfaces.	Light green at outcrop locations. Dark blue at weathered surfaces.	Light purple at outcrop locations. Cyan-green at weathered surfaces.	Brown-green at outcrop locations. Yellow-pink at weathered surfaces.
Leucotroctolite	Medium- to coarse-grained rock. Plagioclase is dark grey and euhedral. Olivine and clinopyroxene are common mafic interstitial minerals with an occasional occurrence of orthopyroxene. Both pyroxenes occasionally rim the olivine grains. Olivine weathers to a brown-red colour (iddingsite). Plagioclase is commonly sericitized.	Medium brown to brown-purple signal.	Strong cyan signal with a faint light green in the northern portion of the complex. In the southern portion it shows as a bright lime green signal.	Strong light green signal with a faint purple in the northern portion of the complex. In the southern portion it shows as a medium - dark purple signal.	Strong magenta signal with a faint brown-green in the northern portion of the complex. In the southern portion it shows as a medium - dark green signal.
Leuconorite (LN) Leucogabbro (LG) Leucogabbronorite (LGN)	Medium to coarse-grained rock. Plagioclase is dark grey and euhedral. LN - orthopyroxene is the common major mafic interstitial mineral with minor clinopyroxene. LG - clinopyroxene is the major mafic interstitial mineral. LGN - clinopyroxene and orthopyroxene are similar in proportions and are the common mafic interstitial minerals. There is also an occasional occurrence of olivine in various samples. High Aluminium Orthopyroxene Megacrysts are common and range from 10 cm – 0.5 m.	Medium brown to brown-purple signal.	Pale sea green signal.	Magenta-purple signal.	Brown-green signal.

Table 2.1 (cont.) - Characteristic spectral response signals of individual rock-types for the processed images, where the band ratio and MNF 234 images show the most useful data.

Rock Type	Rock Description and Common Characteristics	FCC 641 (Figure 2.3a)	Band Ratios (Figure 2.3b)	PCA 234 (Figure 2.3c)	MNF 234 (Figure 2.3d)
Metasomatized Anorthosite	Fairly inhomogeneous rocks that are medium to coarse grained. Plagioclase occurs as large white cumulus euhedral crystals (4 – 5 cm) as well as smaller crystals (~1 cm). Minor interstitial mafics are present. Orthopyroxene can sometimes been seen as brown interstitial crystals in hand samples. Rocks are commonly altered and epidotised in places.	White signal with blue or purple undertones as well as a sea green signal in flatter regions.	Dark blue signal as well as purple-blue or purple-green signals in weathered regions.	Light and dark blue signals as well as a yellow-green signal in weathered regions.	Yellow and purple signals as well as a purple-blue signal in weathered regions.
Red Granites	Medium grained rock composed of mainly quartz and K-feldspar. Appearance of rock is distinctly reddish in colour owing to weathering products of iron rich minerals. In some places the granite is strongly foliated.	Beige-maroon signal.	Reddish yellow signal.	Red-maroon signal.	Cyan signal.
Syenite	Phenocryst of K-feldspar (~ 2cm) in a quartz and K-feldspar matrix. Bleb like networks of hornblende occur throughout and are commonly altered to chlorite. The rock is red in colour (hematisation), and is sheared and brecciated in places.	Beige-maroon signal.	Pale green-yellow signal.	Magenta signal.	Dark purple-cyan signal.
Regional granite	Coarse-grained granite composed of K-feldspar (pinkish in colour), quartz and hornblende. Rock is fairly homogeneous.	Beige-maroon signal.	Peachy-orange signal.	Green-red signal.	Light and dark blue signals.

Table 2.1 (cont.) - Characteristic spectral response signals of individual rock-types for the processed images, where the band ratio and MNF 234 images show the most useful data.

Rock Type	Rock Description and common Characteristics	FCC 641 (Figure 2.3a)	Band Ratios (Figure 2.3b)	PCA 234 (Figure 2.3c)	MNF 234 (Figure 2.3d)
Metamorphic Basement Complex	A Complex made of various rock types including: granodiorite, migmatites, granite gneisses, metasedimentary units, and metavolcanic units.	Predominantly brown-yellow signal with some brown-green.	Predominantly green signal with some oranges, reds, and yellows.	Predominantly purple-pink signal with some oranges, reds, and dull greens.	Predominantly light and dark blue signals with some green and brown.
Capping Unit	A capping unit composed of the Chela Supergroup and dolerite.	Reddish brown and green-yellow signals.	Light green and pink-yellow signals.	Magenta and lime green signals.	Dark purple and brown-green signals.
Alluvium	N/A	Dark Blue and green signals.	Black and dark purple signals.	Black and dark green signals.	Bright yellow and lime green signals.
Kalahari Cover	N/A	Various brown signals.	Pale purple and yellow (Lime green fire scars) signals.	Pale purple and yellow (dark purple fire scars) signals.	Dark purple and blue (Lime green fire scars) signals.
Cross Cutting Dykes	N/A	Red-brown signal.	Cyan signal.	Magenta signal.	Dark purple signal.

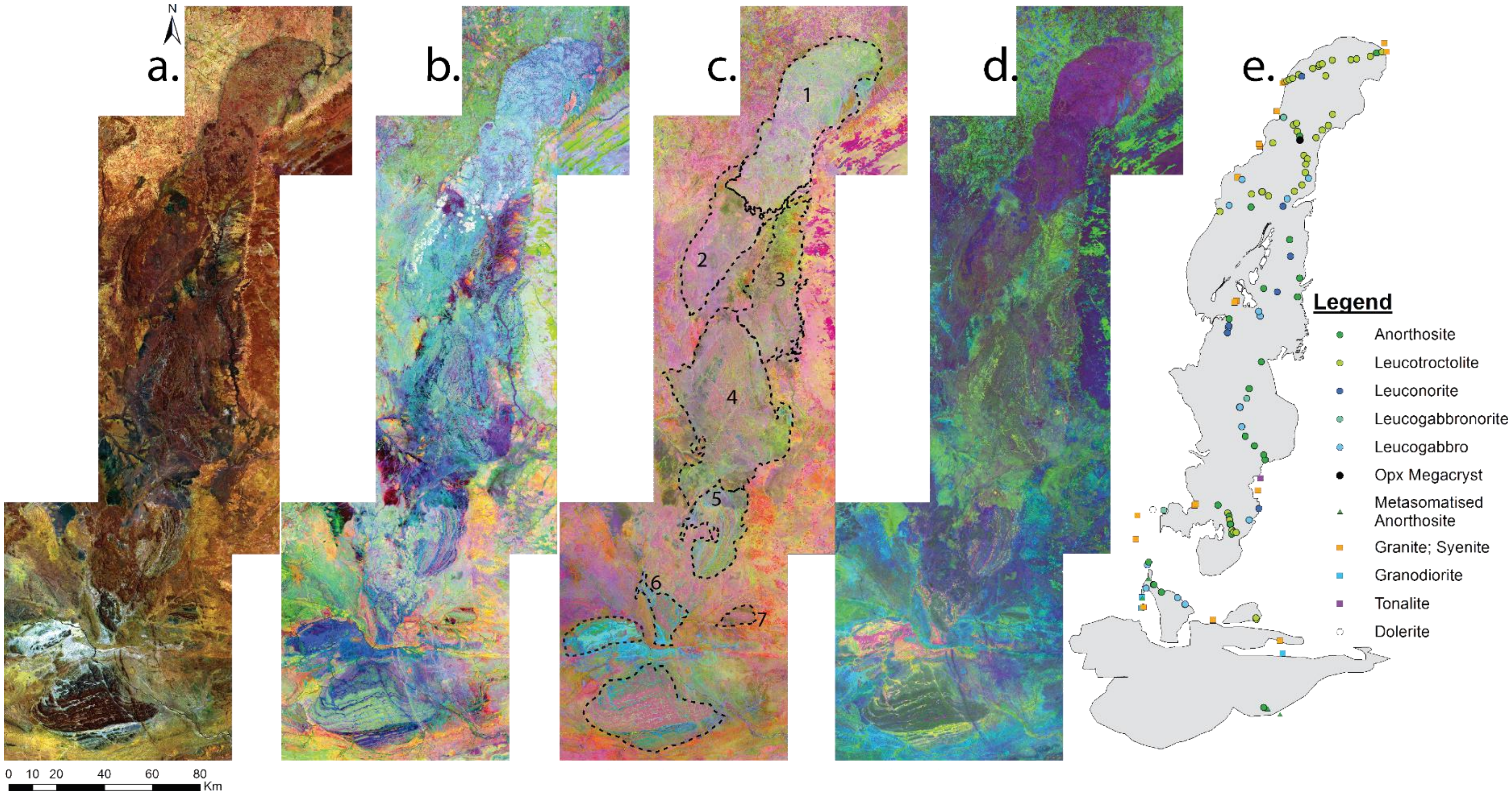

Figure 2.3 - Results of image processing of Landsat 8 data: a) FCC of bands 641 in RGB, b) Colour composite of band ratios 4/2, 6/5, and 6/7 in RGB, C) PCA with bands 234 in RGB. Newly defined domains are indicated by dashed lines (those located in Namibia are not discussed in the text), d) a MNF with bands 234 in RGB, and e) an outline of the KAC showing ground truthed samples and their rock-types.

Although all image processing methods (FCC, Band Ratioing, MNF, and PCA) used were useful in determining various domains and changes in spectral signals, the most useful image processing techniques were the band ratio image and the MNF 234 image. These image provide the best contrast and details in the KAC.

2.3.1.1 Representative rock types of the KAC

The representative sample descriptions of rocks in and around the Kunene Anorthosite Complex are shown below. These samples depict a representative appearance of the main rock types described in Table 2.1 that were used for ground truthing of the spectral signals seen in the processed Landsat 8 imagery.

12/14 – Leucotroctolite (-16.991294 S, 13.914362 E)

This sample is a medium to coarse grained rock, with average grain size ranging from 4 – 5 mm. The weathered surface of the rock is brown in colour while the fresh surface appears to be dark grey and black (Figure 2.4a). Moderate foliation of the mafic minerals are present. Plagioclase (80 %) occurs as cumulus grains. Plagioclase grains are commonly sub- to euhedral, with some grains in the outcrop reaching up to 5 cm in length. Olivine (15 %) is present as anhedral interstitial grains and subhedral grains, and is commonly rimmed by orthopyroxene. Phlogopite, magnetite and ilmenite make up the minor phases (5 %) of this sample (Figure.2.4b).

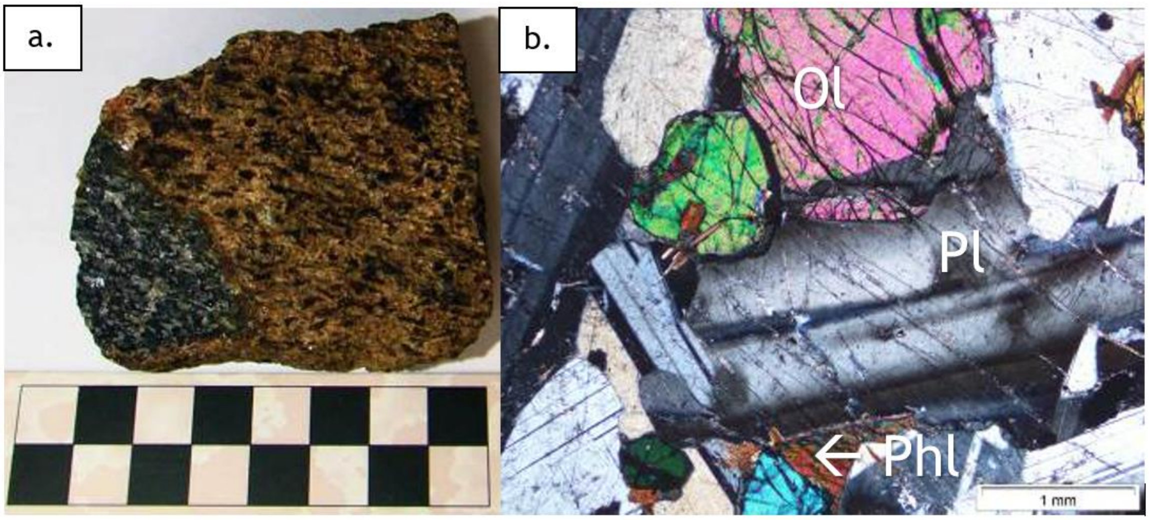

Figure 2.4 – Sample 12/14: a) Hand sample (1 cm scale blocks), b) microphotograph (cross-nicols) of same sample.

57/55 – Leucogabbronorite (-16.61172 S, 13.88787 E)

This sample is a fine to medium grained rock (1 – 5 mm) and is brown in colour on the weathered surface, with dark greys and black on the fresh surface. The sample is mostly homogenous (Figure 2.5a). Major phases includes plagioclase (60 %), clinopyroxene and orthopyroxene (~ 20 % each) and minor phases of biotite and opaque minerals. Plagioclase occurs as sub- to euhedral cumulus grains. The pyroxenes commonly fill the interstitial spaces (Figure 2.5b).

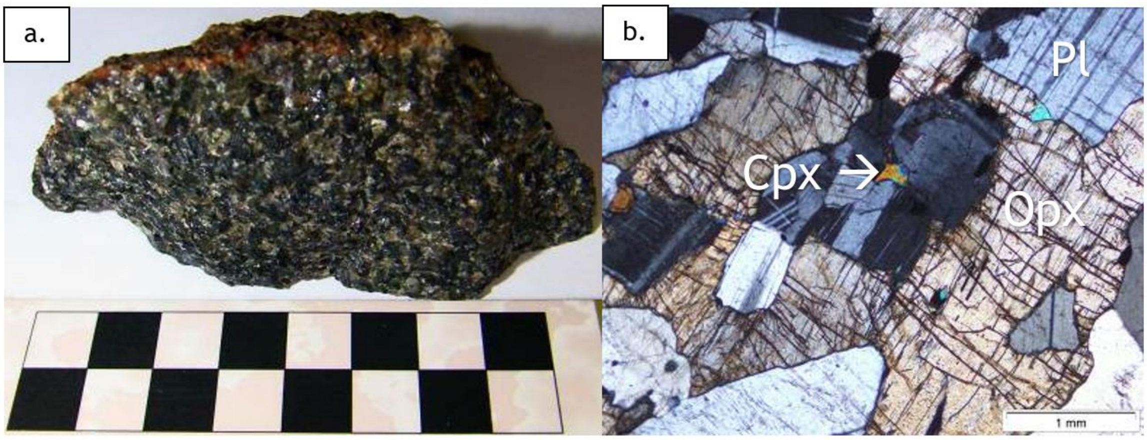

Figure 2.5 – Sample 57/55: a) Hand sample (1 cm scale blocks), b) microphotograph (cross-nicols) of same sample.

67/65B – Leucogabbro (-16.258059 S, 13.861273 E)

This sample is a medium to coarse grained rock (2 – 5 mm). The rock has a brown colour on weathered surface. The fresh surface ranges from greys to black with some reddish brown minerals. There are patches of pegmatitic areas of plagioclase and clinopyroxene in the outcrop that grade into finer grained portions (Figure 2.6a). Major phases include plagioclase (75 %) and clinopyroxene (23 %). Biotite and opaque minerals occur and minor phases (2 %) Clinopyroxene occurs as interstitial networks between the coarse and fine grained plagioclase grains. The clinopyroxene is occasionally kinked (Figure 2.6b).

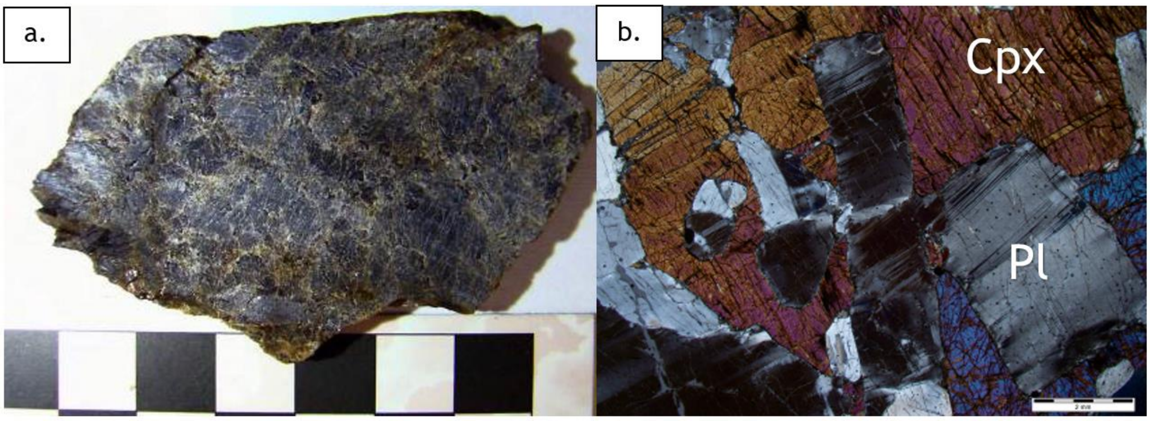

Figure 2.6 – Sample 67/65B: a) Hand sample (1 cm scale blocks), b) microphotograph (cross-nicols) of same sample.

003/002 – Metasomatasied Anorthosite (-17.332119 S, 13.956332 E)

The sample is coarse grained that is white and green on the weathered surface (Figure 2.7a). The rock is made up 90 % of large white cumulus euhedral plagioclase crystals (up to 5 cm) and smaller plagioclase (~1 cm) crystals with ~10 % interstitial mafic minerals (orthopyroxene and ilmenite and/or magnetite). The rock is fairly inhomogeneous and is altered, metasomatised and epidotised in places (Figure 2.7b).

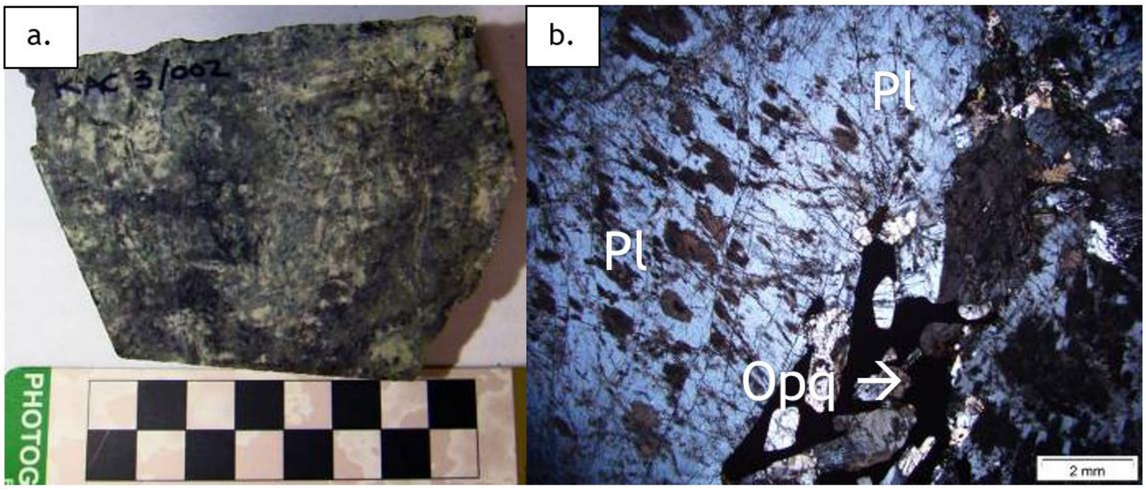

Figure 2.7 – Sample 003/002: a) Hand sample (1 cm scale blocks), b) microphotograph (cross-nicols) of same sample.

31/35 – Granite "Red Granite" (-16.941510 S, 13.469986 E)

Rock is red in colour owing to strong hematisation of the sample (Figure 2.8a). The rock is medium to coarse grained and composed of quartz (55%) and K-feldspar (43 %) with large

K-feldspar phenocrysts in places. Common minor phases minerals are biotite (~2 %) and lesser chlorite (<1 %) There are areas of heterogeneous deformation throughout the rock in the outcrop. Quartz and K-feldspar are commonly recrystallized and also occur as a granophyric texture (Figure 2.8b).

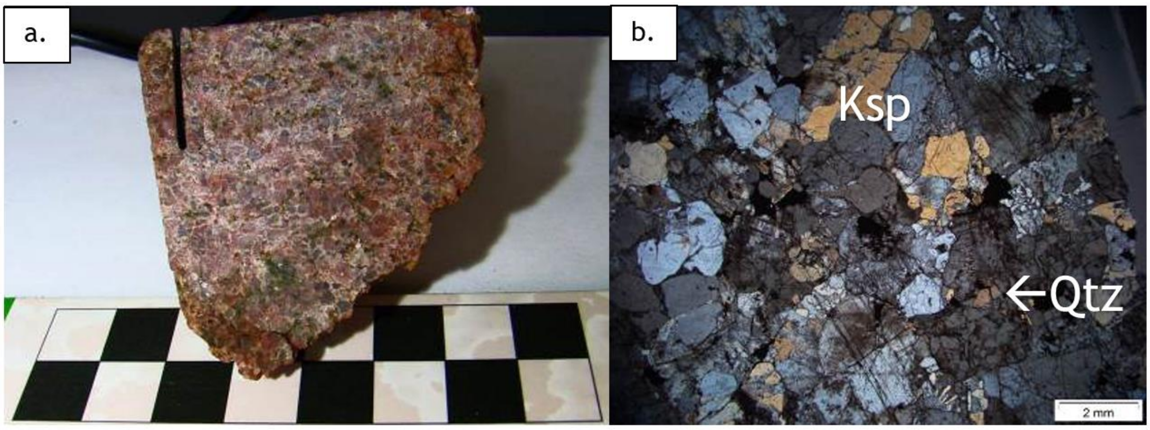

Figure 2.8 – Sample 31/35: a) Hand sample (1 cm scale blocks), b) microphotograph (cross-nicols) of same sample.

__**39/40** – Porphyritic Dolerite (-16.576120 S, 13.556150 E)__

Fine grained rock (~1 mm matrix) with euhedral plagioclase phenocrysts (up to 6cm in outcrop). Rock is dark brown on the weathered surface and black on fresh surface (Figure 2.9a). The matrix is made up of sub- to euhedral grains of plagioclase (55 %) and anhedral to subhedral grains of olivine (45%; Figure 2.9b).

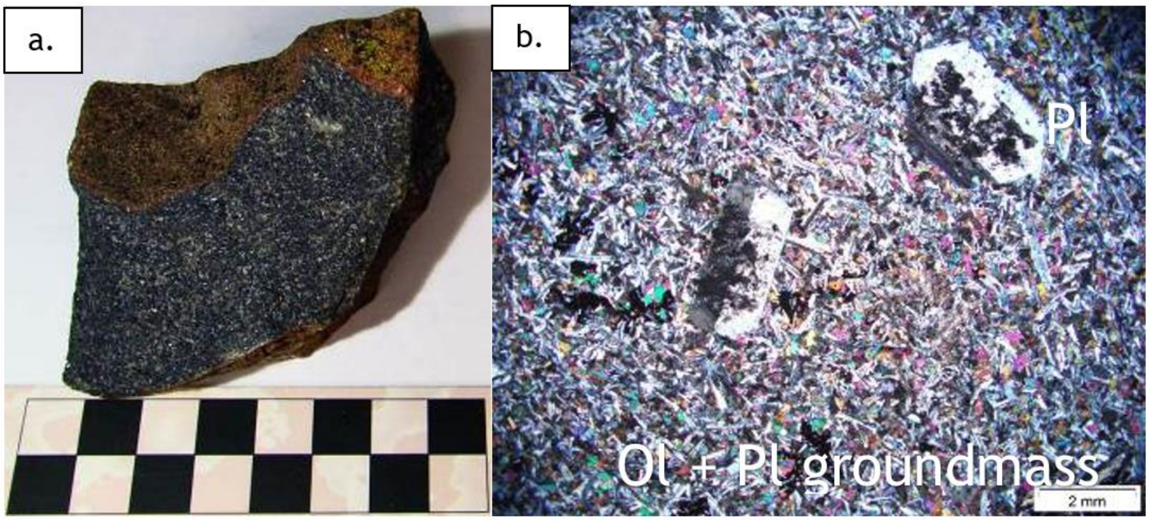

Figure 2.9 – Sample 39/40: a) Hand sample (1 cm scale blocks), b) microphotograph (cross-nicols) of same sample.

<u>62/59</u> <u>– Granodiorite (-16.454342 S, 13.933262 E)</u>

Fine grained rock with a light grey colour as the fresh surface (speckled with dark green and black minerals) (Figure 2.10a). The major minerals are quartz (45 %) and plagioclase (40 %) with lesser K-feldspar (10 %). Minor phases (5 %) occur as biotite, muscovite and opaque minerals. Sample is relatively homogenous with an equigranular texture. In outcrop there are areas of migmatitic banding (Figure 2.10b).

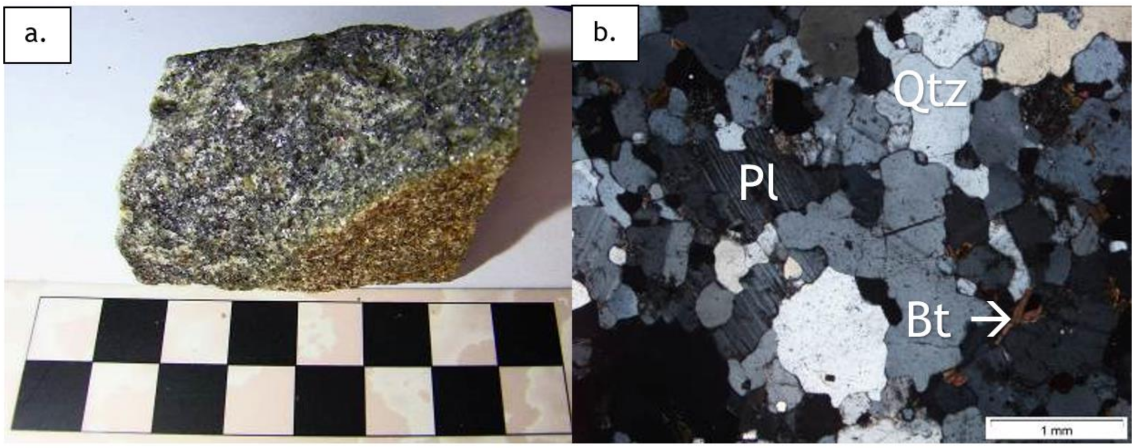

Figure 2.10 – Sample 62/59: a) Hand sample (1 cm scale blocks), b) microphotograph (cross-nicols) of same sample.

2.3.1.2 Spectral domains of the KAC

Using the relation between rock-type and spectral response (Table 2.1), the dominant spectral signal response of each domain (Figure 2.3c) and relating rock-type is described below:

Domains 1 and 2 are dominated by a leucotroctolitic signal (as per ground-thruthing, Table 2.1 and Figure 2.3e). These best seen in the MNF 234 (Figure 2.3d) image as a purple signal. Domain 1 is separated from domain 2 because the former shows a strong OH signal in the band ratio image (Figure 2.3b).

Domain 3 is difficult to see in its entirety owing to alluvial cover. With the small areas of signal response available and subsequent ground validation, it is apparent that the domain represents a more anorthositic domain (*sensu stricto*) with minor occurrence of leuconoritic rocks. Domain 3 is best seen in the band ratio image (Figure 2.3b) as the mixed dark purple and orange colour of the alluvial cover with a more solid blue-green signal to the south.

Domain 4 is best identified using the MNF 234 (Figure 2.3d) image. It shows the general green to brown-green signals of the anorthosites, leucogabbros, and leuconorites of the domain.

Domain 5 is a more heterogeneous domain with mostly anorthosite, but also occurrences of leuconorite, leucogabbro, and leucotroctolite. This domain is best seen in the FCC 641 image (Figure 2.3a; area of a more green, yellow, and cream coloured oval) and band ratio image (Figure 2.3b; lime green, blues, and purple signals).

Domain 6 is best depicted in the MNF 234 (Figure 2.3d) and the PCA 234 (Figure 2.3c) images. In the MNF image the leucogabbroic and anorthositic signals show up as green to brown colours, with a pink-orange signal for the weathered area around it. In the PCA image there is a pink to green colour signal with a blue weathered area around it.

Domain 7 is most prominent in the FCC 641 (Figure 2.3a) and band ratio images (Figure 2.3b). The leucotroctolitic domain shows up as lime green in the band ratio image and a dark brown surrounded by brown-green signals in the FCC image.

2.3.2 Internal Architecture of the Kunene Anorthosite Complex

Using the various processed images in combination with ground truthing, it is possible to further separate the KAC into not only domains of broadly similar spectral responses (Figure 2.3 above), but also to identify lineaments within these spectral domains. Using an automated lineament extraction process (with some manual refining, see Section 2.2.3), lineaments were assigned to the individual domains identified above in Figure 2.3 using the spectral data (Figure 2.11). These domains differ in their shape and areal surface, as well as in the direction of the lineaments throughout the KAC.

Described below is the map shape of each domain as well as each of the domains internal lineaments geometry from north to south:

1) Domain 1 is elliptical in shape along its western, eastern, and northern contacts where it is adjacent to the regional granites. The Landsat imagery, shows that the entire eastern contact is covered by sediments of the Kalahari Supergroup. The southern contact with domain 2 is marked by a WNW – ESE trending irregular contact (Figure 2.12). Domain 1 is divided into two sub-domains. In the northern

part of the domain, the processing extracted a fewer amount of lineaments than in the south. Here, the lineaments are generally oriented at high angle to the main NNE-trending long axis of the KAC showing an east-west trend and deflecting along the northern contact of domain 1 in a WNW – ESE trend (Figure 2.13-1a). In the southern part of domain 1, lineaments are more abundant and they generally show a NNW – SSE trend with a few east-west trending outliers (Figure 2.13-1b).

2) The external contact of domain 2 is straight to slightly westward-convex on its western and southern margin where it is in contact with country rocks. The domain shares its northern WNW – ESE-trending irregular contact with domain 1 and its eastern contact is shared with the NE – SW trending belt of Red Granite. Blebs of what shows up as similar signal responses to that of the rim in domain 1 signal appear irregularly throughout the northern portion of domain 2 (Figure 2.5). A large proportion of lineaments in this domain are oriented in a NNW – SSE trend with minor deflections in either direction (Figure 2.13-2). These lineaments are (sub-)parallel with the western contact of domain 2.

3) Domain 3 lies between the Red Granite belt on its western contact and Kalahari sedimentary cover to the east. Its shape is irregular and controlled by its surrounding rocks. The major lineament direction is NNW – SSE with minor outliers on the eastern portion of the domain showing a NE – SW trend (Figure 2.13-3).

4) Domain 4 has an N – S elongated oval shape. This domain is in contact with Red Granite to the north and east, metamorphic basement and regional granite to the west, and domain 5 to the south. The lineaments broadly define a NNW – SSE-trending maximum with some spread to the NNE and NW (Figure 2.13-4). These lineaments are commonly cross-cut by NW – SE trending lineaments (Figure 2.11 b).

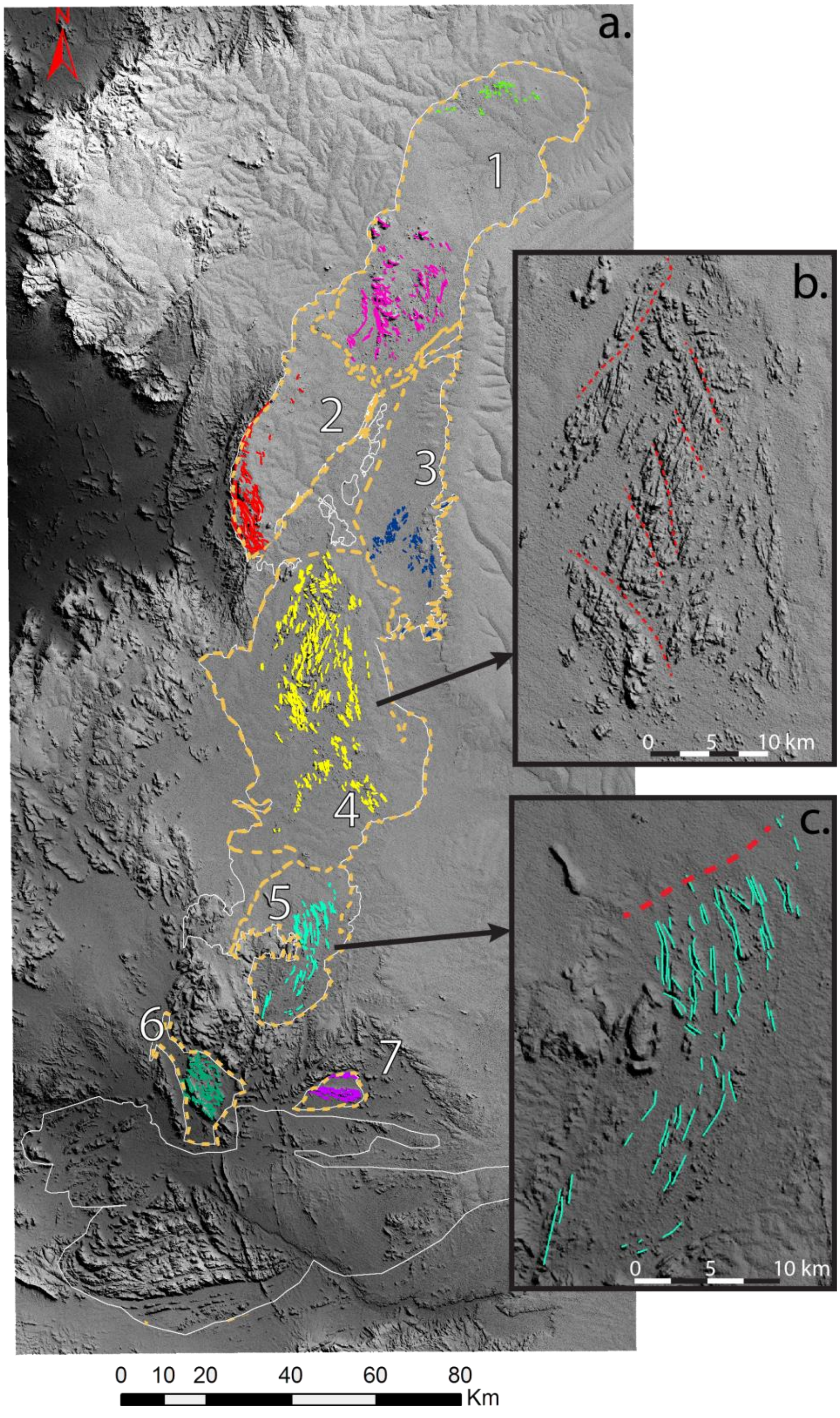

Figure 2.11 - a) A Mosaick of SRTM 3 DEM image of the KAC overlain by automatically extracted lineaments. Lineaments belonging to different compositional and multispectral domains are grouped into different colours. Domains are outlined in orange and numbered 1 – 7. The white outline shows the extent of the KAC b) Zoomed in area of domain 4 showing lineaments cross cutting higher frequency NNE – SSE-trending lineaments. c) Zoomed in area of domain 5 showing termination of lineaments.

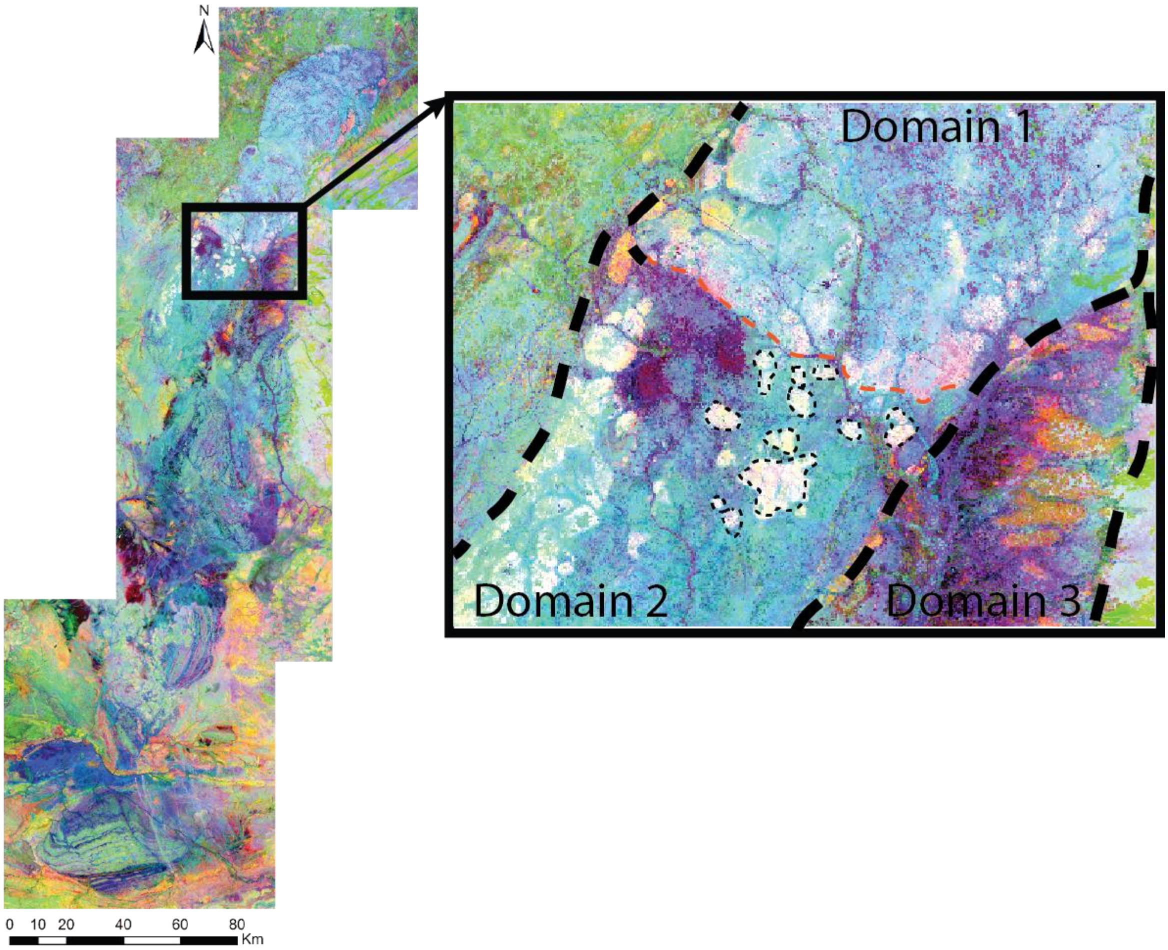

Figure 2.12 - Band ratio image of bands 4/2, 6/5, and 6/7 as RGB showing: 1) the WNW – ESE trending irregular contact between domain 1 and 2 (red dashed line) and 2) blebs (thin black dashed lines) which have the same signal response as the rim signal responses in domain 1. These blebs appear irregularly throughout the northern portion of domain 2.

5) Domain 5 shows an oval like shape (Figure 2.11 c). To the east, the domain is rounded and in contact with Red Granite rocks. To the west and south the domain is covered by capping rocks of the Chela Supergroup. To the north the domain is in contact with domain 4. The lineaments are slightly curved: on the north of the domain they trend in a NNW – SSE direction, in the centre they trend in a N – S direction, and in the southern part of the domain they are NNE – SSW trending (Figure 2.13-5). The lineaments are terminated by a NE – SW trending lineament.

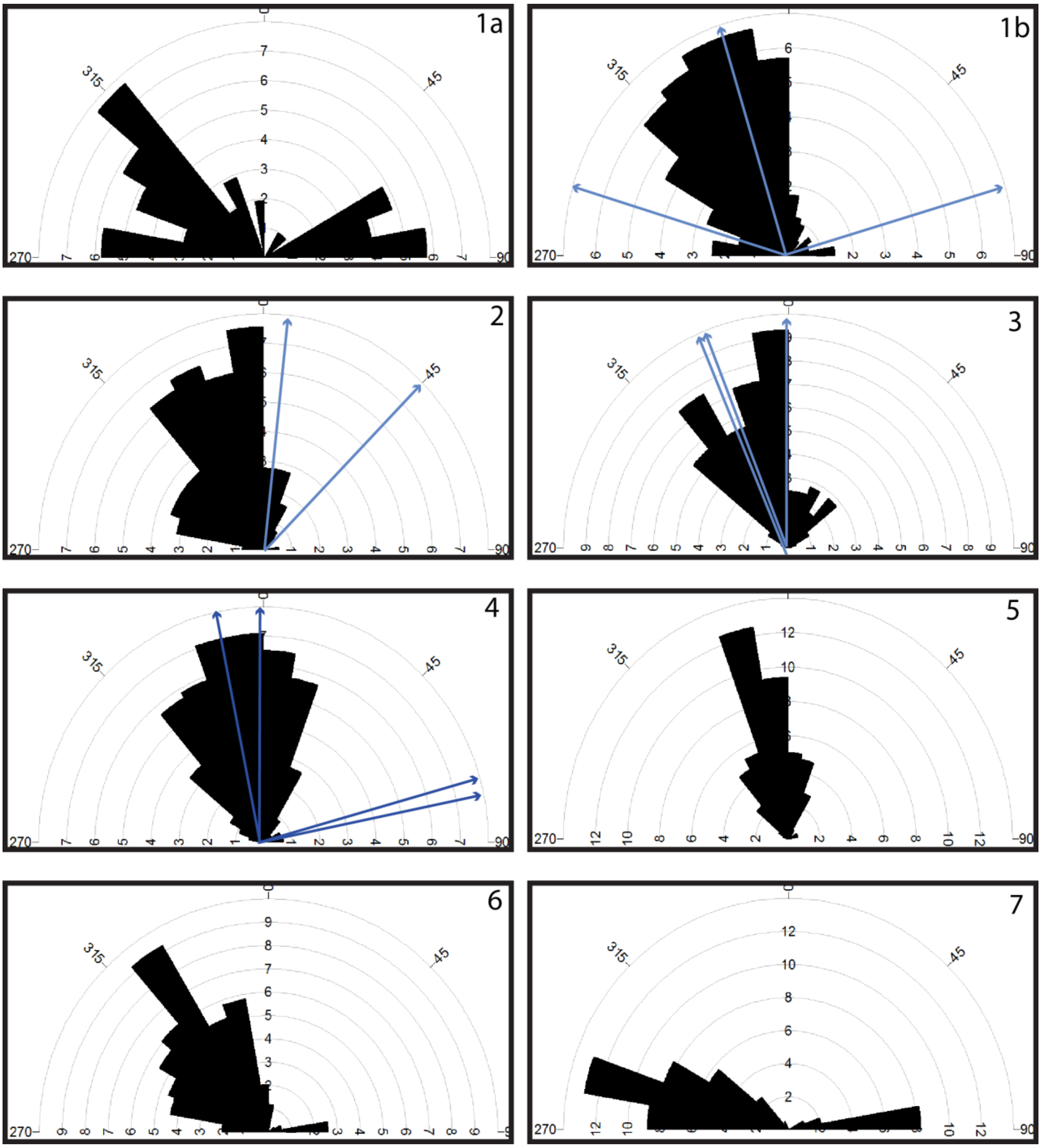

Figure 2.13 - Rose diagrams for lineaments within each domain (Petal length is based on frequency of lineament occurrence of the total domain population, Bin size of 5°). The azimuth of field measurements of steep magmatic foliations are shown as solid blue arrows.

6) Domain 6 has an irregular shape with a more squared off southern edge, and northwest extending elongate portion for the western and northern edges. The domain is surrounded by the capping unit to the north and east, and by

metasomatic anorthosite, a unit of Red Granite and metamorphic basement rocks to the southwest. The lineaments show a strong NNW – SSE trend (Figure 2.13-6).

7) Domain 7 has a pinched-out oval shape and is surrounded by Red Granite rocks to the north, west and east, and metasomatic anorthositic rocks to the south (Figure 2.13-7). The lineaments display a general WNW – ESE trend that contrasts strongly with the other domains.

2.4 Discussion

2.4.1 A Revised Geological Map of the Kunene Anorthosite Complex

The internal architecture and compositional differences of the KAC and its surrounding rocks can be extracted from the processed images. New data presented in this study can be summarized in three major parts: 1) Linking the various spectral responses to specific rock-types in order to map the geology of the complex and adjacent country-rocks, 2) characterizing the geometry and nature of the margins of spectrally homogeneous domains, and 3) presenting new data on the internal geometry of these domains.

2.4.2 Discrimination of Various Rock Types

As seen throughout the processed image data there are notable differences in spectral responses between the surrounding country rocks and the KAC itself. This, as a first order discrimination, allows for easy separation and classification of the KAC and country rocks. Figure 2.14a shows an example where blue signals in domain 1, and green to blues in the other domains, represent the KAC and are easily distinguishable from the peachy orange signals of the surrounding regional granite. The green signals overlaying the peachy orange signals overlap well with the river network (extracted from DEM) and its alluvial deposits. Accordingly, the green signals are interpreted as a cover overlaying the regional granite.

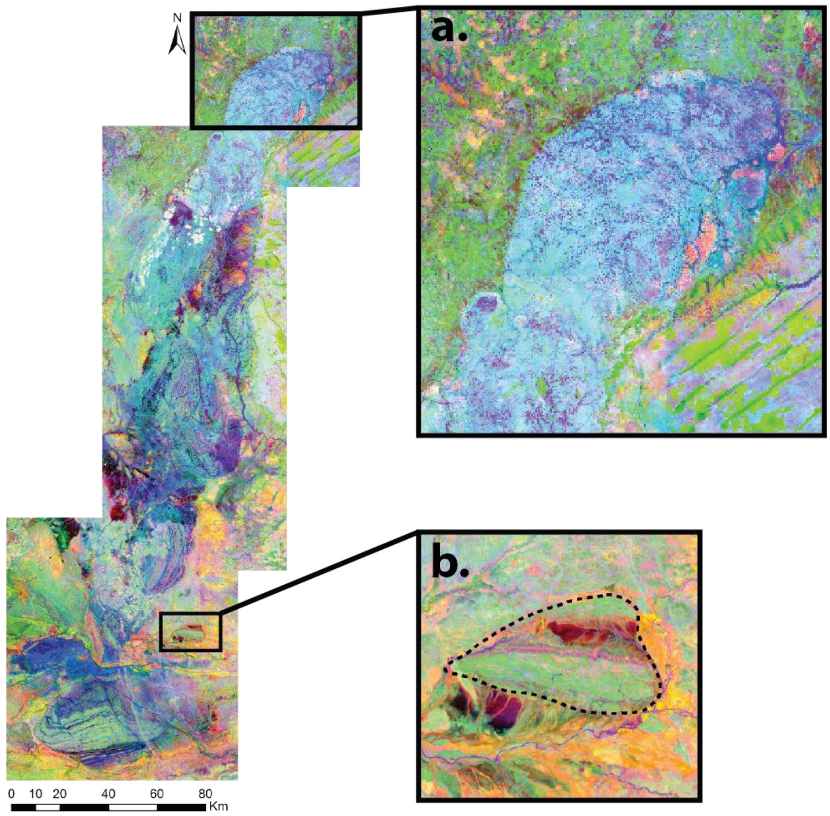

Figure 2.14 - Band ratio image of bands 4/2, 6/5, and 6/7 as RGB used for a) distinguishing the KAC (blue signals) from the surrounding country rock (orangey peach signals) and b) a leucotroctolitic domain (small green signaled body) surround by metasomatised anorthosite to the north (purple-green and Red Granite to the south (orange-yellow).

Current published maps stop at this level of detail, as they do not show the internal geological differences in the KAC. Using the Landsat 8 dataset it is possible to discriminate between the different rock types that make up the complex. These spectral responses are confirmed by ground truthed data (field survey and petrographic analyses) to reinforce this classification. The classification is a two-step process in which the multispectral response data are correlated with ground samples of that response. In general, the northern portion of the KAC (domains 1 and 2, north of the NE – SW trending Red Granite belt, Figure 1.1) is more leucotroctolitic in composition (with rare occurrences of orthopyroxene), whereas in the southern portion (south of the NE – SW trending Red Granite belt) there is an increase in the proportion of orthopyroxene-bearing rocks and the KAC is generally more leuconoritic (Figure 2.15). Exceptions to this pattern are a small satellite body to the east of the southern portion of the KAC which is leucotroctolitic (Figure 2.14b), and the Zebra lobe of the Namibian portion of the Complex, which shows alternating layers of leuconorite and leucotroctolite.

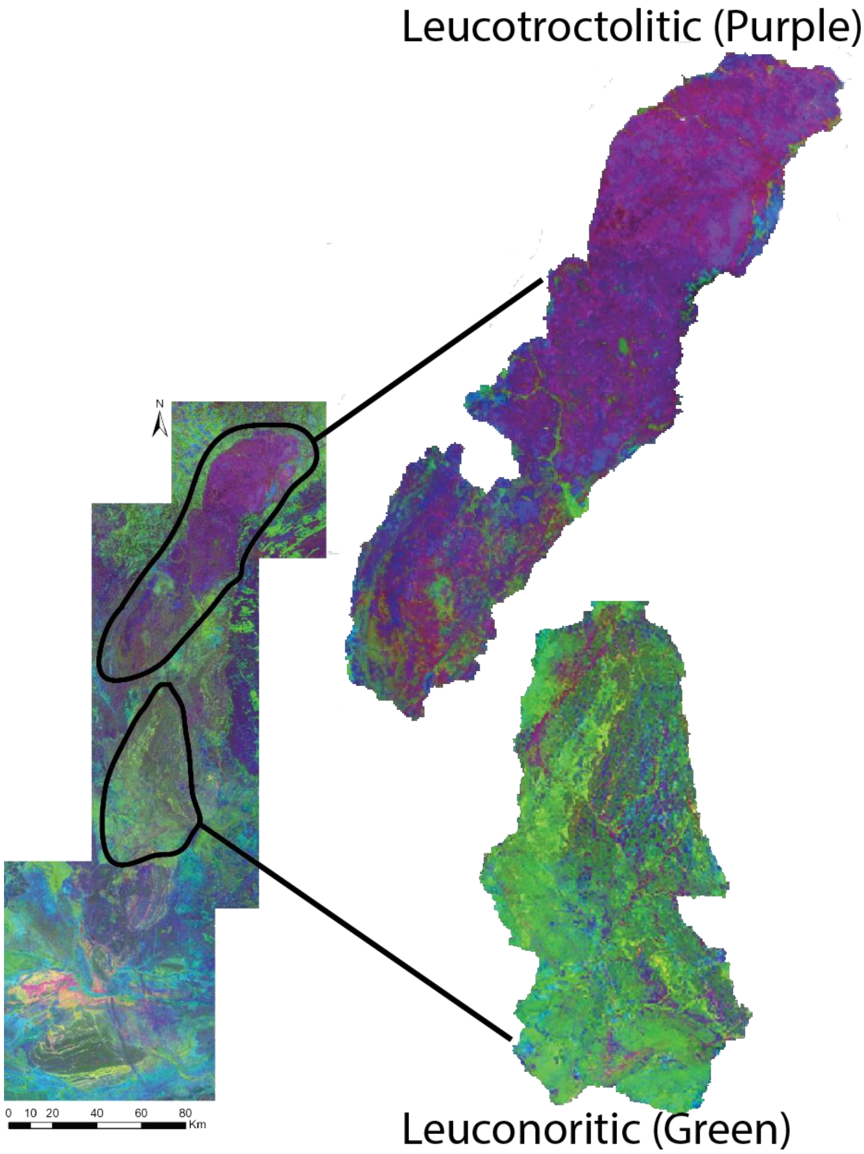

Figure 2.15 - The MNF image (bands 234 in RGB) shows a clear signal difference between the leucotroctolitic area (purples) and the leuconoritic areas (greens), separated by the Red Granite belt.

Further discriminating features are evident in the image data. Domain 1 shows a strong signal for an OH-signature. This is best seen in the Band Ratio image (Figure 2.16) as a more dominant blue signal compared with the green-teal signals of the rest of the KAC. This representative signal can be interpreted as an area of enhanced sericitization of plagioclase, which is a common alteration phase seen in anorthositic bodies.

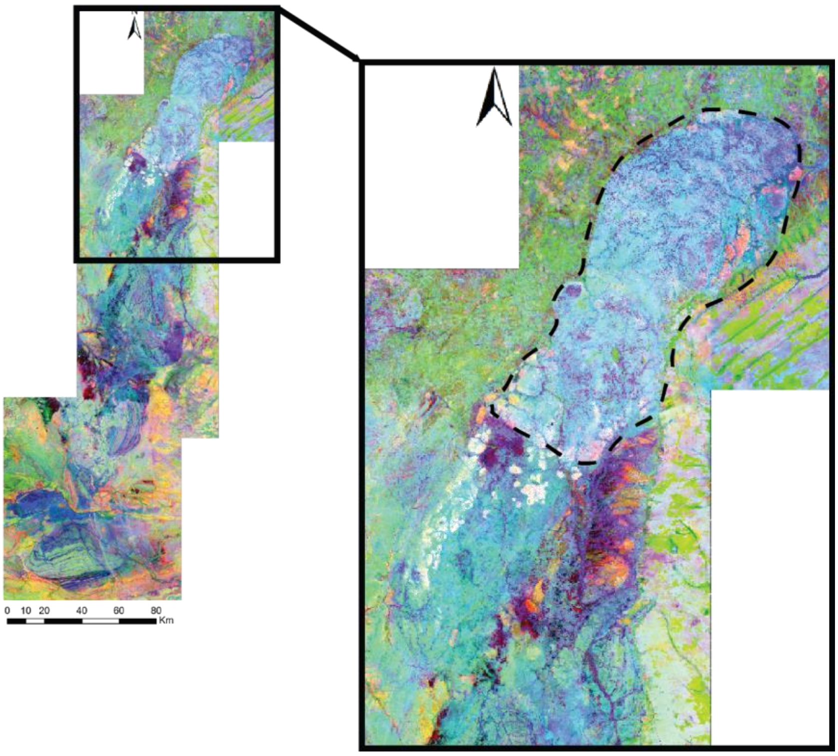

Figure 2.16 - Band ratio image of bands 4/2, 6/5, and 6/7 as RGB showing the different spectral signals of the OH-dominated area (bluer signal, shown in dashed lines) compared to the remainder of the Complex which shows a more greenish teal colour.

2.4.3 Geometry and Lineaments

The lineament data provides a good first order indication for the orientation of the regional-scale lineaments seen in the SRTM and PC1 data throughout the KAC. Lineament orientation for most of the domains coincide well with field measurements of magmatic foliations (Figure 2.13), although local outliers (e.g. domains 1b, 2 and 4) probably suggest that outcrop-scale variations in the geometry of the magmatic foliations are not recorded by the remote sensing. The field description of magmatic foliations at outcrops is further supported by micro-scale observations. This allows for the classification of most of the SRTM and PC1 lineaments (following the similar overall trend of the KAC lineations) as magmatic foliations (Figure 2.17).

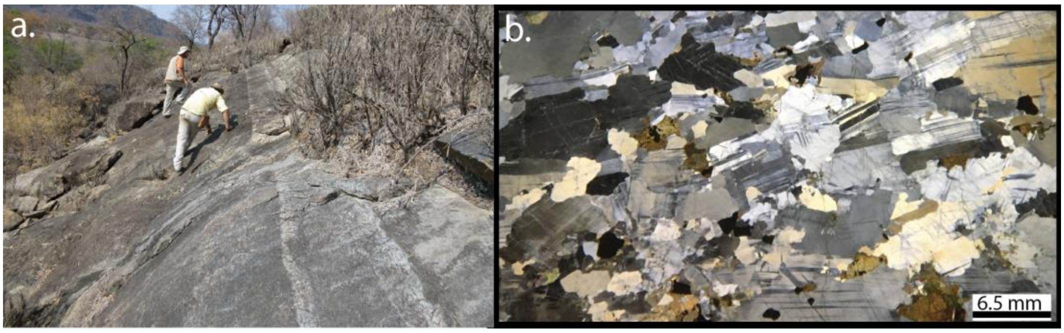

Figure 2.17 - Example of magmatic foliation from the northern portion of domain 4 in the KAC (sample: 146/141c; 15.8790S, 13.8111E) (a) Photograph of locality where a 50 cm-wide leuconorite layer alternates with more anorthositic layers. At the outcrop, all layers are continuous along strike. (b) Microphotograph (cross-nicols) from the same outcrop where elongated and oriented plagioclase, orthopyroxene, and magnetite mark the magmatic foliation. The magmatic foliation is parallel to m-scale anorthosite/ leuconorite layering. Grain boundaries of plagioclase are irregular owing to subsolidus recrystallisation.

The lineaments of the KAC shows an overall N – S to NNW – SSE trend. Deflections of this trend are generally located at the margins of the domain are following the trend of the adjacent country rocks. The pattern is similar to that described by Paterson et al. (1998) for a marginal-type magmatic fabric pattern. These fabric patterns could be due to similar conditions as described by Royse and Park (2000), whereby the rocks emplaced into the cold Archean basement rocks (the regional granites of the KAC) should display more undeformed margins; whereas the rocks emplaced into thermally softened hosts (such as the metamorphic basement complexes) have more deformed margins (Royse and Park, 2000). Other controls could be that the lineaments are (sub-)parallel to the long axis of the elongate-shaped domains(Paterson et al., 1998), or to pre-KAC regional structural trends.

A few lineaments show much wider spacing and don't follow the trend than the magmatic lineaments (km spacing vs. 100 m spacing). They are interpreted as faults (Figure 2.11b). When using regional scale satellite images, it is generally not possible to identify and classify sub-solidus structures in the KAC. This is because they are only observed at the outcrop- and micro-scales (e.g. the sub-solidus recrystallization visible in Figure 2.17 b) and do not form sufficiently thick rhythmic layers of different compositions to be depicted with Landsat and SRTM data.

Two possible interpretations can be inferred from the lineament and spectral images: 1) there is a decrease in the density of mapped lineaments from the northern to the southern domains and 2) orientations of lineaments in the northern domain are more scattered than in the south (Figure 2.11). Multiple factors can influence the distribution of outcrops and also the fact that the northern domains are less well-exposed than the southern ones. A strong argument could be made for differential weathering of the rocks in the KAC. Goldich (1938) showed that, in general, the weathering sequence (Figure 2.18) would be opposite to that of the crystallisation order (Bowen's reaction series; Bowen, 1922).

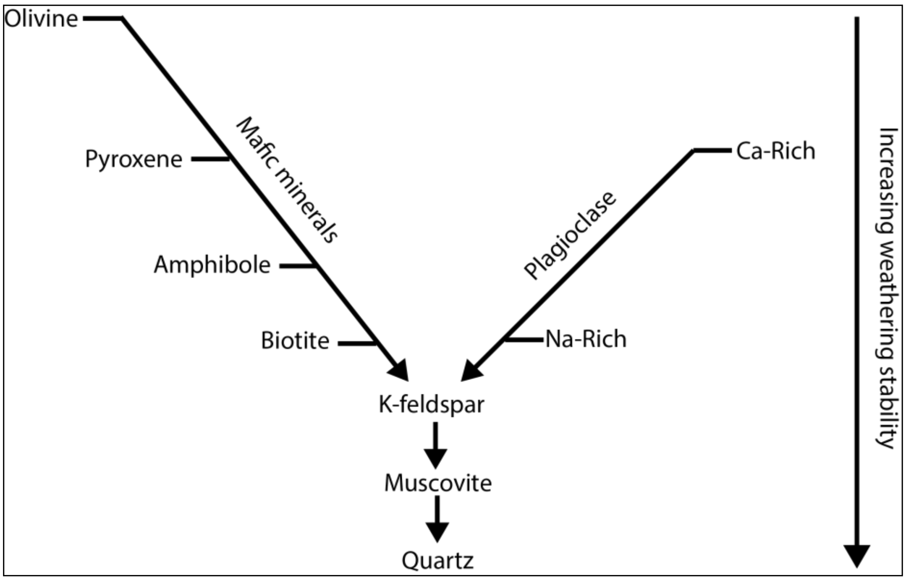

Figure 2.18 - Generalised weathering stability of common minerals (modified after Goldisch, 1938).

This would provide one explanation as to why the northern leucotroctolitic domain displays less outcrop than the southern leuconoritic domain. In addition, or alternatively, factors that could affect the outcrop distributions are: 1) topographically, the northern domains are at a higher altitude, which gradually decreases over the length of the KAC towards the south with a total elevation change of about 350 meters. The difference in topography could result in different weathering/erosion rates along the length of the complex. 2) There is a general decrease in exposure and proportion of outcrops as the distance increases away from the escarpment. This is most evident in domains 1 and 2. The increased proportions of lineaments are likely owing to the formation of the escarpment (Huila Plateau; Lopes et al., 2016), post KAC emplacement. (3) Outcrop exposure in the more central and southern portions of the KAC is also largely controlled by the river networks running through these domains. An example can be seen with domain 3(Figure 2.19a), which shows extensive alluvial cover from the crosscutting river of this domain. In the southern portion of the KAC, nearing the Kunene River, the outcrop exposure is greater owing to the eroding river (Figure 2.19b). 4) A final idea is that the difference in density and distribution of outcrops is related to the compositional difference of the domains. Domains 1, 2, and 7 of the complex are largely more homogeneous and isotropic whereas the remaining domains are more heterogeneous (as seen in domain 4) where leucotroctolite or leuconorite are intercalated with anorthosite, and are commonly foliated (e.g. Figure 2.17a)

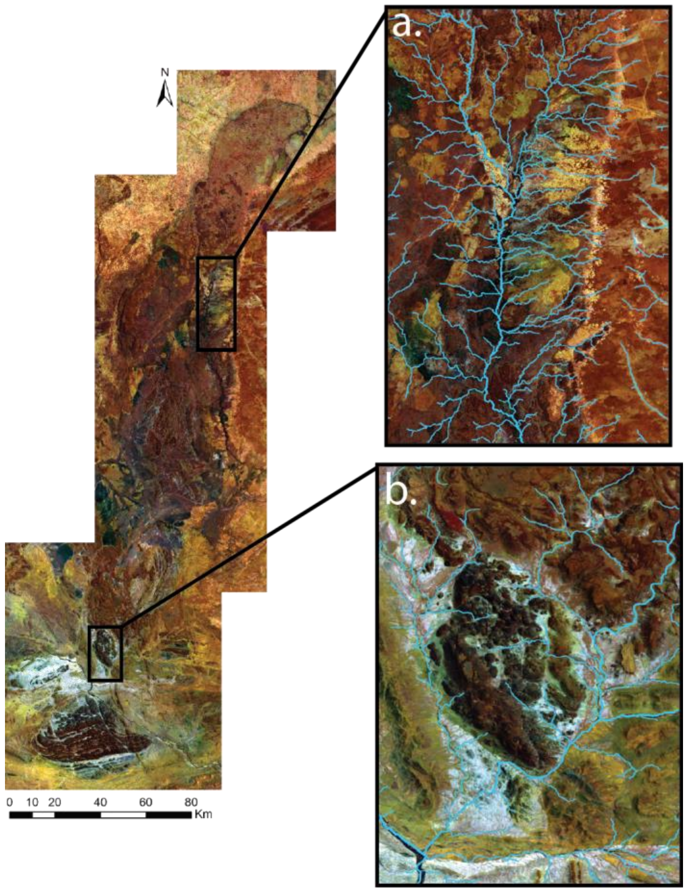

Figure 2.19 - FCC image (641 in RGB) showing: (a) extensive alluvial cover from a river over domain 3 and (b) a well exposed area of outcrop likely owing to the river eroding away into the terrane and prominently exposing parts of domain 6. The river network was produced using hydrology tools in ArcGIS on the STRM data (see method in Section 2.2.3).

2.4.4 Do the Domains of the KAC Represent Individual Plutons?

A pertinent question arises in what do the domains of this study represent? As seen from this study there may be various possibilities influencing the appearance of the domains of the KAC. Factors such as the weathering stability of the rocks in different areas of the KAC, exposure of outcrop owing to regional or local scale tectonics, and erosion and weathering caused by rivers flowing through the KAC are all possible reasons for the formation of the domains as we see them today. It is suggested that the domains identified in the KAC are due to different compositional characteristics of the anorthositic rocks themselves. The remote sensing data show that there are at least two main magmatic entities based on the aforementioned spectral data (north and south of the NE-SW striking granite belt, Figures 1.1 and 2.15). The differences seen between each of the domains could be a result of internal compositional variation in each domain, as well as each domain having a separate concentration and orientation of lineaments. The other influences acting on these domains (summarized above) are therefore likely to enhance the exposure of these domains. It is a possibility that the KAC is composed of multiple plutons as suggested in Ashwal and Twist (1994), where each domain may represent an individual pluton. Futher remote sensing studies and field work may lead to the refinement of the number of plutons. Examples that need to be looked into are: the Chela Supergroup covering parts of domains 5 and 6 (which could possibly be represented as one domain) and the Kalahari cover to the east of the KAC could potentially overlie more plutons. Additional detailed petrographic and structural studies are required to further clarify this point and lead to enahanced understanding of the KACs compositional structure.

2.4.5 Revised Map of the Kunene Anorthosite Complex

The differing spectral responses, compositional domains, and lineament populations all allow for production of a new, detailed geological map of the KAC and surrounding country rocks (Figure 21). The KAC is likely a representation of two main magmatic entities producing a batholithic appearance. Evidence for coalesced domains can be seen between the most northern two domains of the KAC (between domains 1 and 2, Figure 2.5). This intermingling contact and what looks like blebs of domain 1 inside domain 2 are good evidence for a coalesced contact. The blebs and bleb host-rock are both leucotroctolitic, as would be expected from domains 1 and 2, but differ slightly in composition and texture (Figure 2.20). Both rocks within and outside of the blebs are medium to coarse grained leucotroctolites. Outside the bleb (dark blue to teal colours in the band ratio image), the rocks have a greater abundance of clinopyroxene and the olivine grains have a high birefringence. The olivine grains show a peritectic reaction with rims of clinopyroxene surrounding them (Figure 2.20 a). Inside the bleb (light blue to white colours in band ratio image), the rocks have areas of more pegmatitic material and are very brittle/crumbly. The rocks have minor amounts of clinopyroxene and the olivine grains have low birefringence and are commonly altered to iddingsite (Figure 2.20 b). This compositional and textural change could be an indication for evidence towards a coalesced contact. Additional sampling would be required to fully conclude this point. Other contacts may be coalesced, but no evidence is seen in satellite imagery. This could be due to eroding and weathering away of the contacts. The differing spectral responses, compositional domains, and lineament populations observed, combined with interpretation and ground truthing of the data allow presentation of a new geological map of the KAC and parts of its surrounding rocks (Figure 2.21) which will form the basis for the subsequent chapters as well as a succession of more detailed petrological, geochemical and structural research on the intrusion.

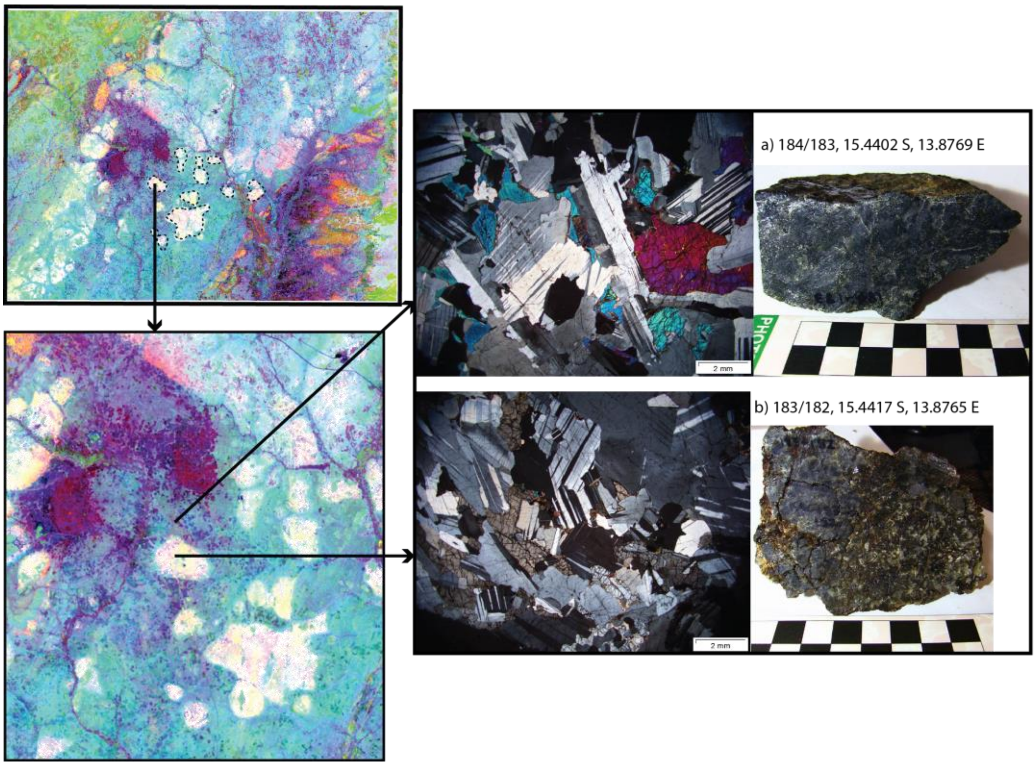

Figure 2.20 - Band ratio image showing location of blebs and their related hand samples, and photomicrographs (cross-nicols). (a) - Outside the bleb (dark blue to teal colours in the band ratio image). (b) - Inside the bleb (light blue to white colours in band ratio image).

Add A2 map here

2.5 Conclusion

This study evaluated the applicability of using remote sensing data processing (Landsat 8 and STRM), image processing, interpretation, field reconnaissance, and petrography for mapping the KAC. This multidisciplinary process is shown to be a valuable technique in such magmatic complexes and it could be applied to other anorthositic complexes exposed in similar arid – semi-arid regions. The variation in Landsat 8 spectral signal correlates well with the different type of rocks observed in the field. The SRTM dataset, combined with an automatic lineament extraction process (which is then manually checked in order to remove non-geological data) has been shown to provide a good estimate of the regional-scale lineament distribution and orientations throughout the KAC. The extracted lineaments appear to match up with field and microscopic observations of magmatic foliations. Combing these datasets, different domains in terms of both composition and lineaments are observed. The KAC is shown to be made up of two main magmatic entities. These entities may be separated into domains that might represent multiple plutons making up the KAC. This study provides additional evidence in favour of batholithic appearance of the anorthositic rock of the KAC, rather than previously suggested models where the KAC was thought to be a layered intrusion. It is recommended that further investigations of the KAC integrate this study with ASTER satellite data (for a greater number of band as well as better spatial and spectral resolution), geophysical data (namely to constrain the eastern extension of the KAC below the Kalahari Supergroup cover), and a field structural mapping survey for a better and more detailed understanding of the KAC.

3 Understanding Magmatic Timescales and Magma Dynamics in Proterozoic Anorthosites: A Geochronological Investigation of the Kunene Anorthosite Complex (Angola)

3.1 Introduction

Proterozoic massif-type anorthosite complexes are some of the most enigmatic and widely debated intrusions in the world. The large volumes of this rock type has made questions regarding anorthosite petrogenesis highly controversial. One emergent question relates to the magmatic timescales of these magmas which form at the Moho (30 – 40 km depth) and intrude into the upper- to mid-crust (10 km depth). Large timescales of emplacement (~80 – 100 Ma) have been noted in Proterozoic anorthosite complexes such as the Mealy Mountains Intrusive Suite, Nain Plutonic Suite, and the Rogaland Anorthosite Province (Table 3.1; Emslie, 1978; Meyer, 2008; Bybee et al., 2014). Long magmatic timescales have important implications for the tectonic settings of Proterozoic anorthosites as it places constraints on the types of settings in which these rocks can form. For instance, long timescales can account for the time required to emplace such large volumes of magma over vast areas.

Table 3.1 - Anorthosite emplacement age and the relating megacrysts isochron Sm/Nd ages (which indicate start of crystallisation of the magmas at high pressure) of three well studied Proterozoic anorthosites (After Bybee et al., 2014)

Anorthositic Complex	Anorthosite Emplacement Age	Megacryst Isochron Sm/Nd Age
Mealy Mountains Intrusive Suite	1640 ± 10 Ma	1765 ± 12 Ma
Nain Plutonic Suite	1326 ± 37 Ma	1444 ± 100 Ma
Rogaland Anorthosite Province	934.5 ± 14.5 Ma	1041 ± 17 Ma

The KAC provides an excellent study site to address the aforementioned problems as it is suggested to be composed of multiple plutons (Ashwal and Twist, 1994) that vary in composition and chemistry (Mayer et al., 2004; Maier et al, 2013). Previous dating of the

KAC suggests that long magmatic time scales greater than 150 Ma may be preserved in the plutons of the KAC, but large age errors preclude any firm conclusions being drawn in this regard (see Section 3.2). Thus, the KAC represents an excellent example in which to test whether the duration and timing of magmatism in Proterozoic anorthosites is indeed on the order of 100 Ma (Ashwal and Twist, 1993; Mayer et al., 2004). Previous age dating was mostly conducted on related or possibly coeval rocks to the KAC, with little to no age data coming from the anorthositic rocks themselves. New, high precision U-Pb dating in this study attempts to resolve age differences between the different domains delineated in the previous chapter, and elucidate whether Proterozoic anorthosites do form over hundred million year periods.

3.2 Age Review of the Kunene Anorthosite Complex

Past studies of the KAC and its basement rocks show a wide spread of age data (1.3 – 2.2 Ga; see Appendix A for table of all published ages). A recent study in the Angolan portion of the KAC (Mayer et al., 2004) reports Sm – Nd ages ranging from 1470 ± 25 Ma to 1319 ± 28 Ma. The large spread of observed ages may result from no systematic study of the age variation within the KAC as well as due to the use of lesser advanced dating techniques (e.g. Rb-Sr of De Carvalho et al., 1987) which resulted in errors that in some cases encompass the entire timescale of the KACs possible emplacement. This age range could also represent the actual magmatic timescale for the emplacement of the KAC. The ages of the KAC summarized in Table 3.2 and Figure 3.1 show that published dates derive mostly from related/coeval rocks of the KAC, or have large errors when they are derived from anorthositic rocks. In the Angolan part of the complex, U-Pb analyses of zircons from a cogenetic mangerite vein produce an age of 1371 ± 2.5 Ma, which has been used as one of the main reference ages of the KAC (Mayer et al., 2004). In the Namibian portion of the KAC, the Zebra Mountain lobe returns a U-Pb age of 1385 ± 25 Ma on zircons from a leucogabbronorite (Drüppel et al., 2007). Maier et al. (2013) suggested that the age range observed throughout the KAC may be a representation of the initiation and termination of anorthosite magmatism, and that the plutons that make up the KAC could possibly have resolvable age differences. In order to assess the possible age range throughout the KAC, as well as whether any age patterns exist between plutons, a systematic series of high precision U-Pb TIMS analyses on zircon and baddeleyite (from the various domains identified in the remote sensing analysis presented in Chapter 2) has been conducted.

Table 3.2 - A compilation of age for the Kunene Anorthosite Complex from current literature. For a full table with all basement and post Kunene Complex ages, see Appendix A. *Unpublished data; + Datum: WSG 1984.

Latitude+	Longitude+	Rock Type	Method	Mineral / Whole rock(WR) analysed	Age (Ma)	Locality precision	Reference
13.9363 E	15.1913 S	Anorthosite dyke	Sm–Nd	WR, Pl phenocrysts, Pl groundmass	1319 ± 28	< 50 m	Mayer et al., 2004
14.9961 E	14.6530 S	Red granite	Rb–Sr	WR	1350 ± 65	< 50 m	De Carlvalho et al.,1987
13.6610 E	17.4374 S	Leucotroctolite	U–Pb	Baddeleyite	1363 ± 17	<1 Km	Maier et al., 2013
14.0272 E	15.4227 S	Mangerite dyke	U–Pb	Zircon	1371.3 ± 2.5	< 50 m	Mayer et al., 2004
13.7845 E	17.3761 S	Syenodiorite	U–Pb	Zircon	1376 ± 2	<1 Km	Drüppel et al., 2007
13.7662 E	17.1324 S	Leucogabbronorite	U–Pb	Zircon	1385 ± 25	<1 Km	Drüppel et al., 2000
14.0227 E	15.4198 S	Mangerite dyke	U–Pb	Zircon	1385 ± 7.6	< 50 m	McCourt et al., 2013
13.9522 E	16.6703 S	Mangerite dyke	U–Pb	Zircon	1403 ± 7.1*	< 50 m	Baxe et al., 2007
13.9363 E	15.1913 S	Anorthosite dyke	Rb–Sr	Zircon	1406 ± 97	< 50 m	Mayer et al., 2004
13.4667 E	16.1833 S	Red granite	Rb–Sr	WR	1407 ± 26	< 50 m	De Carlvalho et al.,1987
13.9333 E	16.4833 S	Red granite	Rb–Sr	WR	1411 ± 24	< 50 m	De Carlvalho et al.,1987
13.9121 E	16.9924 S	Olivine gabbro	U–Pb	Zircon	1434 ± 2*	< 50 m	Baxe et al., 2007
14.0965 E	15.0663 S	Anorthosite	Rb–Sr	WR, Pl and Orthopyroxene	1464 ± 140	< 50 m	Mayer et al., 2004
14.0965 E	15.0663 S	Anorthosite	Sm–Nd	WR, Pl, Orthopyroxene and Biotite	1470 ± 25	< 50 m	Mayer et al., 2004

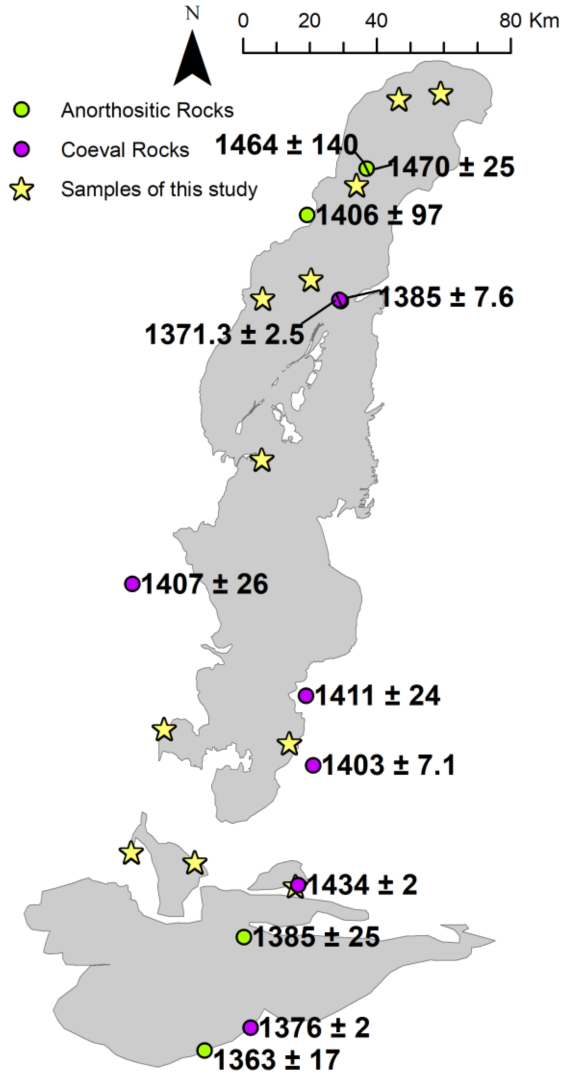

Figure 3.1 - Map of the Kunene Anorthosite Complex (in grey) showing the distribution and ages (Ma) of previous studies summarized in Table 3.2 (circles) and samples of this study (stars). Split circle with diagonal line represents two samples dated at same locality with different methods.

3.3 Sampling and Analytical Procedure

Sampling for geochronological studies of the KAC was based on the remote sensing study (Chapter 2) which identified various possible domains that make up the KAC. At least one sample per domain was collected during field expeditions to the KAC in 2015 and 2016. Sample mass averaged between 5 – 8 kg to facilitate sufficient extraction of datable material (zircon and/or baddeleyite). Three of the 14 selected samples had neither zircon nor baddeleyite, but the remaining eleven samples covered a representative portion of the KAC (Figure 3.1). The samples were processed at the University of Oslo (Norway) using extraction procedures adapted from Krogh (1973), Krogh (1982), and Corfu (2004). The samples were cleaned, crushed in a jaw crusher and pulverized in a hammer mill, followed by mineral separation using a combination of a Wilfley table, a 250 µm sieve, free-fall magnetic separation, and heavy liquid density separation. Recovered zircon and baddeleyite grains were then handpicked under a microscope. The selected zircon grains were subsequently annealed (~ 60 hours in an oven at 900 °C) and later chemically abraded (in HF acid for 12 hours in an oven at 185 °C) to remove any damaged external regions. The selected baddeleyite was air abraded with pyrite for ~3 hours and cleaned with HNO_3 (to remove any pyrite). Both zircon and baddeleyite were then washed on a hot plate in 4N NHO_3 for 20 minutes and rinsed repeatedly using H_2O and acetone in an ultra-sonic bath. The grains were then weighed on a microbalance, loaded into individual Teflon bombs and spiked with a ^{202}Pb - ^{205}Pb - ^{235}U tracer (the tracer is correlated with the Earth Time 100 tracer). The Teflon bombs were loaded into an oven for ~120 hours at ~185 °C. All baddeleyite grains and large zircon grains (> 5 µg) underwent chemical separation (as in Krogh, 1973) in order for elution of the U and Pb to take place. The sample was then loaded onto Re filaments with Si-gel and H_3PO_4. The isotopic ratios of the sample grains were measured using an ID-TIMS (isotope dilution - thermal ionization mass spectrometer) method, on the MAT 262 mass spectrometer. The isotope ratios were measured either Faraday cups in static mode, or by peak-jumping in an ion-counting secondary electron multiplier (SEM) mode (for smaller, weak signal samples and all ^{207}Pb/^{204}Pb ratios). Correction standards for measuring of samples were based on concurrent measurements of the NBS982 Pb and U500 standard. All data were corrected for 0.1% per atomic mass unit (a.m.u) fractionation using reproducibility factors of ±0.05% per a.m.u. for Faraday data and ±0.1% per a.m.u. for secondary electron multiplier data (Corfu, 2004). The zircon and baddeleyite analyses were corrected for a Pb blank of 2 pg and 0.1 pg U, but in some cases the actual blank was higher and allowance has been made for that during the recalculation of the data. The residual initial common Pb was subtracted using compositions calculated with the Stacey & Kramers (1975) model for the age of the sample (at 1400 Ma) and decay constants are those of Jaffey et al. (1971). The data were reduced with ROMAGE 9D (written and later modified by: T. E. Krogh & L. Heaman respectively). Data plotting and age calculations were performed with Isoplot (Ludwig, 1999).

3.4 ID-TIMS Results

Anorthosite, being predominantly an adcumulate of plagioclase, generally has a small proportion of interstitial material and incompatible elements such as zirconium. This makes the occurrence of minerals such as zircon and baddeleyite uncommon. Zircon and baddeleyite of the KAC exhibit an anhedral, segmented morphology. This morphology is related to crystallisation in remaining pore spaces between cumulus phases (Scoates and Chamberlain, 1995; Van Breemen et al, 1986). The crystals are free of any cores or secondary alteration and can generally be interpreted as fresh primary zircon and baddeleyite. The data table of U-Pb isotopic compositions of all single grain fractions (Table 3.3) and their resulting Concordia plots (Figure 3.2) were determined for the 11 samples (10 anorthositic and 1 country rock) of the KAC.

KAC 113/103 (14.86366 S, 14.29551 E):

Sample KAC 113/103 (Figure 3.2 a) is a leucotroctolitic rock composed of plagioclase (85 %) and olivine (10 %) with orthopyroxene, clinopyroxene, biotite, and opaque minerals as minor phases (5 %). The Concordia plot was calculated from four grain fractions (three baddeleyite and one zircon). The zircon fractions' reverse discordance on the plot is likely a result of analytical error having a large amount of common Pb (4 pg). The remaining baddeleyite grains are concordant and overlap within error. The resultant Concordia age is 1381.8 ± 1.8 Ma and can be interpreted as the crystallisation age of the sample.

KAC 108/99 (14.87895 S, 14.18267 E):

Sample KAC 108/99 (Figure 3.2b) is a leucotroctolitic rock composed of plagioclase (85 %) and olivine (12 %) with orthopyroxene, clinopyroxene, biotite, and opaque minerals as minor phases (3 %). The Concordia plot was calculated from three baddeleyite grain fractions. Two of the baddeleyite are concordant and within error, with normal discordance of the youngest baddeleyite fraction owing to Pb loss of the grain. The regression of the Concordia plot gives an age of 1381.0 ± 3.3 Ma and is interpreted as the crystallisation age of the sample.

Table 3.3 - ID-TIMS U-Pb Results for Zircon and Baddeleyite Fraction of the Kunene Anorthosite Complex.

Fraction Analysed	Properties*	Weight [ug]	Pb[t] [ppm]	U [ppm]	Th/U	Pb[c] [ppm]	Pbcom** [pg]	$^{206}Pb/^{204}Pb$ #	$^{207}Pb/^{235}U$ #	2σ [abs]	$^{206}Pb/^{238}U$ #	2σ [abs]	rho	$^{207}Pb/^{206}Pb$ #	2σ [abs]	$^{206}Pb/^{238}U$ ##	2σ [abs]	$^{207}Pb/^{235}U$ ##	2σ [abs]	$^{207}Pb/^{206}Pb$ ##	2σ [abs]	Disc. [%]
113/103																						
113/103 449/56	ZR CA 1GR	11	38	115	1.00	3.54	45.9	434	3.00848	0.01668	0.24640	0.00073	0.61	0.08855	0.00039	1419.9	3.8	1409.8	4.3	1394.5	8.4	-2.0
113/103 449/54	BDY AA 1GR	8	48	217	0.01	0.00	3.1	8237	2.88122	0.00784	0.23763	0.00054	0.92	0.08794	0.00009	1374.4	2.8	1377.0	2.0	1381.1	2.1	0.5
113/103 459/59	BDY AA 1GR	1	16	71	-0.01	0.00	1.0	1082	2.87139	0.02438	0.23734	0.00088	0.47	0.08775	0.00066	1372.8	4.6	1374.4	6.4	1376.9	14.3	0.3
113/103 459/60	BDY AA 1GR	1	45	197	0.08	0.00	0.8	3824	2.89536	0.01271	0.23839	0.00086	0.89	0.08809	0.00018	1378.3	4.5	1380.7	3.3	1384.4	3.8	0.5
108/99																						
108/99 455/50	BDY AA 1GR	1	5	24	0.03	0.00	1.0	384	2.88848	0.03137	0.23834	0.00163	0.65	0.08790	0.00073	1378.0	8.5	1378.9	8.2	1380.2	15.8	0.2
108/99 455/51	BDY AA 1GR	1	4	20	0.04	0.00	1.9	162	2.81664	0.05128	0.23050	0.00136	0.41	0.08863	0.00148	1337.1	7.1	1360.0	14	1396.1	31.6	4.7
108/99 455/52	BDY AA 1GR	6	24	106	0.01	0.00	1.3	6896	2.88098	0.01066	0.23765	0.00073	0.87	0.08792	0.00016	1374.4	3.8	1376.9	2.8	1380.8	3.4	0.5
123/112																						
123/112 454/60	BDY AA 1GR	1	66	291	0.02	0.00	1.6	2722	3.00156	0.01263	0.24110	0.00086	0.92	0.09029	0.00015	1392.4	4.4	1408.0	3.2	1431.7	3.1	3.0
123/112 454/62	BDY AA 1GR	1	23	103	0.01	0.00	1.2	1259	2.90114	0.01436	0.23762	0.00090	0.85	0.08855	0.00024	1374.3	4.7	1382.2	3.7	1394.4	5.1	1.6
123/112 454/61	BDY AA 1GR	1	25	115	0.03	0.00	3.1	544	2.86245	0.01740	0.23461	0.00085	0.68	0.08849	0.00040	1358.6	4.4	1372.1	4.6	1393.1	8.5	2.7
123/112 459/54	BDY AA 1GR	1	106	473	0.01	0.00	1.9	3635	2.88495	0.00779	0.23823	0.00054	0.92	0.08783	0.00010	1377.5	2.8	1378.0	2.0	1378.7	2.1	0.1
123/112 459/55	BDY AA 1GR	1	203	910	0.00	0.00	1.3	10137	2.88500	0.01526	0.23867	0.00113	0.94	0.08767	0.00016	1379.8	5.9	1378.0	4.0	1375.2	3.5	-0.4
90/83																						
90/83 449/58	BDY AA	11	37	167	0.02	0.00	1.5	18246	2.87927	0.00774	0.23735	0.00055	0.95	0.08798	0.00008	1372.9	2.9	1376.5	2.0	1382.1	1.7	0.7
90/83 455/26	BDY AA 1GR	11	43	192	0.01	0.00	3.0	10280	2.86986	0.01013	0.23676	0.00066	0.90	0.08791	0.00014	1369.8	3.4	1374.0	2.7	1380.6	3.1	0.9
90/83 455/25	BDY AA 1GR	11	43	189	0.01	0.56	12.1	2515	2.86586	0.01078	0.23712	0.00072	0.91	0.08766	0.00014	1371.7	3.7	1373.0	2.8	1375.0	3.1	0.3
90/83 449/57	ZR CA 1GR	1	41	146	0.88	0.00	0.9	2450	2.86487	0.01394	0.23736	0.00094	0.88	0.08754	0.00020	1373.0	4.9	1372.7	3.7	1372.3	4.4	-0.1
152/146A																						
152-146A 466/53	BDY EU TIP NA 1GR	1	148	666	0.02	0.00	3.4	2862	2.87445	0.01130	0.23717	0.00072	0.88	0.08790	0.00017	1372.0	3.8	1375.2	3.0	1380.3	3.7	0.7
152/146A 459/53	BDY AA 1GR	1	554	2482	0.01	0.00	2.1	17441	2.88058	0.01111	0.23806	0.00081	0.96	0.08776	0.00010	1376.6	4.2	1376.8	2.9	1377.2	2.2	0.1
152-146A 466/52	BDY EU TIP NA AGR	1	50	229	0.01	0.00	1.0	3188	2.84103	0.00968	0.23503	0.00060	0.89	0.08767	0.00014	1360.8	3.1	1366.4	2.6	1375.3	3.1	1.2
152/146A 459/52	BDY AA 1GR	1	363	1633	0.01	0.00	3.0	7841	2.86482	0.01180	0.23722	0.00073	0.83	0.08759	0.00020	1372.2	3.8	1372.7	3.1	1373.5	4.4	0.1
152/146A 459/51	BDY AA 1GR	1	108	485	0.02	0.00	1.9	3632	2.85084	0.01170	0.23630	0.00083	0.93	0.08750	0.00013	1367.4	4.3	1369.0	3.1	1371.5	2.9	0.3
144/139																						
144/139 454/54	BDY AA 1GR	1	324	1446	0.00	0.00	1.2	18293	2.92973	0.00954	0.23943	0.00067	0.94	0.08875	0.00010	1383.7	3.5	1389.6	2.5	1398.7	2.1	1.2
144/139 454/55	BDY AA 1GR	1	163	723	0.01	0.00	1.4	7755	2.94107	0.00845	0.23997	0.00059	0.93	0.08889	0.00009	1386.6	3.1	1392.5	2.2	1401.7	2.0	1.2
144/139 454/56	BDY AA 1GR	1	177	781	0.00	0.00	2.4	4814	2.96151	0.00938	0.24172	0.00061	0.89	0.08886	0.00013	1395.6	3.2	1397.8	2.4	1401.1	2.8	0.4
41/42A																						
41/42A 449/60	ZR CA 1GR	1	139	439	0.53	0.00	0.5	15371	4.15180	0.02453	0.29118	0.00158	0.95	0.10341	0.00019	1647.4	7.9	1664.6	4.8	1686.2	3.4	2.6
41/42A 455/27	ZR CA 1GR	2	12	36	1.43	0.00	3.0	379	3.00538	0.02658	0.24326	0.00120	0.63	0.08960	0.00062	1403.6	6.2	1409.0	6.7	1417.1	13.2	1.1
41/42A 449/62	ZR CA 1GR	14	7	21	1.33	0.00	2.3	1908	2.98508	0.01431	0.24188	0.00103	0.91	0.08951	0.00018	1396.4	5.4	1403.8	3.6	1415.1	3.7	1.5
41/42A 449/61	ZR CA 1GR	5	16	48	1.85	0.00	1.7	2133	2.91855	0.01313	0.23963	0.00090	0.91	0.08833	0.00017	1384.8	4.7	1386.7	3.4	1389.7	3.7	0.4
41/42A 455/28	ZR CA 1GR	14	6	21	1.24	0.00	2.3	1878	2.94978	0.01370	0.24230	0.00087	0.85	0.08830	0.00022	1398.6	4.5	1394.8	3.5	1388.9	4.7	-0.8
57/55																						
57/55 449/59	ZR CA 1GR	25	18	63	0.97	0.00	1.1	22008	2.93216	0.00796	0.24062	0.00056	0.93	0.08838	0.00009	1389.9	2.9	1390.3	2.1	1390.8	2.0	0.1
57/55 474/12	ZR FR CA 1GR	22	17	65	0.64	0.00	0.8	27754	2.93145	0.00868	0.24062	0.00061	0.93	0.08836	0.00010	1389.9	3.2	1390.1	2.2	1390.3	2.1	0.0
57/55 455/49	BDY AA 1GR	2	123	549	0.00	0.00	1.5	10707	2.92572	0.00982	0.23976	0.00070	0.94	0.08850	0.00011	1385.5	3.6	1388.6	2.5	1393.4	2.3	0.6
57-55 449/52	BDY AA 1GR	4	58	260	0.00	0.00	3.5	4380	2.92150	0.00773	0.23973	0.00051	0.89	0.08839	0.00011	1385.3	2.6	1387.5	2.0	1390.9	2.3	0.5
57/55 466/54	BDY AA 1GR	1	134	596	0.00	0.00	2.8	3122	2.92082	0.00991	0.24027	0.00065	0.88	0.08817	0.00015	1388.1	3.4	1387.3	2.6	1386.1	3.2	-0.2
17/22																						
17/22 454/59	BDY AA 1GR	1	64	284	0.02	0.00	2.3	1817	2.90534	0.01301	0.23855	0.00084	0.87	0.08833	0.00020	1379.2	4.4	1383.3	3.4	1389.7	4.2	0.8
17/22 454/57	BDY AA 1GR	1	194	871	0.01	0.00	5.7	2234	2.88779	0.01121	0.23692	0.00069	0.85	0.08840	0.00018	1370.7	3.6	1378.7	2.9	1391.2	3.9	1.6
17/22 454/58	BDY AA 1GR	1	37	165	0.02	0.00	5.7	434	2.88964	0.02584	0.23493	0.00090	0.54	0.08921	0.00068	1360.3	4.7	1379.2	6.7	1408.6	14.5	3.8
12/14																						
12/14 459/61	BDY AA 1GR	9	76	325	0.01	0.00	1.9	23615	3.11275	0.00956	0.24905	0.00066	0.94	0.09065	0.00009	1433.6	3.4	1435.8	2.4	1439.2	2.0	0.4
12/14 459/62	BDY AA 1GR	14	50	214	0.01	0.00	1.7	27240	3.12306	0.00864	0.24986	0.00058	0.94	0.09065	0.00009	1437.7	3.0	1438.4	2.1	1439.3	1.9	0.1
12/14 454/53	BDY AA 1GR	10	124	529	0.01	0.00	2.1	37810	3.12379	0.01027	0.25026	0.00072	0.96	0.09053	0.00009	1439.8	3.7	1438.6	2.5	1436.8	1.8	-0.2
27/31																						
27/31 459/56	ZR CA 1GR	12	56	156	0.63	0.00	3.3	11219	4.85469	0.01297	0.32033	0.00076	0.96	0.10991	0.00009	1791.4	3.7	1794.4	2.2	1798.0	1.4	0.4
27/31 459/57	ZR CA 1GR	1	201	553	0.72	0.00	4.0	2733	4.83190	0.01732	0.31922	0.00095	0.91	0.10978	0.00016	1785.9	4.6	1790.5	3.0	1795.8	2.7	0.6

* ZR = Mineral analysed: Zircon   CA = Chemical Abrasion   ** Total common Pb, Including: Blank, Sample and Spike

BDY = Mineral analysed: Baddeleyite   AA = Air Abrasion   # Ratio ; ## Age

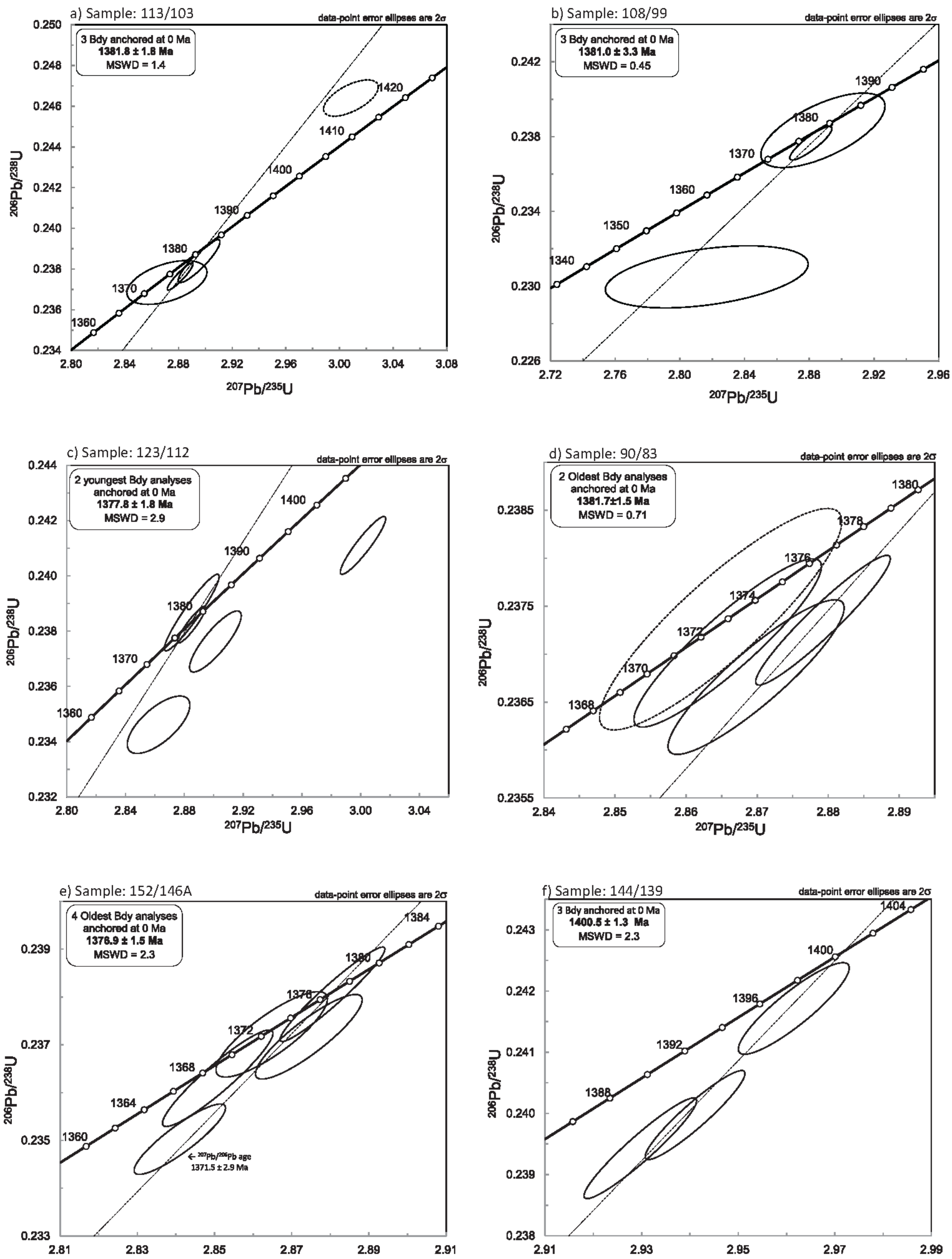

Figure 3.2 - Concordia plots for all U-Pb data of analysed baddeleyite and zircon fractions. Each ellipse represents the result of a single fraction analysis. Solid line ellipses: baddeleyite, and dashed line ellipses: zircon.

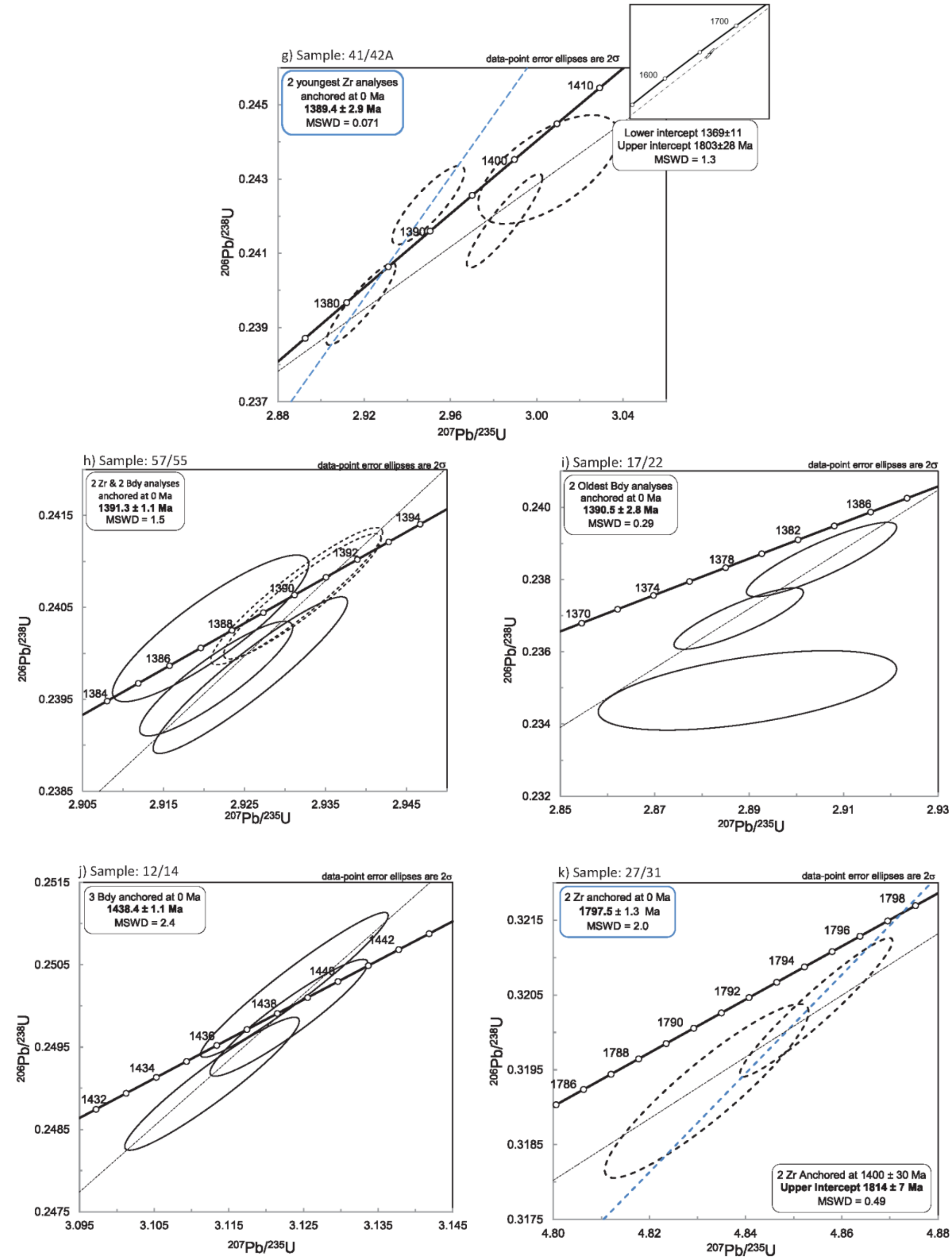

Figure 3.2 (cont.) - Concordia plots for all U-Pb data of analysed baddeleyite and zircon fractions. Each ellipse represents the result of a single fraction analysis. Solid line ellipses: baddeleyite, and dashed line ellipses: zircon.

<u>KAC 123/112 (15.11102 S, 14.06949 E):</u>

Sample KAC 123/112 (Figure 3.2c) is a leucotroctolitic rock composed of plagioclase (75 %) and olivine (20 %) with clinopyroxene, muscovite, biotite, apatite, and opaque minerals minor phases (5 %). The Concordia plot indicates the possibility of two generations of baddeleyite occurrence. The older generation of baddeleyite would indicated the minimum age of this component. Another possibility would be inheritance of zircon cores which have desilicified and are now baddeleyite. Further studies are needed in order to completely resolve this sample's possible baddeleyite inheritance. The Concordia age (1377.8 ± 1.8 Ma) of the two youngest baddeleyite grains give the best estimate of final emplacement ages of the sample.

<u>KAC 90/83 (15.36449 S, 13.94658 E):</u>

Sample KAC 90/83 (Figure 3.2d) is an anorthosite composed of plagioclase (90 %), olivine (5 %), and clinopyroxene (3 %), as well as biotite and opaque minerals as minor phases (2 %). The Concordia plot was calculated from three baddeleyite fractions and one zircon fraction. The reversely discordant baddeleyite and zircon grains are most likely a result of analytical error where the samples had low $^{207}Pb/^{204}Pb$ measurements (~2500 as compared to 10 000/18 000). The two normally discordant baddeleyite grains indicate Pb loss in the sample and produce a Concordia age for crystallisation of 1381.7 ± 1.5 Ma.

<u>KAC 152/146A (15.41555 S, 13.81692 E):</u>

Sample KAC 152/146A (Figure 3.2e) is a leucogabbro composed of plagioclase (85 %) and clinopyroxene (14 %) with biotite and opaque minerals as minor phases (1 %). The Concordia plot shows a larger spread of baddeleyite analyses with some analyses exhibiting a reverse discordance as a result of low $^{207}Pb/^{204}Pb$ (as explained in sample KAC 90/83) or some late stage alteration/mineral growth. The remaining baddeleyite samples are normally discordant owing to Pb loss and produce a Concordia age of 1369.9 ± 1.5 Ma which is interpreted as the crystallisation age of the sample.

KAC 144/139 (15.84750 S, 13.81432 E):

Sample KAC 144/139 (Figure 3.2f) is a leucotroctolitic rock composed of plagioclase (85%), olivine (10%), and clinopyroxene (5%). The Concordia plot is calculated from three baddeleyite fractions and produces a normal Pb loss discordance pattern. The resultant Concordia age is 1400.5 ± 1.3 Ma and is interpreted as the crystallisation age of the sample.

KAC 41/42A (16.57356 S, 13.55232 E):

Sample KAC 41/42A (Figure 3.2g) is an olivine-leucogabbro composed of plagioclase (60 %), olivine (20 %), clinopyroxene (15 %), and orthopyroxene (5 %). The Concordia plot was calculated from five zircon fractions. The sample shows that there is an inherited component that results in an upper intercept age of 1803 ± 28 Ma and a lower intercept age of 1369 ± 11 Ma. To estimate the minimum emplacement age of the sample, the two youngest zircon analyses were used and produced an age of 1389.4 ± 2.9 Ma. The remaining zircons fractions aligned on a discordia are defined by the youngest (Kunene) and oldest (inherited) zircon analyses.

KAC 57/55 (16.61172 S, 13.88787 E):

Sample KAC 57/55 (Figure 3.2h) is a leucogabbronorite composed of plagioclase (60 %), clinopyroxene (20 %), orthopyroxene (18 %), as well as biotite and opaque minerals as minor phases (2 %). The Concordia plot was calculated from four grain fractions (three baddeleyite and two zircon). The error ellipsoids overlap well within error with minor normal (caused by normal Pb loss) and reverse discordance seen in the baddeleyite (where the reverse discordance is likely an analytical error or a low signal run of the baddeleyite fraction). The zircon indicated a possibility of an age difference with the baddeleyite, but the difference is small and likely negligible. Regression produces an age of 1391.3 ± 1.1 Ma and is interpreted as the crystallisation age of the sample.

KAC 17/22 (16.93143 S, 13.63432 E):

Sample KAC 17/22 (Figure 3.2i) is an olivine-bearing leucogabbro composed of plagioclase (70 %), clinopyroxene (10 %), olivine (5 %), orthopyroxene (4 %), and minor amounts of biotite (1 %). The Concordia plot was obtained from three baddeleyite fractions and produces a normal Pb loss discordance pattern. The largely discordant point is likely a result of the small baddeleyite grain size or a low signal run giving a small $^{207}Pb/^{204}Pb$ ratio. The resultant Concordia age is 1390.5 ± 2.8 Ma and is interpreted as the crystallisation age of the sample.

KAC 12/14 (16.99129 S, 13.91436 E):

Sample KAC 12/14 (Figure 3.2j) is a leucotroctolite composed of plagioclase (80 %) and olivine (15 %) and orthopyroxene, clinopyroxene, phlogopite, and opaque minerals as minor phases (5 %). The Concordia plot was obtained from three baddeleyite fractions and produces a normal Pb loss discordance pattern with fractions overlapping mostly within error. Regression of the Concordia plot results in a crystallisation age of 1438.4 ± 1.1 Ma for this sample.

KAC 27/31 (16.90432 S, 13.46386 E):

Sample KAC 27/31 (Figure 3.2k) is a gneissic meta-granodiorite from the surrounding country rocks, west of the KAC. The Concordia plot was obtained from two zircon fractions and produces a normal Pb loss discordance pattern with fractions overlapping well within error. The regression age of the Concordia plot resulted in an age of 1797.5 ± 1.3 Ma and is a first order interpretation of the possible crystallisation age of the sample. Regression was anchored at a Kunene-aged event and yields an upper intercept age of 1814 ± 7 Ma. These ages agree with the 1803 ± 28 Ma inherited age of sample KAC 41/42A.

3.5 Discussion

3.5.1 A Genetic Link between Anorthosite Age and Composition

The data show that the KAC geochronology is characterized by distinct age groupings. An important consideration is whether there is any relationship between these age groups and the mineral assemblages or the composition of the anorthosite bodies. Combining the remote sensing study and petrographic validation (Appendix B) of the samples in the KAC with this new age data reveal that a clear trend is visible. In the KAC, as shown in Figure 3.3, the older domains (~1400 Ma and 1390 Ma) coincide with orthopyroxene-rich compositions and in general occur south of the Red Granite belt, whereas the younger domains (~1380 Ma) coincide with the olivine-rich domains (orthopyroxene occurrence is rare/poor). Exceptions to these general age groups are the oldest and smallest leucotroctolitic domains of the KAC with an age of 1438.4 ± 1.1 Ma, and a more heterogeneous domain (in the south of the KAC) mainly made of anorthosite *sensu stricto* and leucotroctolite, with a subordinate amount of orthopyroxene in the assemblage.

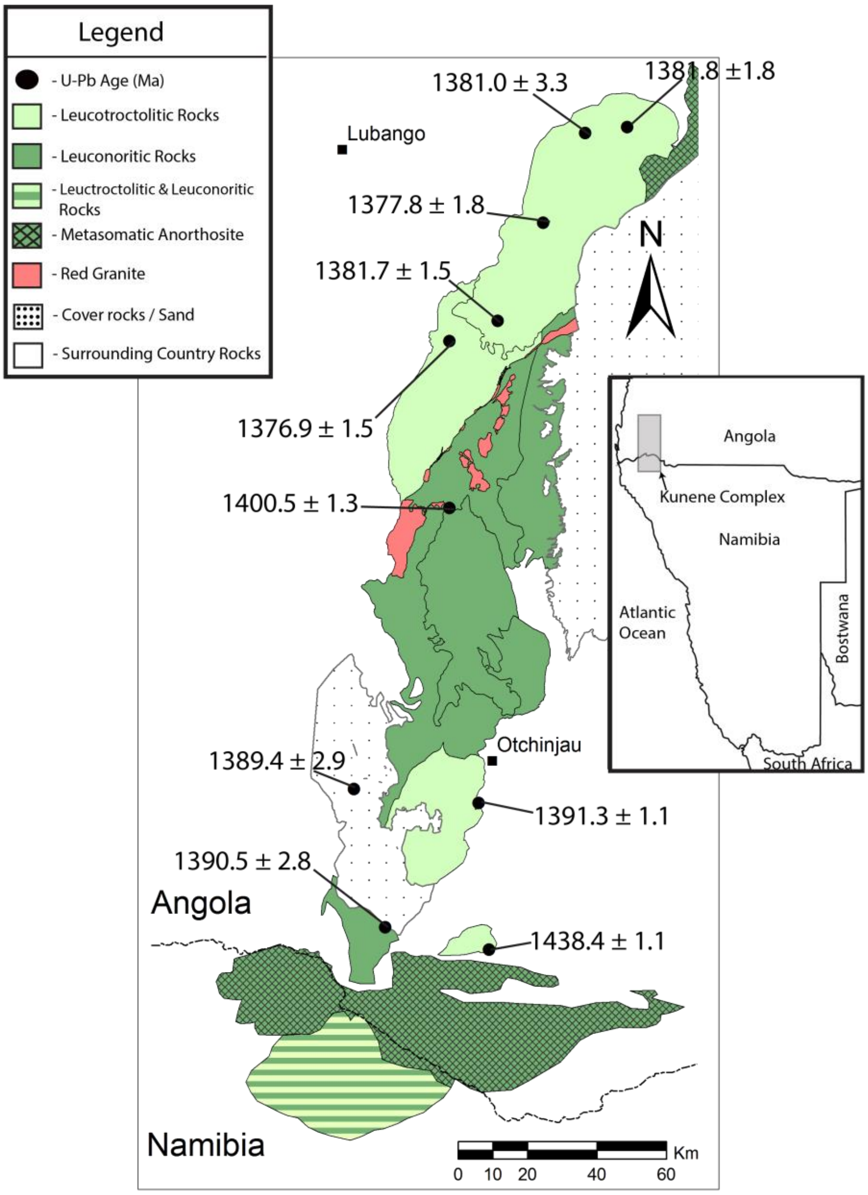

Figure 3.3 - Map of the Kunene Anorthosite Complex showing new U-Pb ages of anorthositic rocks of the KAC and their relating rock-type. Domains of this image are based upon domains of Chapter 2.

This relationship between crystallization ages and compositions can be explained by a model where older pulses of magma have intruded and which previously experienced a greater degree of contamination forcing the broadly basaltic parental magma to produce orthopyroxene (instead of olivine) as the main mafic phase (Emslie et al., 1987; Drüppel, 2007; Myer et al., 2008; Gleißner, 2011). In this model, the later pulses of magma would receive a lower degree of contamination as they would be ascending through already partially melted crust, producing olivine as the main mafic phase. The exception to this model is the oldest and smallest domain of the KAC. A possible reason for this is that this is the first small pulse of magma of the Kunene event received very small degrees of contamination owing to its size. This could be related to insufficient thermal energy, due to its small size, to induce significant contamination. A more detailed study is required to determine the cause of this outlier. The heterogeneous southern domain may be a result of an intermediate degree of contamination having developed a magma composition which produces both olivine and orthopyroxene phases. Overall, this model corroborates previous studies in the KAC where intrusive relationships between older leuconoritic bodies and younger, crosscutting, leucotroctolites are described (Köstlin, 1974; De Carvalho and Alves, 1990; Drüppel, 2007; Gleißner, 2011).

These results have important implications for Proterozoic anorthosites from a global perspective. Many studies in the past have suggested a link between anorthosite composition and crystallisation ages, and in general there is a growing consensus that this link between older leuconoritic rock and younger leucotroctolitic rock exists (Emslie et al., 1987; Myer et al., 2008; Frost et al., 2010; Heinonen et al., 2010). Whereas studies on Proterozoic anorthosites such as in the Nain plutonic suite, Laramie Anorthosite Complex, and the Ahvenisto Complex based these interpretations mainly on field relationships and isotope studies, there has been no systematic and precise age data of the anorthositic rocks to compliment these remarks. This study allows for a true comparison of the observed age and composition of a Proterozoic anorthosite and sets the stage for isotopic and contamination studies to be performed.

3.5.2 Emplacement Dynamics and Timescales

The age data presented in Section 3.4 show that the various components of the KAC were emplaced episodically. Indeed, there is no gradual age progression throughout the complex, but distinct groupings of ages (Figure 3.3). Mean age clusters of 1379.8 ± 2.0 Ma (n=5) occur north of the NE – SW–striking Red Granite belt, whereas in the south there is an older mean age grouping of 1390.4 ± 2.3 (n=3). Owing to poor yield in datable material in samples only one age of 1400.5 ± 1.3 is available in the center of the KAC. An age of 1438.4 ± 1.1 Ma is found in a small, leucotroctolitic body to the south east of the KAC (Figure 2.7b). These age data indicate that there is a minimum magmatic emplacement timescale of ~60 Ma. However, this timescale could be larger as there is evidence of high aluminium orthopyroxene megacrysts (HAOMs) occurring throughout the KAC. Bybee et al. (2014) showed that these HAOMs are indicators that anorthositic systems have longer magmatic lifespans of ~80 – 100 Ma. The age groupings of anorthositic intrusions in the KAC represent separate pulses of magmatic emplacement, separated by several million-year periods of quiescence. Evidence of comagmatic HAOMs seen in the KAC is also an indication of a polybaric crystallisation system for the anorthosites. HAOMs typically crystallise between depths of 30 – 40 km (Emslie, 1978; Charlier et al., 2010; Bybee et al., 2014), while final emplacement of the anorthosite is at shallow depths of less than 10 km (Valley and O'Neil, 1982). Therefore it is likely that the KAC emplacement could be a result of the accumulation of anorthositic magma at the base of the Moho, where the magma would only intrude in pulses once a sufficient buoyant volume had been reached. During this process of accumulation HAOMs are also incorporated in the melt and ascend and intrude as part of the crystal mush.

The oldest age from this study is 1438 Ma. It indicates early crystallization, at least 40 Ma before the majority of the emplacement of the KAC. The age is supported by an age of about 1434 Ma from the same leucotroctolitic body in an unpublished M.Sc. dissertation by Baxe (2007). It is therefore unlikely to be the result of inheritance, contamination or analytical error of another rock, but rather confirmation of initial magmatic activity 40 Ma before the subsequent magmatic bodies' emplacement. Other small satellite anorthositic bodies found during a field excursion in 2016, and observed by Maier et al. (2013), occur in the surrounding country rock of the KAC and could be evidence of similar early differentiated bodies throughout the KAC. In the following 20 Ma of pulsed magmatism the remaining domains would follow the expected trend, with magma having sufficient time to accumulate a large mass of plagioclase and emplace once sufficient differentiation has taken place. The 40 Ma age difference between the recorded emplacement age of the first magmatic body and the remaining magmatic emplacement suggests two possibilities. The first possibility is that magma differentiation occurred slowly over an extended period of time with anorthositic mushes reaching their final emplacement depth at a faster rate.

The second possibility is that differentiation occurred at a faster rate but the mushes ascended slowly in a near solid state to their final emplacement depths.

3.6 Conclusion

The results of the geochronological study indicate that: 1) the Kunene Complex anorthosites were emplaced over a 60 Ma period (at minimum) 2) There is a 40 Ma period of no recorded ages in the KAC (as ages represent only the final emplacement age of the rocks), this could be the result of a difference in magma differentiation rates. A slower differentiation rate coincides with a quicker anorthositic mush emplacement, while a faster differentiation rate coincides with slower mush emplacement. 3) Through a brief petrographic study (Section 2.3.1.1) and Remote Sensing (Chapter 2), a link has been shown between pluton composition and age. In general, leuconoritic domains are older than the leucotroctolitic domains. This may imply that the first pulses of magma received a greater degree of contamination, forcing the broadly basaltic magma to produce orthopyroxene as the main mafic phase. The subsequent pulses received less contamination as they ascended through already partially melted crust, producing olivine as the mafic phase and deforming the older domains. In this study a genetic link between domain composition and age has been shown using the precise, absolute age of the anorthositic rocks, rather than indirect methods. The existence of long-lived timescales of Proterozoic anorthosites, in this case, of one of the world's largest anorthositic complexes, the Kunene Anorthosite Complex has been re-emphasised.

4 Summary and Tectonic Setting of the Kunene Anorthosite Complex

4.1 Summary

The enigmatic nature of Proterozoic anorthosites remains a highly debated topic, despite many years of research. Several integral topics such as the sources, emplacement mechanics, and tectonic settings remain unsettled. This study aimed at using two different approaches, namely a remote sensing analysis and high precision U-Pb ID-TIMS analysis to test multiple hypotheses in order to better understand the petrogenesis of the KAC and, in turn, other Proterozoic anorthosites around the globe. Remote sensing was used to identify and classify the magmatic architecture of the KAC with the goal of improving the current understanding of the internal architecture of the KAC. The ID-TIMS study aimed at resolving age differences between domains of differing compositions with the goal of broadening our understanding of anorthositic petrogenesis/processes in the Proterozoic Eon.

Using the KAC to test some of these hypotheses reveals several key ideas:

1) Remote sensing data allows for a first order interpretation of the general architecture of the KAC as well as depicting internal variations in spectral signatures that correlate with variations in composition. In addition, through lineament extraction, new directional data on the internal geometry of the complex within each homogeneous spectral domain is provided. It is suggested that the KAC is composed of at least two main magmatic entities that show different compositions (reflected in the mineral phases present) and geometries forming the overall elongate aspect ratio we see today.

2) New high precision U-Pb ID-TIMS data from the anorthositic rocks show that the KAC magmatism was episodic, and spread over a period of at least 60 Ma. There is also a genetic link between composition and the age. Older leuconoritic pulse intruded first and are interpreted to have experienced a greater degree of crustal contamination. Whereas younger leucotroctolitic pulses intrude through already partially melted crust and experience lower degrees of contamination.

From these datasets we are left with questions regarding what tectonic environment is capable of producing these volumes of anorthositic rocks over relatively long timescales.

4.2 Tectonic Settings of Proterozoic Anorthosites in Literature

4.2.1 Non-convergent Environments

A variety of tectonic settings have been proposed for the formation of Proterozoic anorthosites (Ashwal, 1993). These tectonic environments require sufficient heating to cause melting and produce enough magma to form the Proterozoic anorthosite massifs (Ashwal, 1993; Bybee et al., 2014). The first ideas for a tectonic setting proposed an extensional or rifting environment. This environment enabled sufficient heat and magma delivery into the crust (Berg, 1977; Morse, 1982). Emslie (1978) pointed out that anorogenic bimodal magmatism is the only way for a large amount of heat to be transferred from the mantle to the crust. An issue with a rifting environment is that magmatism in such environments normally operates on shorter timescales (< 1 Ma; Ebinger et al., 2010; Ebinger et al., 2013) than observed in the KAC (~60 Ma; this study) and other Proterozoic anorthosite bodies around the world (~100 Ma; Meyer, 2008; Bybee et al., 2014). Continuous rifting environments on these time scales, and large volumes of magma production should lead to continental break up which is not evident in the case of the Kunene Complex and other Proterozoic anorthosites (Ashwal, 1993). Other possible intra-plate environments include mantle plumes which can account for the formation of a linear array of magmatic bodies through time and the long magmatic timescales. Where this idea falls short is that hotspot plume tracks are generally age progressive in one direction (such as Hawaii) and leave a progressional age track from oldest to youngest magmatic products (Tarduno, 1997). This is not evident in the KAC as there is no such progressive age relationship of magmatic pulses between the north and the south of the elongate batholith (Chapter 3).

4.2.2 Convergent Environments

Based on these arguments a consensus appears to have been reached among geologists studying anorthosites for a convergent tectonic setting for Proterozoic anorthosite formation (Ashwal, 1993; Corrigan and Hammer, 1997; McLelland et al., 2010, Bybee et al., 2014). A continent – continent collision setting favours a lower crustal source over a mantle parental source magma. It does not seem to be the ideal setting as it does not fully allow for all requirements of Proterozoic anorthosite formation. On average, continent – continent collision produces about 2.3 km^3/year less volume of magma than continental arc settings (Hawkesworth et al., 2013). Hence, much more time is required for formation of huge batholith in a collision belt than in a continental arc. Nevertheless, some batholiths formed in continent collision setting are massive (about 10 000 km^2 and possibly up to 30 000 km^2, e.g. the Hook Batholith in central Zambia; Milani et al., 2015), but these are not of basaltic parental sources as it would be required for anorthosite production, but are granitic in composition. Morse (1991) explains that a basaltic magma (the suggested parental source for Proterozoic anorthosites) is unlikely to form in this environment as it would require complete melting of a mafic lower crust to produce basaltic magma or a huge amount of hot underplated material at temperatures of about 1650 °C. These high temperatures imply a preexisting generation of mantle-derived magma and therefore the source would be regarded as a more of a mantle source and not a melted lower crust (Morse, 1991).

A study based on U-Pb ages of zircon from anorthosites in the Adirondack Mountains show ages related to the late- to post-orogenic stages of orogeny (McLelland et al., 2010). There is an extensional period and resulting replacement of the mantle lithosphere with asthenospheric material which occurs as a result of either delamination or convective thinning (Corrigan and Hammer, 1997; McLelland et al., 2010). This study and a recent study by Bybee et al. (2014) shows that typical magmatic durations in late- to post-orogenic stages do not cover the entire timescales observed in Proterozoic anorthositic complexes. Rather the long-lived anorthositic magmatism may start earlier in the orogenic cycle during syn-orogenic magmatism. Geochronological and geochemical evidence from HAOMs that are comagmatic with Proterozoic anorthosites confirms a long-lived timescale of ~100 Ma in many anorthositic bodies (Bybee et al., 2014). The results of this study show an early differentiated anorthositic mush emplaced 40 Ma before the majority of magmatism in the KAC. Additionally evidence from Bybee et al. (2014) shows HAOMs are much older than the anorthosite emplacement themselves. This indicates that there may have been activity during syn-orogenic magmatism with ultimate emplacement extending into the late stages of orogeny.

Therefore, a continental are setting would be appropriate for the earlier magmatism. This setting has many attractive factors that can account for the features seen in the KAC and other Proterozoic anorthosites around the world. The first indication of a continental arc setting can been seen in the linear geometry of some Proterozoic anorthosites as evident in the KAC (see Chapter 2) and other anorthosites (e.g. Grenville Province; Ashwal, 1993, 2004). This is a common and characteristic feature of continental arcs (Ducea et al., 2015). The long magmatic time scales of continental arcs, such as the Californian Arc, with the duration of magmatism for 100's Ma (Ducea, 2001; Ducea et al., 2015), are observed in the KAC (60 Ma; this study), as well as the Mealy Mountains Intrusive Suite, Nain Plutonic Suite, and the Rogaland Anorthosite Province (~80 – 100 MA, see Section 3.1; Bybee et al 2014). Magmatism in continental arcs, and as presented in this study by anorthosites, is commonly associated with episodic magmatic activity (De Silva et al., 2015). This is evident by the 40 Ma period of quiescence of magmatic episodes in the KAC (see Section 3.5.2). Another factor in favour of a continental arc environment is the evidence of magma ponding and crystallisation at appropriate Moho deaths (~35 km). HAOMs (found in the KAC and many other Proterozoic anorthosites) are key indicators of crystallisation at depths of ~35km (see Section 3.5.2). The above arguments suggest that the KAC, as well as other Proterozoic anorthosites, form in a continental arc environment. A regional study of the terranes in and around the KAC needs to be conducted to provide additional evidence and possible relationships to events such as the ~1400 Ma Kibaran orogeny (Maier, 2008).

4.3 Tentative Tectonic Setting and Summary Model for KAC.

Considering all evidence from this study whilst ruling out some of the possibilities of previously suggested tectonic environments, it is suggested that the most favourable tectonic setting for the KAC would be a continental arc setting. This environment fulfills the various requirements observed such as the KAC's map geometry, magma volume, composition, and long-lived timescales. A summary model of the Kunene magmatism is shown in Figure 4.1:

> 1) Initially arc magmatism produced a broadly basaltic melt that ponded at the Moho. These melts continually accumulated and crystallised large quantities of plagioclase rich magma, which begin to differentiate. This magma ultimately became a buoyant crystal-rich mush.
>
> 2) At 1438 Ma, part of this early differentiating magma was emplaced and experienced minimal contamination producing an olivine-dominant magmatic pulse. At 1400 Ma a larger pulse of magma rose through the crust and assimilated

large amounts of crustal material, producing orthopyroxene as the main mafic phase.

3) At 1390 Ma a new pulse of magma was injected into the crust. This magmatic pulse is more heterogeneous in composition than the other pulses, having a common occurrence of both leucotroctolitic to leucogabbronoritic rocks. This may be an indicator of an intermediate contamination of crust and parental magma.

4) The Zebra Lobe intruded at ~1385 Ma. At 1380 Ma – two pulses of magma rose through the crust and were emplaced. These pulses were injected into a crust that had experienced a prior melting event and was refractory, therefore it experienced a lesser degree of contamination. This magma therefore produced olivine as its main mafic phase. Along with the emplacement of these anorthositic imtrusions, Red Granites (with a U-Pb age of ~ 1374 Ma) were emplaced as products of crustal anatexis (Seth et al, 2005). These granites are common throughout the KAC and possibly exhibit a resolvable age difference as well, with Rb-Sr data giving age ranges of 1350 ± 65 – 1411 ± 24 Ma (De Carvalho et al., 1987).

4.4 Conclusion

This dissertation shows how the combination of remote sensing data, ground validation, and high precision geochronology can be used to help understand the petrogenesis, composition, structure, and tectonic setting of the KAC. With the use of multiple image enhancement techniques on Landsat 8, and SRTM datasets, one of the most detailed geological maps of the KAC has been produced. The study also shows the internal heterogeneity and complexity of this anorthositic body. This study reaffirms the batholithic appearance of the KAC and suggests that the complex is made up of two main magmatic entities, which differs in terms of their Landsat spectral response and composition. In addition, remote sensing processing allowed refining the KAC into up to nine domains of contrasting Landsat spectral response as well as density and orientation of SRTM and Landsat lineaments.

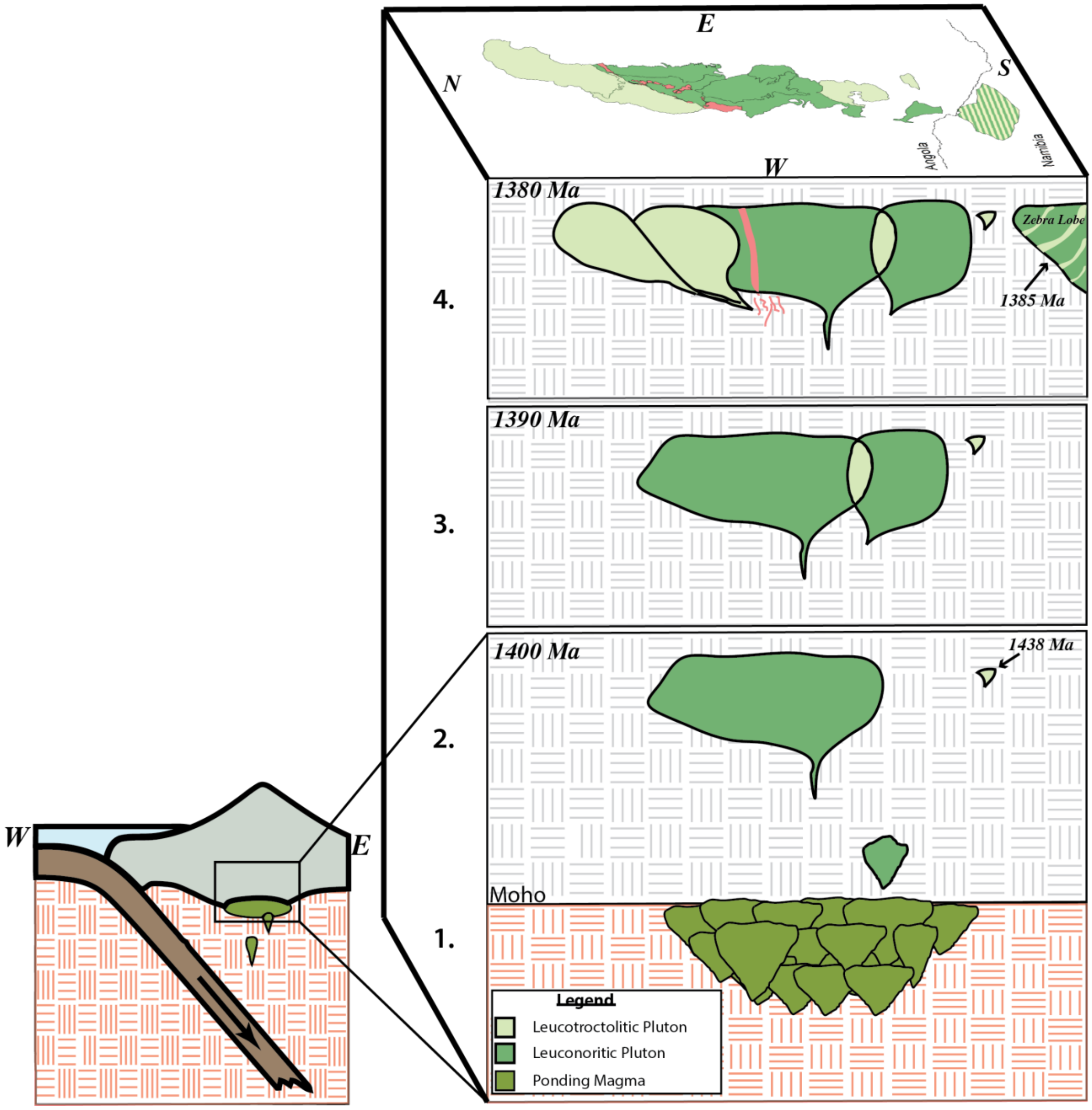

Figure 4.1 - Summary schematic model of the Kunene Anorthosite Complex.

Following the remote sensing study, the age variation between these remote sensing domains has been assessed in order to investigate whether any age relationship exists between them.There is no gradual age progression between domains but distinct groupings of ages in the KAC. There is an age grouping of ~1380 Ma occurring to the north of a NE – SW-striking Red Granite belt, whereas in the south there is an age grouping of 1390 Ma.

Two additional ages of 1400 Ma in the centre and 1438 Ma in the southeast occur. It is also shown that a genetic relationship between the age of the plutons and the composition exists. The younger 1380 Ma plutons are more leucotroctolitic and the older 1400 Ma and 1390 Ma are leuconoritic. This age and composition relationship has been noted by other authors before and suggests that the older leuconoritic magmatic pulse experienced more contamination, producing orthopyroxene as a main mafic phase where the young leucotroctolitic magmatic pulse experienced less contamination and produced olivine as the main mafic phase. The exception to this is the oldest magmatic batch of 1438 Ma which is leucotroctolitic. This body may have experienced less contamination due to its size and not having had enough energy to melt the surrounding rocks. The age data also show that there is at least 60 Ma of pulsed magmatic activity occurring in the KAC. The 1438 Ma body is an indication of magma differentiation 40 Ma before the majority of magma emplacement. Utilizing the remote sensing data and the geochronological results a new model for the petrogenesis of the KAC has been developed and it is suggested that the most valid setting for the KAC is a continental arc. This study reiterates the multiphase petrogenesis of Proterozoic anorthosites and sheds light on the assembly of these crystal-rich magmas in arc environments and their subsequent ascent through the crust.

5 References

Ali, A.S. and Pour, A.B., 2014. Lithological mapping and hydrothermal alteration using Landsat 8 data: a case study in ariab mining district, red sea hills, Sudan. International Journal of Basic and Applied Sciences, 3(3), 199.

Ashwal, L.D., Wooden, J.L., 1983. Isotopic evidence from the eastern Canadian shield for geochemical discontinuity in the Proterozoic mantle. Journal Volume Pages

Ashwal, L.D., 1993, Anorthosites, Springer Berlin Heidelberg.

Ashwal, L.D., Twist, D., 1994. The Kunene complex, Angola/Namibia: a composite massif- type anorthosite complex. Geological Magazine, 131, 579-591.

Ashwal, L.D., 2004. Origin of Anorthosites: Petrological and Tectonic Considerations. AGU Spring Meeting Abstracts

Ashwal, L.D., 2010. The Temporality of Anorthosites. Canadian Mineralogist, 48, 711- 728.

Barker, F., Wones, D.R., Sharp, W.N. and Desborough, G.A., 1975. The Pikes Peak batholith, Colorado Front Range, and a model for the origin of the gabbro— anorthosite—syenite—potassic granite suite. Precambrian Research, 2(2), 97-160.

Barnichon, J.D., Havenith, H., Hoffer, B., Charlier, R., Jongmans, D., Duchesne, J.C., 1999. The Deformation of the Egersund-Ogna massif, South Norway: Finite Element modelling of diapirism. Tectonophysics, 303, 109-130.

Baxe, O.S.S., 2007. Geocronologia de complexos máfico-ultramáficos: exemplo da série superior do complexo de Niquelândia, Brasil, e do complexo Kunene, Angola. M.Sc. Dissertation (unpublished). Universidade de Brasília, Instituto de Geociências, 46-74

Bédard, J.H., 2010. Parental magmas of Grenville Province massif-type anorthosites, and conjectures about why massif anorthosites are restricted to the Proterozoic. Geological Society of America Special Papers, 472, 77-103.

Bowen, N.L., 1917. The Problem of Anorthosites. The Journal of Geology, 25, 209-243.

Bowen, N.L. 1922. The Reaction Principle In Petrogenesis. The Journal of Geology 30, 177-198.

Brandt, S., Will, T.M., Klemd, R., 2007. Magmatic Loading In The Proterozoic Epupa Complex, NW Namibia, As Evidence By Ultra-High-Temperature Sapphitine-Bearing Orthopyroxene – Sillimanite- Quartz Granulites. Precambrian Research. 153, 143-178.

Brandt, S., Klemd, R., 2008. Upper-Amphibolite Facies Partial Melting Of Paragneisses From The Epupa Complex, NW Namibia, And Relations To Mesoproterozoic Anorthosite Magmatism. Journal of Metamorphic Geology. 26, 871-893.

Buddington, A.F., 1939. Adirondack igneous rocks and their metamorphism. Geological Society of America Memoir, 7, 343.

Bybee, G.M., Ashwal, L.D., Shirey, S.B., Horan, M., Mock, Andersen, T.B., 2014. Pyroxene megacrysts in Proterozoic anorthosites: Implications for tectonic setting, magma source and magmatic processes at the Moho. Earth and Planetary Science Letters, 389, 74-85.

Bybee, G.M. and Ashwal, L.D., 2015. Isotopic disequilibrium and lower crustal contamination in slowly ascending magmas: Insights from Proterozoic anorthosites. Geochimica et Cosmochimica Acta, 167, 286-300.

Charlier, B., Duchesne, J.C., Vander Auwera, J., Storme, J.Y., Maquil, R. and Longhi, J., 2010. Polybaric fractional crystallisation of high-alumina basalt parental magmas in the Egersund–Ogna massif-type anorthosite (Rogaland, SW Norway) constrained by plagioclase and high-alumina orthopyroxene megacrysts. Journal of Petrology, 51 (12), 2515-2546.

Charlier, B., Namur, O., Bolle, O., Latypov, R. and Duchesne, J.C., 2015. Fe–Ti–V–P ore deposits associated with Proterozoic massif-type anorthosites and related rocks. Earth-Science Reviews, 141, 56-81.

Corfu, F., 2004, U–Pb age, setting and tectonic significance of the anorthosite–mangerite– charnockite–granite suite, Lofoten–Vesterålen, Norway. Journal of Petrology, 45(9), 1799-1819.

Corrigan, D. and Hanmer, S., 1997. Anorthosites and related granitoids in the Grenville orogen: A product of convective thinning of the lithosphere? Geology, 25(1), 61- 64.

Cruden, A.R., 1990. Flow and fabric development during the diapiric rise of magma. Journal of Geology, 98, 681-698.

De Carvalho, H.D., Crasto, J.P., Silva, Z.C.G. and Vialette, Y., 1987. The Kibaran cycle in Angola—a discussion. Geological Journal, 22(S2), 85-102.

De Carvalho, H., Alves, P., 1990. Gabbro-Anorthosite Complex of SW Angola/NW Namibia. Comunicações Instituto Investigação Cient´Ifica Tropical, Serie De Ciencias Da Terra, Lisboa, 5–64.

De Silva, S.L., Riggs, N.R. and Barth, A.P., 2015. Quickening the pulse: Fractal tempos in continental arc magmatism. Elements, 11(2), 113-118.

Drüppel, K., von Seckendorf, V., Okrusch, M., 2001. Subsolidus reaction textures in anorthositic rocks of the southern part of te Kunene Intrusive Complex, NW Namibia. European Journal of Mineralogy. 13, 289– 309.

Drüppel, K., Littmann, S., Romer, R.L., Okrusch, M., 2007. Petrology and isotope geochemistry of the Mesoproterozoic anorthosite and related rocks of the Kunene Intrusive Complex, NW Namibia. Precambrian Res. 156, 1–31.

Drury, S., 2001. Image Interpretation in Geology 3rd Ed., Blackwell Science

Inc. Ducea, Miah. 2001 The California arc. GSA Today, 11 (11), 4-10.

Ducea, M.N., Saleeby, J.B. and Bergantz, G., 2015. The architecture, chemistry, and evolution of continental magmatic arcs. Annual Review of Earth and Planetary Sciences, 43, 299-331.

Duchesne, J.-C. *et* al., 1999. The crustal tongue melting model and the origin of massive anorthosites. Terra Nova, 11, 100-105.

Emslie, R.F., 1975. Pyroxene megacrysts from anorthositic rocks; new clues to the sources and evolution of the parent magmas. The Canadian Mineralogist, 13(2), 138- 145.

Emslie, R.F., 1978. Anorthosite massifs, rapakivi granites, and late Proterozoic rifting of North America. Precambrian Research, 7, 61-98.

Emslie, R.F., 1985. Proterozoic anorthosite massifs. In (Tobi, A.C. and Touret, L.R.) The deep Proterozoic crust in the North Atlantic provinces, Springer Netherlands, 39-60.

Emslie, R., Hamilton, M. & Theriault, R., 1994. Petrogenesis of a Mid-Proterozoic Anorthosite-Mangerite-Charnockite-Granite (AMCG) Complex: Isotopic and Chemical Evidence from the Nain Plutonic Suite. The Journal of Geology, 102, 539-558.

Ebinger, Cynthia, et al., 2010, Length and timescales of rift faulting and magma intrusion: The Afar rifting cycle from 2005 to present. Annual Review of Earth and Planetary Sciences 38, 439-466.

Ebinger, Cynthia J., Jolante van Wijk, and Derek Keir, 2013, The time scales of continental rifting: Implications for global processes. Geological Society of America Special Papers 500, 371-396.

Felde, G.W., Anderson, G.P., Cooley, T.W., Matthew, M.W., Berk, A. and Lee, J., 2003, July. Analysis of Hyperion data with the FLAASH atmospheric correction algorithm. In Geoscience and Remote Sensing Symposium, 2003. IGARSS'03. Proceedings. IEEE International, 1, 90-92.

Frost, C.D., Frost, B.R., Lindsley, D.H., Chamberlain, K.R., Swapp, S.M. and Scoates, J.S., 2010. Chemical and isotopic evolution of the anorthositic plutons of the Laramie Anorthosite Complex: Explanations for variations in silica activity and oxygen fugacity of massif anorthosites. The Canadian Mineralogist, 48(4), 925-946.

Gad, S. & Kusky, T., 2006. Lithological Mapping In The Eastern Desert Of Egypt, The Barramiya Area , Using Landsat Thematic Mapper (TM). , 44, 196–202.

Gleißner, P., Drüppel, K., Taubald, H., 2010. Magmatic evolution of anorthosites of the Kunene Intrusive Complex, NW Namibia: evidence from oxygen isotope data and trace element zoning. Journal of Petrology. 51, 897–919.

Gleißner, P., Drüppel, K. & Romer, R.L., 2011. The role of crustal contamination in massif- type anorthosites, new evidence from Sr-Nd-Pb isotopic composition of the Kunene Intrusive Complex, NW Namibia. Precambrian Research, 185, 18–36.

Goldich, S.S. 1938. A Study In Rock Weathering. Journal Of Geology 46: 17-58.

Green, A.A., Berman, M., Switzer, P. and Craig, M.D., 1988. A transformation for ordering multispectral data in terms of image quality with implications for noise removal. IEEE Transactions on geoscience and remote sensing, 26(1), 65-74.

Gupta, R.P., Tiwari, R.K., Saini, V. and Srivastava, N., 2013. A simplified approach for interpreting principal component images, 111–119.

Harris, J.R., Ponomarev, P., Shang, J. and Rogge, D., 2006. Noise reduction and best band selection techniques for improving classification results using hyperspectral data: application to lithological mapping in Canada's Arctic. Canadian Journal of Remote Sensing, 32(5), 341-354.

Hawkesworth, C., Cawood, P. and Dhuime, B., 2013. Continental growth and the crustal record. Tectonophysics, 609, 651-660.

Heinonen, A.P., Rämö, O.T., Mänttäri, I., Johanson, B. and Alviola, R., 2010. Formation and fractionation of high-Al tholeiitic magmas in the Ahvenisto rapakivi granite–massif- type anorthosite complex, southeastern Finland. The Canadian Mineralogist, 48(4), 969-990.

Inzana, J., Kusky, T., Higgs, G. and Tucker, R., 2003. Supervised classifications of Landsat TM band ratio images and Landsat TM band ratio image with radar for geological interpretations of central Madagascar. Journal of African Earth Sciences, 37(1), 59-72.

Jaffey, A.H., Flynn, K.F., Glendenin, L.E., Bentley, W.T. and Essling, A.M., 1971. Precision measurement of half-lives and specific activities of U 235 and U 238. Physical Review C, 4(5), 1889.

Jolliffe, I.T., 2002. Principal Component Analysis, John Wiley & Sons, Ltd.

Köstlin, E. C., 1974, "The Kunene Basic Complex, Northern South West Africa." In Contributions To The Precambrian Geology Of Southern Africa, 15, 123-135.

Kruse, F.A., 1996. Ologic Mapping Using Combined Analysis Of Airborne Visible/Infrared Imaging Spectrometer (AVIRIS) And SIR-C/X-SAR Data. SPIE's 1996 International Symposium On Optical Science, Engineering, And Instrumentation. International Society For Optics And Photonics.

Krogh, T. E. (1973). A low contamination method for hydrothermal decomposition of zircon and extraction of U and Pb for isotopic age determinations. Geochimica et Cosmochimica Acta 37, 485–494.

Krogh, T. E. (1982). Improved accuracy of U–Pb zircon ages by the creation of more concordant systems using an air abrasion technique. Geochimica et Cosmochimica Acta 46, 637–649.

Kushiro, I., 1980. Viscosity, density, and structure of silicate melts at high pressures, and their petrological applications. In: Hargraves R.B. (ed.) Physics of magmatic processes. Princeton University Press, Princeton, NJ, 93-120.

Longhi, J., Fram, M.S., Vander Auwera, J. and Montieth, J.N., 1993. Pressure effects, kinetics, and rheology of anorthositic and related magmas.

American Mineralogist, 78(9-10), 1016-1030.

Longhi, J., 2005. A mantle or mafic crustal source for Proterozoic anorthosites? Lithos, 83, 183-198.

Lopes, Fernando Carlos, et al. "Morphostructural characterization of the western edge of the Huila Plateau (SW Angola), based on remote sensing techniques." Journal of African Earth Sciences 117 (2016): 114-123.

Ludwig, K. R. (1999). Isoplot/Ex Version 2.03. A Geochronological Toolkit for Microsoft Excel. Berkeley Geochronology Center Special Publication 1, 43.

Martignole, J. & Schrijver, K., 1970. Tectonic setting and evolution of the Morin anorthosite, Grenville Province, Quebec. Bulletin of the Geoogical Society of Finland, 42, 165-209.

Matthew, M.W., Adler-Golden, S.M., Berk, A., Felde, G., Anderson, G.P., Gorodetzky, D., Paswaters, S. and Shippert, M., 2002, October. Atmospheric correction of spectral imagery: evaluation of the FLAASH algorithm with AVIRIS data. In Applied Imagery Pattern Recognition Workshop, 2002. Proceedings. 31st, 157-163.

Mayer, A., Hofmann, A., Sinigoi, S., Morais, E., 2004. Mesoproterozoic Sm-Nd and U-Pb ages for the Kunene anorthosite Complex of SW Angola. Precambrian Research 133, 187–206.

Maier, W.D., 2008. The Kunene anorthosite complex, its satellite intrusions, and possible links to early Kibaran intrusions in Tanzania and Burundi. October 2008 LIP of the Month. http://www.largeigneousprovinces.org/08oct

Maier, W. D., Rasmussen, B., Fletcher, I. R., Li, C., Barnes, S. J., & Huhma, H. 2013. The Kunene Anorthosite Complex, Namibia, and its satellite intrusions: geochemistry, geochronology, and economic potential. Economic Geology, 108, 953-986.

McCourt, S., Armstrong, R.A., Jelsma, H. and Mapeo, R.B.M., 2013. New U–Pb SHRIMP ages from the Lubango region, SW Angola: insights into the Palaeoproterozoic evolution of the Angolan Shield, southern Congo Craton, Africa. Journal of the Geological Society, 170(2), 353-363.

McLelland, J.M., Selleck, B.W., Hamilton, M.A. and Bickford, M.E., 2010. Late- to post- tectonic setting of some major Proterozoic anorthosite–mangerite–charnockite– granite (AMCG) suites. The Canadian Mineralogist, 48(4), 729-750.

Menge, G. F. W. (1998). The antiformal structure and general aspects of the Kunene Complex, Namibia. Zeitschrift der Deutschen Geologischen Gesellschaft 149, 433- 448.

Milani, L., Lehmann, J., Naydenov, K.V., Saalmann, K., Kinnaird, J.A., Daly, J.S., Frei,

D. and Sanz, A.L.G., 2015. A-type magmatism in a syn-collisional setting: The case of the Pan-African Hook Batholith in Central Zambia. Lithos, 216, 48-72.

Miller, R.McG., Schalk, K.E.L., 1980, Geological Survey of Namibia, 1:1000000

Mitchell, J., Scoates, J. & Frost, C., 1995. High-Al Gabbros in the Laramie Anorthosite Complex, Wyoming - Implications for the Composition of Melts Parental to Proterozoic Anorthosite. Contributions to Mineralogy and Petrology, 119, 166- 180.

Morais, E., Sinigoi, S., Mayer, A., Mucana, A., Miguel, L. G., Rufino Neto, J. (1998). The Kunene Gabbro-Anorthosite Complex: Preliminary Results Based On New Field and Chemical Data. African Geoscience Review 5, 485-498.Morse, S.A., 1982. A Partisan Review of Proterozoic Anorthosites. The American Mineralogist, 67, 1087- 1100.

Morse, S.A., 1982. A partisan review of Proterozoic anorthosites. The American Mineralogist, 67, 1087- 1100.

Morse, S.A., 1991. Basaltic magma from the crust is not a free option. Eos, Transactions American Geophysical Union, 72(14), 161-161.

Mshiu, E.E., 2011. Remote Sensing Data As An Alternative Approach For Geological Mapping In Tanzania: A Case Study In The Rungwe Volcanic Province, South- Western Tanzania. Tanzania Journal of Science, 37(1), 26–36.

Owojori, A. & Xie, H., 2005. Landsat image-based lulc changes of san antonio , texas using advanced atmospheric correction and object- oriented image analysis approaches. Proceedings of the 5th International Symposium on Remote Sensing Of Urban Areas, (January), 14–16.

Paterson, S.R., Fowler, T.K., Schmidt, K.L., Yoshinobu, A.S., Yuan, E.S. and Miller, R.B., 1998. Interpreting magmatic fabric patterns in plutons. Lithos, 44(1), 53-82.

PCI Geomatica Users' Manual, 2016

Peck, W.H., Clechenko, C.C., Hamilton, M.A. and Valley, J.W., 2010. Oxygen isotopes in the Grenville and Nain AMCG suites: Regional aspects of the crustal component in massif anorthosites. The Canadian Mineralogist, 48(4), 763-786.

Perkins, T., Adler-Golden, S., Matthew, M., Berk, A., Anderson, G., Gardner, J. and Felde, G., 2005, October. Retrieval of atmospheric properties from hyper and multispectral imagery with the FLAASH atmospheric correction algorithm. In Remote Sensing, International Society for Optics and Photonics.

Pour, A.B. & Hashim, M., 2015. Hydrothermal Alteration Mapping From Landsat-8 Data, Sar Cheshmeh Copper Mining District, South-Eastern Islamic Republic Of Iran. Journal of Taibah University for Science, 9(2), 155–166.

Ramsey, J.G., 1989. Emplacement kinetics of a granite diapir: the Chindamora batholith, Zimbabwe. Journal of Structural Geology, 11, 191-209.

Royse, K. & Park, R., 2000. Emplacement of the Nain anorthosite: diapiric versus conduit ascent. Canadian Journal of Earth Sciences, 37, 1195-1207.

Sauer, S., Slagstad, T., Andersen, T. and Kirkland, C.L., 2013, April. Zircon Lu-Hf isotopes in high-alumina orthopyroxene megacrysts from the Neoproterozoic Rogaland Anorthosite Province, SW Norway: A window into the Sveconorwegian lower crust. In EGU General Assembly Conference Abstracts, 15, 13958.

Scoates, J.S. and Chamberlain, K.R., 1995. Baddeleyite (ZrO2) and zircon (ZrSiO4) from anorthositic rocks of the Laramie anorthosite complex, Wyoming: petrologic consequences and U-Pb ages.

Schiellerup, H., Lambert, D.D., Prestvik, T., Robins, B., McBride, J.S. and Larsen, R.B., 2000. Re–Os isotopic evidence for a lower crustal origin of massif-type anorthosites. Nature, 405(6788), 781-784.

Seth, B., Armstrong, R.A., Büttner, A. and Villa, I.M., 2005. Time constraints for Mesoproterozoic upper amphibolite facies metamorphism in NW Namibia: a multi- isotopic approach. Earth and Planetary Science Letters, 230(3), 355-378.

Serviços De Geologia E Minas De Angola. Carta Geologica De Angola 1:100,000 Folha No 356 SUL D-33 T-II.

Serviços De Geologia E Minas De Angola. Carta Geologica De Angola 1:100,000 Folha No 377 SUL D-33 T-IV.

Serviços De Geologia E Minas De Angola. Carta Geologica De Angola 1:250,000 Folha SUL D-33 O.

Serviços De Geologia E Minas De Angola. Carta Geologica De Angola 1:250,000 Folha SUL D-33 U.

Serviços De Geologia E Minas De Angola. Carta Geologica De Angola 1:250,000 Folha SUL E-33 B-C-H-I.

Silva, Z.C.G., 1990. Geochemistry Of The Gabbro-Anorthosite Complex Of Southwest Angola. J. Afr. Earth Sci. 10, 683-692.

Silva, Z.C.G., 1992. Minearalogy and Cryptic Layering Of The Kunene Anorthosite Complex Of SW Angola And Namibia. Miner. Magazine 56, 319–327.

Slejko, F.F., Demarchi, G. and Morais, E., 2002. Mineral chemistry and Nd isotopic composition of two anorthositic rocks from the Kunene complex (South Western Angola). Journal of African Earth Sciences, 35(1), 77-88.

Soe, M., Kyaw, T.A. & Takashima, I., 2005. Application Of Remote Sensing Techniques On Iron Oxide Detection From ASTER And Landsat Images Of Tanintharyi Coastal Area, Myanmar , 21–28.

Streckeisen, A., 1976. To each plutonic rock its proper name. Earth Science Reviews, 12, 1-33.

Tarduno, J.A. and Cottrell, R.D., 1997. Paleomagnetic evidence for motion of the Hawaiian hotspot during formation of the Emperor seamounts. Earth and Planetary Science Letters, 153(3-4), 171-180.

Taylor, S.R., Campbell, I.H., McCulloch, M.T. and McLennan, S.M., 1984. A lower crustal origin for massif-type anorthosites. Nature, 311(5984), 372-374.

Valley, J. & O'Neil, J.R., 1982. Oxygen isotope evidence for shallow emplacement of Adirondack anorthosite. Nature, 300, 497-500.

Van Breemen, O., Davidson, A., Loveridge, W.D., Sullivan, R.W., 1986. U-Pb zircon geochronology of Grenville tectonites, granulites and igneous precursors, Parry Sound, Ontario. In: Moore, J.M., Davidson, A., Baer, A.J. (Eds.), The Grenville Province. Geological Association of Canada Special Paper 31, 191–207

Villanova, C., Gali, S., Torro,L. ,Castillo,M., Campeny,M., Concalves, A.O., Melgarejo, J.C., Ti-V oxide deposits in the Kunene anorthositic complex (SW Angola), EG50G – Economic Geology (metallic and non-metallic ore deposits)

Waldhoff, G., Bubenzer, O., Bolten, A., Koppe, W. and Bareth, G., 2008, July. Spectral analysis of ASTER, Hyperion, and QuickBird data for geomorphological and geological research in Egypt (Dakhla Oasis, Western Desert). In Proc. XXI ISPRS Congress, Commission VIII (Vol. 38, p. B8).

Wiebe, R.A., 1990. Evidence for Unusually Feldspathic Liquids in the Nain Complex, Labrador. American Mineralogist, 75, 1–12

Appendix A – Literature Ages of the KAC

All geochronological samples found in literature are represented in the table below.

Latitude	Longitude	Rock Type	Method	WR/Mineral	Age (Ma)	Interpretation	Comment	Locality precision	Reference
14.9833 E	14.1333 S	Dolertite	K-Ar	Pl	880 ± 34	Crystallisation Age	G1/318 (Silva et al 1973)	<50 m	De Carlvalho et al.,1987
13.5589 E	15.2631 S	Gabbro-norite Dyke	U-Pb	Baddeleyite	1110.3 ± 2.5	Crystallisation Age	Sample-356-17,ID-TIMS method, MSWD 0.7	<50 m	Ernst et al., 2013
14.2500 E	14.1500 S	Dolertite	K-Ar	Pl	1157 ± 26	Crystallisation Age	G54/317(Silva et al 1973)	<50 m	De Carlvalho et al.,1987
14.1000 E	14.0667 S	Dolertite	K-Ar	Pl	1175 ± 69	Crystallisation Age	G24/317(Silva et al 1973)	<50 m	De Carlvalho et al.,1987
13.2865 E	17.4879 S	Troctolite	U-Pb	Baddeleyite	1220 ± 31	Emplacement Age	HRDD-1 102.8m, MSWD 1.4, Ohamaremba satellite body (approximate position)	<1KM	Maier et al., 2013
13.2865 E	17.4879 S	Troctolite	U-Pb	Baddeleyite	1220 ± 20	Emplacement Age	HRDD-1 160.62m, MSWD 0.72, Ohamaremba satellite body (approximate position)	<1KM	Maier et al., 2013
14.1500 E	14.2167 S	Dolertite	K-Ar	Pl	1281 ± 22	Crystallisation Age	G17/317(Silva et al 1973)	<50 m	De Carlvalho et al.,1987
14.1500 E	14.2000 S	Dolertite	K-Ar	Pl	1301 ± 65	Crystallisation Age	G16/317(Silva et al 1973)	<50 m	De Carlvalho et al.,1987
13.6500 E	17.0667 S	Red granite	Rb-Sr	WR	1302 ± 20	Minimum Age	Red granite suite near Chitado border	<50 m	De Carlvalho et al.,1987

							(Angola/Namibia), MSWD1.5		
14.6500 E	14.100 S	Dolertite	K-Ar	Pl	1309 ± 99	Crystallisation Age	G5/318(Silva et al 1973)	<50 m	De Carlvalho et al.,1987
13.7658 E	17.4642 S	garnet–amphibolite	Sm–Nd	Garnet	1317 ± 3	Metamorphic Age	Sample-191-B, MSWD 0.9	<50 m	Seth et al., 2005
13.7322 E	17.4617 S	orthogneiss	U-Pb	Zr	1317.6 ± 8.5	Metamorphic Age	Sample-702	<50 m	Seth et al., 2005
13.9363 E	15.1913 S	Anorthosite dyke	Sm-Nd	WR	1319 ± 28	Crystallisation Age	MSWD 0.49, (wr + plag Phenocryst + plag groundmass)	<50 m	Meyer et al., 2004
13.8133 E	17.4625 S	metapelitic gneiss	U-Pb	Zr	1323.1 ± 9.8	Metamorphic Age	Sample-342-3	<50 m	Seth et al., 2005
13.8133 E	17.4625 S	leucosome	U-Pb	Zr	1328.5 ± 6.6	Metamorphic Age	Sample-342-5	<50 m	Seth et al., 2005
13.6333 E	17.4492 S	metapelitic gneiss	Sm–Nd	Garnet-feldspar	1333 ± 9	Metamorphic Age	Sample-302-2	<50 m	Seth et al., 2005
13.7658 E	17.4642 S	garnet–amphibolite	Lu–Hf	Garnet	1338 ± 3	Metamorphic Age	Sample-191-B, MSWD 5.2	<50 m	Seth et al., 2005
13.3333 E	17.4569 S	metapelitic gneiss	U-Pb	Zr	1339.7 ± 7.4	Metamorphic Age	Sample-246A	<50 m	Seth et al., 2005
13.6333 E	17.4492 S	metapelitic gneiss	Lu–Hf	Garnet-feldspar	1342 ± 1	Metamorphic Age	Sample-302-2	<50 m	Seth et al., 2005
14.9961 E	14.6503 S	Red granite	Rb-Sr	WR	1350 ± 65	Crystallisation Age	Matala region (approximate position)	<50 m	De Carlvalho et al.,1987
13.7458 E	17.5633 S	garnet–amphibolite	U-Pb	Zr	1356.5 ± 14.4	Metamorphic Age	Sample-311-3	<50 m	Seth et al., 2005
13.6610 E	17.4374 S	Leucotroctolite	U-Pb	Baddeleyite	1363 ± 17	Emplacement Age	OJS10, MSWD 1.0 (Manual estimated position)	<1KM	Maier et al., 2013
14.0272 E	15.4227 S	Mangerite dyke	U-Pb	Zr	1371.3 ± 2.5	Emplacement Age	Coeval with Kunene complex. Anorthosite still	<50 m	Meyer et al., 2004

							hot when emplaced (no chilled margin). Multi grain vapour dissolution analyses		
13.7708 E	17.4333 S	Granite	U-Pb	Zr	1374 ± 5.2	Crystallisation Age	Sample-180-1	<50 m	Seth et al., 2005
13.7845 E	17.3761 S	Syenodiorite	U-Pb	Zr	1376 ± 2	Crystallisation Age	sample number:ku98-201, Associated felsic rock	<1KM	Druppel et al., 2007
13.7662 E	17.1324 S	Leucogabbronorite	U-Pb	Zr	1385 ± 25	Crystallisation Age	subconcordant	<1KM	Druppel et al, 2000
14.0227 E	15.4198 S	Mangerite dyke	U-Pb	Zr	1385 ± 7.6	Crystallisation Age	Sample-00-L4, Min age of Kunene complex or coeval as suggested by Mayer 2004	<50 m	McCourt et al., 2013
13.9522 E	16.6703 S	Mangerite dyke	U-Pb	Zr	1403 ± 7.1	Crystallisation Age	Sample OSCK 64 - MSWD 8.9 , Mangerite Vein	<50 m	Baxe et al., 2007
13.9363 E	15.1913 S	Anorthosite dyke	Rb-Sr	wr+plag phenocryst	1406 ± 97	Crystallisation Age	MSWD1.2, (wr +plag phenocryst).Quenched in a short time	<50 m	Meyer et al., 2004
13.4667 E	16.1833 S	Red granite	Rb-Sr	WR	1407 ± 26	Crystallisation Age	Ompupa region-in contact with basement and KAC, MSWD0.79	<50 m	De Carlvalho et al.,1987
13.9333 E	16.4833 S	Red granite	Rb-Sr	WR	1411 ± 24	Crystallisation Age	Otchinjau region, MSWD0.32	<50 m	De Carlvalho et al.,1987
13.9121 E	16.9924 S	Olivine gabbro	U-Pb	Zr	1434 ± 2	Crystallisation Age	Sample ONC 88	<50 m	Baxe et al., 2007
14.0965 E	15.0663 S	Anorthosite	Rb-Sr	wr+Pl+opx	1464 ± 140	Crystallisation Age	MSWD 1.05, (wr+plag+opx)"rep cumulate from relative prim magma"	<50 m	Meyer et al., 2004

14.0965 E	15.0663 S	Anorthosite	Sm-Nd	wr+Pl+opx+bio	1470 ± 25	Crystallisation Age	MSWD 1.6, (wr+plag+opx+bio)."rep cumulate from relative prim magma"	<50 m	Meyer et al., 2004
13.5731 E	17.5538 S	MgAl-rich granulite-lens	PbSL	Spr	1487 ± 50	Isochron Age	Sample-700, MSWD 0.48	<1KM	Seth et al., 2003
13.5092 E	15.2308 S	Dolerite Sill	U-Pb	Baddeleyite	1501.5 ± 3.6	Crystallisation Age	Sample-356-56, ID-TIMS method, MSWD 0.3	<50 m	Ernst et al., 2013
13.5941 E	17.5447 S	Meta-Semipelite	U-Pb	Zr	1510.7 ± 6.2	Metamorphic Age	Sample- 614-10, MSWD 1.15, PbSL garnet age 1491 ± 53 (MSWD 3.1)	<1KM	Seth et al., 2003
13.6905 E	17.5190 S	Enderbite	U-Pb	Zr	1513.8 ± 4.6	Metamorphic Age	Sample- 329-1, Concordant with 1σ confidence level , PbSL garnet age 1462 ± 67 (MSWD 0.46)	<1KM	Seth et al., 2003
13.3466 E	17.5308 S	Charnockite	U-Pb	Zr	1515 ± 10	Metamorphic Age	Sample- 661-2, MSWD 0.058	<1KM	Seth et al., 2003
13.6209 E	17.5134 S	Mafic granulite	U-Pb	Zr	1516.8 ± 2.7	Metamorphic Age	Sample-434-2, MSWD 1.07 , PbSL garnet age 1485 ± 120 (MSWD 0.31)	<1KM	Seth et al., 2003
13.5166 E	17.5739 S	Quartz-free metapelite	U-Pb	Zr	1520.5 ± 8.2	Metamorphic Age	Sample- 212-A, MSWD 0.82, PbSL garnet age 1447 ± 37 (MSWD 0.81)	<1KM	Seth et al., 2003
12.9310 E	17.0210 S	Hornblende-bearing granite	U-Pb	Zr	1521.6 ± 1.5	Crystallisation Age	Na173, Southern bank of Kunene River, Red, unfoliated hornblende-bearing granite	<50 m	Kröner et al., 2015

13.5877 E	17.5454 S	Metapelite	U-Pb	Zr	1525.7 ± 8.6	Metamorphic Age	Sample- 615-5, MSWD 1.6	<1KM	Seth et al., 2003
12.8774 E	17.0650 S	Granite	U-Pb	Zr	1533.5 ± 2.9	Crystallisation Age	Na179, Southern bank of Kunene River, Unfoliated, red S-type granite cutting older gneiss	<50 m	Kröner et al., 2015
14.2197 E	17.3926 S	Augen-gneiss	U-Pb	Zr	1774.8 ± 1	Crystallisation Age	Na188, Lookout point on Ruacana Falls, Kunene River, Coarse-grained augen-gneiss	<50 m	Kröner et al., 2015
14.1832 E	17.4273 S	Granite	U-Pb	Zr	1778.1 ± 4.3	Crystallisation Age	Na189, West of Hippo Pool on Kunene River, Boulder of red granite cutting coarse augen gneiss	<50 m	Kröner et al., 2015
13.2207 E	16.9866 S	Granite–gneiss	U-Pb	Zr	1782.7 ± 0.9	Crystallisation Age	Na161, Southern bank of Kunene River west of Epupa Falls ,Strongly foliated, almost mylonitic granite–gneiss	<50 m	Kröner et al., 2015
13.2207 E	16.9958 S	Granite–gneiss	U-Pb	Zr	1790 ± 11	Crystallisation Age	Na03/81, Small river bed SW of Epupa Falls ,Strongly foliated, almost mylonitic granite–gneiss	<50 m	Kröner et al., 2015
13.0882 E	16.9958 S	Granite–gneiss	U-Pb	Zr	1790.6 ± 3.6	Crystallisation Age	Na03/82, Small river bed SW of Epupa Falls ,Migmatitic porphyritic granite–gneiss	<50 m	Kröner et al., 2015

12.8774 E	17.0650 S	Migmatitic granodioritic gneiss	U-Pb	Zr	1793.6 ± 3.1	Crystallisation Age	Na178, Southern bank of Kunene River, Foliated, slightly migmatitic granodioritic gneiss	<50 m	Kröner et al., 2015
12.8908 E	17.0504 S	Hornblende-granodiorite	U-Pb	Zr	1794.5 ± 1.6	Crystallisation Age	Na177, Southern bank of Kunene River, Weakly foliated hornblende-granodiorite	<50 m	Kröner et al., 2015
13.0905 E	16.9973 S	Metagabbro	U-Pb	Zr	1800.2 ± 3.6	Crystallisation Age	Na164, Southern bank of Kunene River, Coarse-grained, weakly foliated metagabbro	<50 m	Kröner et al., 2015
13.8887 E	15.2468 S	Xenolith	U-Pb	Zr	1803.4 ± 9.6	Original age or rock	Sample-CHN-1, MSWD 0.95	<50 m	McCourt et al., 2013
13.1792 E	14.8486 S	Hornblende granite	U-Pb	Zr	1810 ± 11	Crystallisation Age	Sample-335-22, MSWD 45	<50 m	pereira et al., 2011
12.9910 E	16.9923 S	Hornblende-granodiorite	U-Pb	Zr	1812.8 ± 2.8	Crystallisation Age	Na171, Southern bank of Kunene River, Coarse-grained, unfoliated hornblende-granodiorite	<50 m	Kröner et al., 2015
13.2425 E	15.0706 S	Rhyolite	U-Pb	Zr	1814 ± 88	Emplacement Age	Sample-355-2, MSWD 113	<50 m	pereira et al., 2011
13.0071 E	16.9814 S	Granite–gneiss	U-Pb	Zr	1814.6 ± 1.5	Crystallisation Age	Na168, Southern bank of Kunene River, Migmatitic biotite-garnet granite–gneiss	<50 m	Kröner et al., 2015
13.6024 E	17.5557 S	Metapelite	U-Pb	Zr	1828.5 ± 7.1	Metamorphic Age?	Sample- 230-E, MSWD 0.79, PbSL garnet age 1484 ± 37 (MSWD 1.6)	<1KM	Seth et al., 2003

13.2035 E	16.9895 S	Quartzo-feldspathic paragneiss	U-Pb	Zr	<1830	Crystallisation Age	Na162, Southern bank of Kunene River ,Well layered quartzo-feldspathic paragneiss	<50 m	Kröner et al., 2015
13.0844 E	16.9910 S	Granite	U-Pb	Zr	1835.9 ± 0.9	Crystallisation Age	Na166, Eyao River, south of Kunene River, Well foliated granite cutting supracrustal rocks	<50 m	Kröner et al., 2015
13.4678 E	14.7181 S	Coarse biotite granite	U-Pb	Zr	1947 ± 5	Crystallisation Age	Sample-335-9, MSWD 29	<50 m	pereira et al., 2011
13.4392 E	14.8422 S	Granite	U-Pb	Zr	1953.8 ± 6.4	Emplacement Age	Sample-00-L10, MSWD 1.00	<50 m	McCourt et al., 2013
15.0000 E	14.7622 S	Ol-gabbronorite	K-Ar	Pl	1964 ± 61	Crystallisation Age	30 km east of town(Quipango)	<1KM	Silva et al. ,1973
13.8887 E	15.2468 S	Xenolith	U-Pb	Zr	1967 ± 11	Inheritace age	Sample-CHN-1, MSWD 0.38	<50 m	McCourt et al., 2013
13.2397 E	15.0502 S	Granite	U-Pb	Zr	2038 ± 28	Emplacement Age	Sample-00-L1, MSWD 0.74	<50 m	McCourt et al., 2013
13.4797 E	14.8356 S	Foliated granite	Rb-Sr	Unknown	2100 ± 100	Crystallisation Age	Sample-335-8	<50 m	Torquato et al., 1979
14.3184 E	14.8127 S	Anorthosite	K-Ar	Pl	2102 ± 51	Crystallisation Age	Anorthosite samples from specimen near Quipango. 25 km west of town	<1KM	Silva et al. ,1973
14.4213 E	14.8315 S	Anorthosite	K-Ar	Pl	2157 ± 43	Crystallisation Age	Anorthosite samples from specimen near Quipango. 45 km west of town	<1KM	Silva et al. ,1973

Appendix B – Geochemistry of KAC samples

Whole rock and trace element chemistry are presented below for additional reference of data from the KAC.

Sample	**Latitude**	**Longitude**	SiO2 (wt%)	Al2O3 (wt%)	Fe2O3 (wt%)	FeO (wt%)	MnO (wt%)	MgO (wt%)	CaO (wt%)	Na2O (wt%)	K2O (wt%)	TiO2 (wt%)	P2O5 (wt%)	Cr2O3 (wt%)	NiO (wt%)	LOI (wt%)	TOTAL (wt%)
KAC 12/14	-16.991294	13.914362	45.84	16.24	1.60	12.97	0.19	11.48	7.46	2.69	0.42	1.00	0.10	0.05	0.03	0.24	100.32
KAC 13/18	-16.985413	13.913089	47.65	20.48	1.03	8.36	0.13	9.04	9.07	2.93	0.40	0.51	0.13	0.02	0.04	0.25	100.03
KAC 17/22	-16.931429	13.634316	49.40	27.37	0.28	2.32	0.04	3.38	12.94	2.98	0.20	0.20	0.04	0.02	0.01	1.02	100.20
KAC 19/24	-16.885108	13.540396	47.64	28.72	0.35	2.85	0.05	2.78	13.93	2.39	0.17	0.16	0.03	0.01	0.01	0.96	100.06
KAC 41/42A	-16.573563	13.552322	52.20	19.61	0.95	7.69	0.17	4.90	8.73	3.87	0.36	0.85	0.34	0.03	0.01	0.23	99.94
KAC 47/47	-16.586	13.803968	50.61	25.94	0.39	3.17	0.05	4.31	10.81	3.65	0.29	0.11	0.03	0.01	0.02	0.53	99.92
KAC 57/55	-16.611722	13.887869	49.36	16.33	1.35	10.95	0.19	5.46	8.95	3.34	0.53	3.01	0.15	0.02	0.01	0.19	99.83
KAC 65/62	-16.330336	13.910539	52.77	26.71	0.37	2.94	0.02	0.92	9.37	4.88	0.61	0.75	0.02	0.04	0.01	0.34	99.73
KAC 83/76	-15.764355	14.082721	54.10	27.54	0.08	0.68	0.01	0.21	10.43	5.13	0.50	0.13	0.04	0.01	0.00	0.60	99.47
KAC 87/79	-15.547076	14.052496	52.95	26.36	0.31	2.51	0.04	1.53	9.94	4.75	0.58	0.28	0.10	0.01	0.00	0.30	99.67
KAC 90/83	-15.364488	13.946578	47.85	23.48	0.83	6.77	0.10	6.84	10.78	2.78	0.22	0.40	0.05	0.02	0.02	0.20	100.33
KAC 99/93	-14.942444	14.044063	46.41	23.86	0.71	5.76	0.10	8.26	11.71	2.10	0.14	0.22	0.03	0.02	0.04	0.80	100.14
KAC 103/96	-14.926523	14.102807	47.90	26.75	0.46	3.69	0.06	5.28	13.45	2.20	0.11	0.16	0.03	0.02	0.02	0.31	100.42
KAC 108/99	-14.878949	14.182671	48.15	27.69	0.40	3.24	0.05	3.67	13.43	2.44	0.13	0.23	0.03	0.02	0.01	1.04	100.53
KAC 109/100	-14.923292	14.196161	46.98	28.19	0.38	3.08	0.06	4.33	13.85	2.06	0.09	0.18	0.03	0.01	0.02	0.94	100.19
KAC 113/103	-14.86366	14.295512	48.83	26.72	0.45	3.59	0.06	3.61	12.25	2.87	0.17	0.38	0.04	0.01	0.01	0.59	99.57
KAC 114/104	-14.859644	14.316895	48.58	28.36	0.38	3.04	0.05	2.90	13.64	2.43	0.17	0.18	0.03	0.01	0.01	0.42	100.19
KAC 115/105	-14.850091	14.370413	47.01	25.99	0.64	5.23	0.09	5.98	12.38	2.13	0.12	0.18	0.03	0.01	0.02	0.54	100.36
KAC 123/112	-15.111019	14.069486	49.08	26.10	0.52	4.16	0.06	4.55	11.79	3.06	0.19	0.17	0.03	0.01	0.01	0.18	99.92

KAC 126/114	-15.134554	14.084448	48.68	25.77	0.56	4.49	0.07	5.02	11.61	2.83	0.22	0.10	0.02	0.00	0.02	0.21	99.60
KAC 135/124	-15.113305	14.2057	48.06	28.89	0.31	2.48	0.05	3.04	14.01	2.24	0.11	0.15	0.03	0.01	0.01	0.60	99.98
KAC 142 /131	-15.791525	13.84534	47.00	21.95	1.04	8.47	0.12	8.46	9.86	2.65	0.22	0.44	0.04	0.01	0.03	-0.07	100.22
KAC 144 /139	-15.847505	13.814323	50.89	24.19	0.58	4.64	0.06	5.16	9.67	3.91	0.33	0.22	0.04	0.01	0.02	0.20	99.90
KAC 152 /146A	-15.415549	13.816918	52.24	25.96	0.41	3.28	0.05	1.36	11.20	4.15	0.42	0.62	0.04	0.01	0.00	0.32	100.06
KAC 166/153	-15.438558	13.779098	45.77	22.43	0.92	7.48	0.10	10.26	10.45	2.05	0.12	0.08	0.03	0.01	0.05	0.40	100.16
KAC 168/155	-15.191133	13.936662	47.68	21.70	0.94	7.63	0.14	5.32	11.89	2.57	0.33	1.01	0.14	0.02	0.01	0.86	100.22
KAC 170/159	-15.178472	13.987676	48.70	28.09	0.36	2.89	0.05	3.39	13.25	2.65	0.16	0.13	0.03	0.01	0.01	0.17	99.88
KAC 172/160	-15.693594	14.091193	53.52	27.77	0.13	1.04	0.01	0.63	11.00	4.68	0.41	0.13	0.03	0.00	0.00	0.32	99.67

Sample	**Lat (S)**	**Long (E)**	Li (ppm)	P (ppm)	Sc (ppm)	Ti (ppm)	V (ppm)	Cr (ppm)	Co (ppm)	Ni (ppm)	Cu (ppm)	Zn (ppm)	Ga (ppm)	As (ppm)	Rb (ppm)
KAC 12/14	-16.991294	13.914362	3.62	270.55	8.86	3248.65	160.47	138.03	54.79	118.81	21.25	60.36	10.15	0.31	4.19
KAC 13/18	-16.985413	13.913089	3.62	603.55	4.88	3160.25	60.16	26.85	65.14	307.53	22.45	68.71	15.06	0.53	5.94
KAC 17/22	-16.931429	13.634316	0.76	171.18	1.98	1214.10	36.09	30.01	15.66	109.25	22.16	14.81	12.94	0.52	1.12
KAC 19/24	-16.885108	13.540396	1.44	89.50	1.24	875.42	21.27	9.38	17.53	70.91	12.05	17.33	13.85	0.52	1.16
KAC 41/42A	-16.573563	13.552322	7.01	1524.82	13.23	5048.86	179.10	120.20	29.16	54.82	18.95	94.28	21.91	0.53	1.43
KAC 47/47	-16.586	13.803968	1.09	107.46	0.54	603.58	5.12	9.46	25.83	137.90	4.52	21.08	13.28	0.50	0.41
KAC 57/55	-16.611722	13.887869	4.60	614.48	23.00	17058.54	331.11	26.01	46.17	88.95	77.86	102.71	18.14	0.52	1.93
KAC 65/62	-16.330336	13.910539	1.48	42.58	0.11	4839.18	113.69	167.16	15.60	53.64	5.28	24.36	18.20	0.54	0.31
KAC 83/76	-15.764355	14.082721	1.67	161.14	0.57	943.81	6.38	4.86	3.40	9.40	5.77	17.83	11.22	0.39	1.23
KAC 87/79	-15.547076	14.052496	2.80	416.05	0.76	1693.35	24.45	29.01	17.82	22.86	7.93	20.71	19.52	0.53	1.97
KAC 90/83	-15.364488	13.946578	2.19	170.15	2.78	2004.29	51.14	23.90	47.59	132.02	19.79	39.69	14.87	0.42	1.82

KAC 99/93	-14.942444	14.044063	2.78	93.79	4.76	1350.60	40.28	49.47	52.41	298.96	22.52	42.84	14.38	0.55	1.03
KAC 103/96	-14.926523	14.102807	1.30	82.90	3.45	941.58	37.47	61.99	36.92	144.80	14.88	24.38	14.31	0.54	0.73
KAC 108/99	-14.878949	14.182671	1.46	120.56	2.90	1424.90	35.87	14.74	27.62	70.13	11.00	15.23	11.31	0.44	0.76
KAC 109/100	-14.923292	14.196161	1.13	69.57	1.15	879.87	24.38	24.35	23.33	105.71	37.93	20.39	12.62	0.39	0.52
KAC 113/103	-14.86366	14.295512	1.78	137.65	2.03	2385.49	44.05	13.37	22.79	71.66	17.32	22.66	15.65	0.54	1.30
KAC 114/104	-14.859644	14.316895	1.78	110.45	1.48	1132.44	24.18	11.43	18.63	66.50	13.14	19.61	15.24	0.53	0.83
KAC 115/105	-14.850091	14.370413	2.30	124.20	2.08	1090.67	22.56	27.52	38.95	132.36	23.11	37.49	13.98	0.54	0.96
KAC 123/112	-15.111019	14.069486	1.77	93.01	1.75	984.05	21.13	17.34	32.44	118.57	10.21	25.37	16.70	0.53	0.75
KAC 126/114	-15.134554	14.084448	1.88	57.52	1.08	496.25	8.64	7.91	28.45	88.99	9.53	20.87	11.90	0.30	0.85
KAC 135/124	-15.113305	14.2057	1.18	91.13	1.73	792.49	26.90	19.33	20.80	56.41	13.53	15.79	14.37	0.37	0.74
KAC 142 /131	-15.791525	13.84534	3.26	144.30	3.28	2436.90	67.39	26.17	66.70	176.84	12.62	54.98	15.18	0.35	1.70
KAC 144 /139	-15.847505	13.814323	3.80	125.15	1.09	1158.84	16.68	37.48	35.98	102.61	9.90	28.62	14.89	0.31	1.27
KAC 152 /146A	-15.415549	13.816918	2.61	158.26	4.71	3402.54	134.57	10.94	13.87	13.51	29.99	24.58	21.50	0.33	0.93
KAC 166/153	-15.438558	13.779098	1.93	89.34	1.62	431.55	8.28	20.02	70.82	257.87	7.50	40.23	12.60	0.35	0.47
KAC 168/155	-15.191133	13.936662	7.16	557.86	14.82	5774.83	173.13	87.68	39.73	75.97	60.43	59.73	17.70	0.36	3.92
KAC 170/159	-15.178472	13.987676	1.37	74.11	1.19	929.56	13.33	14.52	18.50	160.98	17.31	18.02	12.39	0.35	0.70
KAC 172/160	-15.693594	14.091193	2.83	74.94	0.43	680.77	7.50	3.54	4.35	14.59	9.71	9.05	17.39	0.32	0.89

Sample	**Lat (S)**	**Long (E)**	Sr (ppm)	Y (ppm)	Zr (ppm)	Nb (ppm)	Ba (ppm)	Sn (ppm)	Cs (ppm)	La (ppm)	Ce (ppm)	Pr (ppm)	Nd (ppm)	Sm (ppm)	Eu (ppm)
KAC 12/14	-16.991294	13.914362	399.46	7.11	24.82	1.46	180.76	0.69	0.07	6.22	8.80	1.57	7.09	1.63	0.90
KAC 13/18	-16.985413	13.913089	462.12	7.11	33.21	2.50	186.76	0.53	0.11	5.32	13.96	1.55	6.57	1.43	0.68
KAC 17/22	-16.931429	13.634316	218.73	1.34	15.64	0.66	44.01	0.18	0.12	0.87	2.51	0.20	0.94	0.24	0.16
KAC 19/24	-16.885108	13.540396	226.38	0.74	6.54	0.42	33.44	0.30	0.02	0.75	2.46	0.18	0.75	0.16	0.16
KAC 41/42A	-16.573563	13.552322	728.62	8.64	33.06	3.29	420.01	1.14	0.05	16.11	40.74	3.83	15.52	3.00	1.15

KAC 47/47	-16.586	13.803968	321.39	0.28	1.53	0.10	76.68	0.51	0.02	0.85	2.13	0.18	0.70	0.14	0.24
KAC 57/55	-16.611722	13.887869	436.95	13.86	85.91	8.53	489.50	0.78	0.05	7.35	19.37	2.29	12.46	2.63	1.30
KAC 65/62	-16.330336	13.910539	423.18	0.01	0.19	0.02	235.36	0.10	0.00	0.75	0.80	0.07	0.21	0.10	0.51
KAC 83/76	-15.764355	14.082721	539.90	0.94	4.60	0.63	174.96	0.24	0.00	2.66	4.15	0.53	2.00	0.39	0.56
KAC 87/79	-15.547076	14.052496	646.58	1.56	3.76	0.62	312.90	0.41	0.00	4.22	7.97	0.96	3.59	0.71	1.08
KAC 90/83	-15.364488	13.946578	331.31	2.16	21.41	1.13	81.43	0.69	0.03	1.45	4.54	0.40	1.89	0.51	0.34
KAC 99/93	-14.942444	14.044063	318.56	2.04	8.37	0.51	54.06	0.27	0.01	1.91	4.24	0.34	1.43	0.35	0.28
KAC 103/96	-14.926523	14.102807	203.17	1.66	8.84	0.37	30.91	0.79	0.00	0.75	2.17	0.21	0.95	0.25	0.20
KAC 108/99	-14.878949	14.182671	242.12	1.80	12.55	0.94	34.57	0.49	0.00	1.14	2.22	0.28	1.24	0.29	0.21
KAC 109/100	-14.923292	14.196161	167.97	0.83	5.75	0.48	26.22	1.36	0.00	0.62	1.63	0.16	0.71	0.19	0.16
KAC 113/103	-14.86366	14.295512	206.68	1.46	15.62	1.59	36.53	0.26	0.00	0.79	2.79	0.21	0.96	0.23	0.15
KAC 114/104	-14.859644	14.316895	237.07	0.95	10.47	0.60	52.92	0.37	0.00	0.86	2.47	0.21	0.87	0.19	0.18
KAC 115/105	-14.850091	14.370413	263.43	1.32	7.61	0.69	35.76	0.45	0.01	1.02	3.04	0.24	1.01	0.24	0.20
KAC 123/112	-15.111019	14.069486	237.81	0.85	7.35	0.40	49.02	0.45	0.00	0.68	2.46	0.16	0.72	0.17	0.23
KAC 126/114	-15.134554	14.084448	235.17	0.35	2.16	0.16	55.32	0.18	0.00	0.81	1.43	0.16	0.67	0.16	0.30
KAC 135/124	-15.113305	14.2057	228.17	0.81	6.02	0.37	36.96	0.40	0.00	0.97	2.06	0.20	0.93	0.21	0.22
KAC 142 /131	-15.791525	13.84534	362.03	1.94	14.55	0.89	99.68	0.48	0.02	1.99	4.32	0.48	2.23	0.53	0.48
KAC 144 /139	-15.847505	13.814323	396.77	0.59	4.39	0.43	116.89	0.28	0.01	1.37	2.74	0.27	1.11	0.28	0.41
KAC 152 /146A	-15.415549	13.816918	319.22	1.70	12.25	0.76	129.28	0.42	0.01	1.77	3.36	0.44	2.11	0.55	0.56
KAC 166/153	-15.438558	13.779098	377.01	0.37	2.35	0.14	81.38	0.23	0.00	1.17	1.91	0.19	0.78	0.19	0.42
KAC 168/155	-15.191133	13.936662	342.48	10.62	42.34	3.72	164.79	1.01	0.15	7.08	14.80	1.92	8.87	2.20	0.89
KAC 170/159	-15.178472	13.987676	248.02	0.57	4.33	0.43	43.98	1.08	0.00	0.73	1.40	0.15	0.71	0.18	0.26
KAC 172/160	-15.693594	14.091193	397.25	0.32	2.43	0.17	122.66	0.85	0.00	1.05	1.78	0.19	0.82	0.23	0.34

Sample	**Lat (S)**	**Long (E)**	Gd (ppm)	Tb (ppm)	Dy (ppm)	Ho (ppm)	Er (ppm)	Tm (ppm)	Yb (ppm)	Lu (ppm)	Hf (ppm)	Ta (ppm)	W (ppm)	Pb (ppm)	Th (ppm)	U (ppm)
KAC 12/14	-16.991294	13.914362	1.54	0.23	1.38	0.29	0.78	0.11	0.78	0.12	0.66	0.08	0.06	2.14	0.55	0.11
KAC 13/18	-16.985413	13.913089	1.42	0.21	1.21	0.24	0.66	0.10	0.61	0.09	0.82	0.15	0.06	1.78	0.57	0.16
KAC 17/22	-16.931429	13.634316	0.26	0.04	0.23	0.05	0.13	0.02	0.13	0.02	0.37	0.03	0.01	0.77	0.04	0.02
KAC 19/24	-16.885108	13.540396	0.17	0.02	0.13	0.03	0.06	0.01	0.06	0.01	0.16	0.02	0.02	0.73	0.03	0.03
KAC 41/42A	-16.573563	13.552322	2.72	0.33	1.67	0.31	0.84	0.11	0.69	0.11	0.94	0.08	0.03	3.55	0.16	0.04
KAC 47/47	-16.586	13.803968	0.11	0.01	0.06	0.01	0.03	0.00	0.02	0.00	0.03	0.01	0.04	0.74	0.00	0.00
KAC 57/55	-16.611722	13.887869	2.63	0.40	2.41	0.49	1.36	0.21	1.31	0.20	2.07	0.42	0.05	2.52	0.10	0.03
KAC 65/62	-16.330336	13.910539	0.02	0.00	0.00	0.00	0.00	0.00	0.00	0.00	0.00	0.00	0.01	0.83	0.00	0.00
KAC 83/76	-15.764355	14.082721	0.30	0.04	0.17	0.03	0.09	0.01	0.07	0.01	0.11	0.03	0.04	0.73	0.05	0.01
KAC 87/79	-15.547076	14.052496	0.55	0.07	0.31	0.06	0.14	0.02	0.12	0.02	0.09	0.03	0.02	1.46	0.10	0.02
KAC 90/83	-15.364488	13.946578	0.50	0.07	0.41	0.09	0.23	0.03	0.21	0.03	0.55	0.06	0.03	0.64	0.18	0.06
KAC 99/93	-14.942444	14.044063	0.39	0.06	0.34	0.07	0.19	0.03	0.18	0.03	0.22	0.04	0.03	0.76	0.06	0.02
KAC 103/96	-14.926523	14.102807	0.27	0.05	0.27	0.06	0.16	0.02	0.15	0.02	0.23	0.02	0.02	0.65	0.04	0.02
KAC 108/99	-14.878949	14.182671	0.31	0.05	0.31	0.06	0.16	0.03	0.15	0.03	0.29	0.05	0.03	0.45	0.10	0.02
KAC 109/100	-14.923292	14.196161	0.19	0.03	0.17	0.04	0.10	0.01	0.09	0.01	0.17	0.02	0.01	0.76	0.03	0.02
KAC 113/103	-14.86366	14.295512	0.27	0.04	0.24	0.05	0.14	0.02	0.14	0.02	0.40	0.08	0.02	0.70	0.06	0.03
KAC 114/104	-14.859644	14.316895	0.19	0.03	0.16	0.03	0.09	0.01	0.08	0.01	0.26	0.03	0.02	1.02	0.05	0.02
KAC 115/105	-14.850091	14.370413	0.26	0.04	0.21	0.04	0.13	0.02	0.12	0.02	0.21	0.04	0.01	0.90	0.06	0.02
KAC 123/112	-15.111019	14.069486	0.19	0.03	0.16	0.03	0.08	0.01	0.07	0.01	0.20	0.02	0.01	0.60	0.03	0.02
KAC 126/114	-15.134554	14.084448	0.12	0.01	0.07	0.01	0.04	0.01	0.04	0.01	0.06	0.01	0.02	0.43	0.02	0.01
KAC 135/124	-15.113305	14.2057	0.21	0.03	0.16	0.03	0.09	0.01	0.08	0.01	0.16	0.02	0.01	0.44	0.04	0.01
KAC 142 /131	-15.791525	13.84534	0.49	0.07	0.37	0.08	0.21	0.03	0.19	0.03	0.35	0.05	0.02	0.62	0.10	0.03

KAC 144 /139	-15.847505	13.814323	0.22	0.02	0.12	0.02	0.07	0.01	0.05	0.01	0.11	0.02	0.01	0.65	0.03	0.01
KAC 152 /146A	-15.415549	13.816918	0.47	0.06	0.39	0.07	0.21	0.03	0.18	0.03	0.34	0.04	0.01	0.90	0.07	0.02
KAC 166/153	-15.438558	13.779098	0.14	0.01	0.07	0.01	0.04	0.00	0.03	0.01	0.06	0.01	0.01	0.39	0.02	0.01
KAC 168/155	-15.191133	13.936662	2.33	0.33	2.05	0.42	1.15	0.17	1.03	0.16	1.34	0.18	0.02	1.65	0.27	0.08
KAC 170/159	-15.178472	13.987676	0.15	0.02	0.11	0.02	0.06	0.01	0.05	0.01	0.12	0.02	0.01	0.50	0.02	0.01
KAC 172/160	-15.693594	14.091193	0.14	0.02	0.08	0.01	0.04	0.00	0.03	0.00	0.06	0.01	0.00	0.93	0.02	0.01